# NONINVASIVE BLOOD FLOW AND OXYGENATION MEASUREMENTS IN DISEASED TISSUE

A Dissertation submitted in partial fulfilment of the
requirements for the degree of
Doctor of Philosophy

by

BENJAMIN S. RINEHART

B.S.B.E., Wright State University, 2014

M.S.B.M.E, Wright State University, 2016

2021

Wright State University

WRIGHT STATE UNIVERSITY

GRADUATE SCHOOL

September 16, 2021

I HEREBY RECOMMEND THAT THE DISSERTATION PREPARED UNDER MY SUPERVISION BY BENJAMIN S. RINEHART ENTITLED NONINVASIVE BLOOD FLOW AND OXYGENATION MEASUREMENTS OF DISEASED TISSUE BE ACCEPTED IN PARTIAL FULFILLMENT OF THE REQUIREMENTS FOR THE DEGREE OF DOCTOR OF PHILOSOPHY.

Ulas Sunar, PhD
Dissertation Director

Ahsan Mian
Program Director, PhD in Engineering

Barry Milligan, Ph.D.
Vice Provost for Academic Affairs
Dean of the Graduate School

Committee on Final Examination:

Andrew Voss, Ph.D.

Mark Rich, Ph.D.

Tarun Goswami, PhD

Sandra Kostyk, MD, PhD

# ABSTRACT

Rinehart, Benjamin S. Ph.D., Engineering Ph.D. Program, Wright State University, 2021.
Noninvasive Blood Flow and Oxygenation Measurements in Diseased Tissue.

The research presented in this dissertation focused on the application of optical imaging techniques to establish blood flow and oxygen saturation as effective biomarkers for two disease cases, Autism Spectrum Disorder (ASD) and Huntington's Disease (HD). The BTBR mouse model of ASD was utilized to validate measurements of cerebral blood flow and oxygenation as biomarkers for autism. The R6/2 mouse model of juvenile HD was utilized to validate measurements of skeletal muscle blood flow following tetanic muscle contractions induced by electrical nerve stimulation. Next, a noncontact, camera-based system to measure blood flow and oxygen saturation maps was implemented to improve upon the previous HD mouse results by providing spatial heterogeneity in a wild-type mouse model. Finally, translational research was performed to validate a research design conducting concurrent grip strength force and skeletal muscle blood flow and oxygenation measurements in a healthy human population that will be used to establish HD biomarkers in humans in future clinical applications.

# Contents

# LIST OF FIGURES

# ACKNOWLEDGEMENT

I would like to formally acknowledge my advisor, Dr. Ulas Sunar, for the support I have received throughout my dissertation process. I have been fortunate to work with an advisor who provided motivation, incredible knowledge and a model work ethic to learn from. My advisory committee, Dr. Voss, Dr. Rich, Dr. Goswami and Dr. Kostyk for their support and encouragement. Chien-Sing Poon and Dharminder Langri who worked beside and supported me every day in the BMIL lab at Wright State and Steve Burke for his support during my murine model experiments.

*Dedicated to the loving memory of my father, Lloyd Arthur Rinehart. Thank you for everything Dad. I could not have done this without you.*

# 1. Introduction

The symptoms and detrimental effects of a variety of diseases can be traced back to inefficiencies in hemodynamic parameters including blood flow and tissue oxygenation. In this thesis, optical imaging is applied for cases of two diseases, autism spectrum disorder (ASD) and Huntington's disease (HD). Thus, the experiments and research detailed herein will focus on the application of optical imaging techniques to establish blood flow and oxygen saturation as effective biomarkers for these diseases.

## 1.1. Autism Spectrum Disorder

Autism spectrum disorders (ASD) is now recognized to occur in approximately 1% of the population and is a major public health concern because of their early onset, lifelong persistence, and high levels of associated impairment(Simonoff et al., 2008) . ASD is a highly heritable, biologically-based neurodevelopmental disorder. Despite this fact, the exact cause remains unknown. Finding the cause has been challenging because ASD encompasses a range of complex disorders that involve multiple genes and demonstrate great phenotypical variation. Estimates of recurrence risks based on family studies of idiopathic ASD are approximately 6% when there is an older sibling diagnosed with ASD, and even higher when there are already two children with ASD in the family(Johnson & Myers, 2007) . One of the main difficulties in diagnosing and treating autism is the observational nature of diagnostic schedules(Lord et al., 2000) . Although these diagnostic methods have a high sensitivity of around 90%, the specificity can be quite low, leading to overdiagnosis and overtreatment. Also, the time requirement is cost-intensive and requires a dedicated team of physicians to accurately track progress.

There exists a need for a non-observational diagnostic system capable of measuring in vivo biomarkers to both accurately place a patient along the ASD spectrum and track the efficacy of therapies in patients that receive them. Recent *in vivo* imaging studies have shown that cerebral hypoperfusion presents as a comorbidity in subjects with subjects to ASD when compared to control groups. Traditionally, these measurements have been performed using positron emission tomography (PET) or single-photon emission computed tomography (SPECT) (Boddaert & Zilbovicius, 2002; Galuska et al., 2002; Sasaki et al., 2010; Zilbovicius et al., 1995, 2000) . Functional magnetic resonance imaging (fMRI) was also used in a series of ASD neuroimaging studies with a sensitivity of ASD diagnosis up to 75%(Dichter, 2012; Jann et al., 2015; Philip et al., 2012) . A time resolved arterial spin labelling MRI study has also shown robust hypoperfusion results in the ASD population over time(Yerys et al., 2018). The results of these studies are encouraging; however, the imaging modalities of PET, SPECT, and fMRI are limited for routine clinical use in the diagnosis of ASD in adolescents. The extended imaging durations and the sensitivity to motion artifacts also present a risk in rendering data unusable.

Efforts have been made in the optical imaging field to fill this need as optical imaging techniques possess the unique combination of advantages of being relatively inexpensive, simple to operate, and with non-contact imaging options. Initially, functional near-infrared spectroscopy (fNIRS) has been used to monitor hemodynamic abnormalities in autism subjects by monitoring changes in blood chromophore concentrations (specifically oxygenated and deoxygenated hemoglobin) as previously shown in clinical studies(J. Li et al., 2016) . Techniques less technically involved, such as dual-wavelength laser speckle imaging (DW-LSI), have also been used in animal studies(Abookasis et al., 2018) . DW-LSI has the advantage of measuring hemodynamics and blood flow simultaneously in a non-contact, camera-based setup. However, as DW-LSI is a wide-field illumination method, the penetration depth is limited to a few millimeters, in which the majority of the reflected signal will be from the scalp tissue, thereby convoluting the cerebral hemodynamics with blood flow information from the scalp.

Therefore, there exists a need for a low-cost, noninvasive optical imaging system capable of measuring brain blood flow and hemodynamics in the ASD mouse model.

## 1.2. Huntington’s Disease

Huntington’s Disease (HD) is a progressive neurodegenerative disease caused by a mutation of the huntingtin (HTT) gene. Specifically, there are more than 36 CAG trinucleotide repeats in the 5’ coding region of the IT15 gene located at locus 4p16.3, whereas a healthy individual would have 20-35 CAG units(Costa et al., 2006) . HD has a prevalence ranging from 4 to 8 people per 100,000, depending on geographic location(Folstein et al., 1987; Harper, 1992; Kokmen et al., 1994; Quarrell et al., 1988; Reed & Chandler, 1958; Shokeir, 1975; Simpson & Johnston, 1989) . Currently, there is no cure for HD; there exist only treatments to minimize symptoms(Cusin et al., 2013) .

Early symptoms of HD are neurocognitive (irritability, depression, difficulty synthesizing new information or memories) and neuromotor (chorea, poor coordination) in nature. As the disease inevitably progresses, these symptoms will advance to more pronounced bouts of chorea, as well as difficulty walking, speaking, and swallowing. This form of Huntington's disease, commonly referred to as the adult-onset form, carries a life expectancy of 15-20 years from the first onset of symptoms**.**

There exists a less common form of HD that begins in childhood or adolescence, known as the juvenile form. Aside from earlier onset, this form also presents with additional symptoms of clumsiness, slurred speech, drooling, and impaired thinking and reasoning abilities. Most drastically, the juvenile form also presents seizures in 30 to 50% of children. Due to the advanced morbidity and faster progression of the symptoms associated with the juvenile form of HD, affected children usually live only 10 to 15 years after signs and symptoms first appear. It should be noted that with the progression of the disease, patient mobility becomes greatly affected, increasing the risk of falls and directly affecting the functionality of patients who end up needing constant help in their daily living activities(Bilney et al., 2005; Carroll et al., 2015; Cruickshank et al., 2014; Koller & Trimble, 1985; Thaut et al., 1999; Wheelock et al., 2003) .

Traditionally, HD has been studied in the central nervous system (CNS), mainly in the basal ganglia and cerebral cortex. However, experiments performed in animal models have shown that mutant HTT is found outside of the CNS and in peripheral structures such as the skeletal muscles(van der Burg et al., 2009; Zielonka et al., 2014). This discovery led to further research that found that skeletal muscles of the R6/2 HD mouse models are hyperexcitable due to decreased chloride and potassium conductance(Miranda et al., 2017). Skeletal muscles exhibited pronounced hyperexcitability, the likely cause of which was decreased synaptic transmission across the neuromuscular junction (NMJ) (Khedraki et al., 2017; Waters et al., 2013) . This work suggests that there exists an HD pathology within the skeletal muscles that could be a candidate for targeted therapies to lessen the motor symptoms of late-stage HD.

There is increasing evidence of a primary skeletal muscle pathology in HD. Although the pathophysiology of the has not yet been determined, the expanded *huntingtin polyglutamine* protein has been suggested to play multiple roles leading to muscle fiber atrophy(Zielonka et al., 2014). The mutant *huntingtin* protein is known to form intracellular aggregates that are associated with muscle fiber atrophy. Possible pathways in which the mutant protein could contribute to fiber damage include impairment of heat shock proteins to remove aggregates(Labbadia & Morimoto, 2013) , disruption of transcription(Miranda et al., 2017; Zielonka et al., 2014) , and mitochondrial dysfunction that interrupts fiber metabolic function(Ayala-Peña, 2013; Chaturvedi et al., n.d.; J.-N. Zhu et al., 2019; Zielonka et al., 2014) .

Currently, there is no effective treatment for preventing HD and, therefore, no screening is performed(Wyant et al., 2017). Patient management approaches focus on relieving the patients' depression, anxiety and other mood disorders that are common components of the disease(Brandt, 2018) as well as pharmacological treatment of chorea(Armstrong & Miyasaki, 2012; Reilmann, n.d.) although there is a lack of evidence-based treatment. Therefore, it is necessary to further investigate the pathology of the disease and look for more therapeutic targets. The proposed methods will be able to assess many of the physiological indicators of the mechanism thought to be disrupted in HD through monitoring blood flow speed and tissue oxygen saturation in a noncontact, in vivo manner during skeletal muscle contractions.

## 1.3. Skeletal Muscle Contraction

First, we should describe how the action potentials are generated in the skeletal muscle which begins at the neuromuscular junction (NMJ). This is the site where the terminal end of a motor neuron fiber meets the muscle fiber. More specifically, the axon (synaptic) terminal of the motor nerve junctions with the motor end plate of the sarcolemma. When a neuronal action potential reaches the axon terminal, this stimulates the release of the neurotransmitter acetylcholine (ACh). ACh will then diffuse across the synaptic cleft and bind to ACh receptors on the motor end plate. The ACh binding triggers channels to open within the receptor, allowing ions to pass into the muscle fiber. An influx of positively charged ions will cause the membrane potential of the muscle fiber to depolarize. The spread of this depolarization across the sarcolemma triggers the voltage-gated sodium channels to open. As a result, sodium ions cross the membrane, causing an action potential to fire along the entire membrane to initiate excitation-contraction coupling.

The process of excitation-contraction coupling is what links the electrical stimulus of the action potential with the mechanical interactions that produce a muscle contraction. As the action potential sweeps along the sarcolemma, it will travel down t-tubules to reach the interior of the muscle. The membrane of the t-tubules contains voltage sensitive proteins which are linked to proteins within the SR. When these proteins are activated by the action potential, the release of Ca2+ ions from the SR will be triggered. These Ca2+ will then bind to troponin within the sarcoplasm, releasing the troponin-tropomyosin complex and allowing the binding sites on actin strands to be exposed. Myosin will then bind to the exposed actin binding sites to form cross-bridges. The myosin heads then pull the thin filaments past the thick filaments toward the center of the sarcomere. The sliding motion of these filaments shortens the sarcomere itself, which we refer to as a contraction. This sliding is a cyclical process in which each myosin head can only pull a short distance before it needs to be 'reloaded', a process that requires ATP.

Although these processes occur very quickly, they still require a finite amount of time to complete. Therefore, it is possible for a muscle fiber to be stimulated by a subsequent motor nerve action potential before the filaments have fully relaxed from the contraction caused by the previous action potential. As a result, the sarcomere will undergo another contraction starting at above the resting state of force production. Figure 1-1, below shows an example of how the increase in action potential frequency can causes an

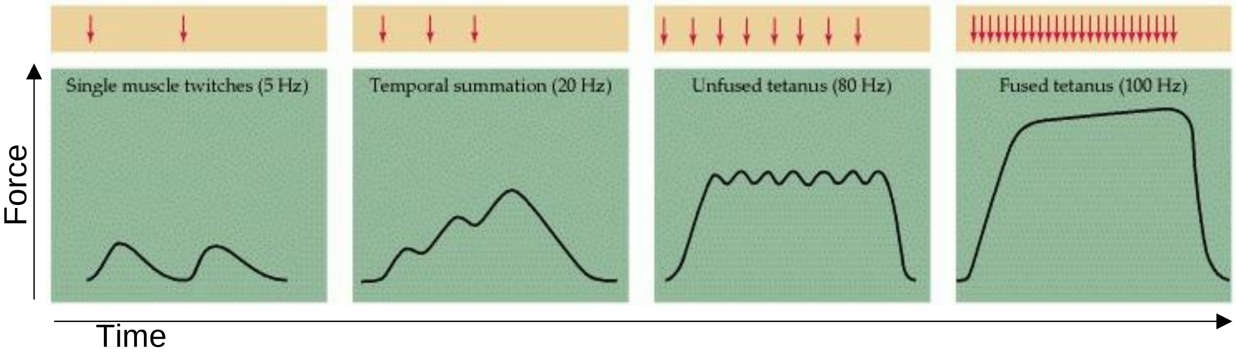

FIGURE 1-1 FORCE-FREQUENCY COUPLING EFFECT

increase in force production. With a low frequency of action potentials (5 Hz) the muscle fiber will have enough time to fully relax before the next contraction occurs. When the action potential frequency is increased to 10 Hz, the next contraction starts before the previous contraction is completed, and we start to see a summation effect in the force production. As the frequency increases to 80 Hz the force profile forms a “fused tetanus” which is when each contractile force spike is still individually discernible, but the force production stays sustainably elevated. At the higher end of the frequency spectrum, we see a fused tetanus at 100 Hz, where the motor nerve action potentials are happening so frequently that individual contractions are no longer discernible, and we see a steady increase in force production over time.

During periods of activation of the skeletal muscle, the metabolism of muscle fiber is greatly increased to aid in resupplying ATP to the system. Therefore, substrate and oxygen requirements are elevated above the resting state requirement, necessitating increased local blood flow to compensate. For this to occur, the body will undergo redistribution of blood flow, where renal and splanchnic blood flow will decrease by up to ~25% due to sympathetic vasoconstriction. This blood flow is redistributed to the active skeletal muscles by dilating the blood vessels that supply these regions. This dilation is stimulated by multiple mediators such as increased pCO2, K+, adenosine and nitric oxide whose production is stimulated by muscle activity.

The increase in pC02 is a by-product of increased glucose breakdown by the processes of aerobic and anaerobic glycolysis during muscle activity, leading to increased turnover of the citrate cycle, producing CO2. The increase in K+ is due to high action potential frequencies that do not allow adequate reuptake or washout of potassium. Adenosine is a by-product of ATP consumption during muscle fiber contraction. All three of these mediators formed during muscle activity can reach the smooth muscle of the adjacent arterioles and capillaries through diffusion, where they function as vasodilators.

As a result, monitoring blood flow speed and oxygen saturation within the skeletal muscle before, during, and after skeletal muscle contractions can be an indicator of muscular dysfunction. Blood oxygen saturation is a marker of mitochondrial dysfunction, which has previously been shown in HD(Carroll et al., 2015; Mueller et al., 2017).

# 2. Diffuse Optics Theory

There are established methodologies in the field of optical imaging that have the capability to perform the required measurements of blood flow velocity and blood oxygen saturation. This section will describe the underlying theory and equations surrounding diffuse optics with respect to the various methods of monitoring blood flow speed and oxygen saturation in living tissue.

## 2.1. Spatial Frequency Domain Imaging

Spatial frequency domain imaging (SFDI) is a wide-field optical imaging technique that quantifies the absorption ($\mu_a$) and scattering ($\mu_s'$) properties of a target tissue topographically. The absorption and scattering properties of the tissue govern how light propagates and diffuses through the tissue. Therefore, diffuse optical imaging techniques are dependent on the absorption and scattering properties of the tissue to resolve blood flow and oxygenation.

### 2.1.1 Theory - SFDI

Spatial frequency domain imaging (SFDI) is a wide-field optical imaging technique that quantifies the absorption ($\mu_a$) and scattering ($\mu_s'$) properties of a target tissue topographically. The signals of interest in SFDI are modeled as spatially modulated photon density waves in the spatial frequency domain. The diffusion of these photon density waves in homogeneous media are scattering dominated ($\mu_s' >> \mu_a$) such as human tissue can be described by a second-order photon diffusion equation:

$$\nabla^2\varphi - \mu_{eff}^2\varphi = -3\mu_{tr}q. \tag{1}$$

Where, $\varphi$ is the fluence rate related to measured power per unit area, $q$ is the source illumination, $\mu_{eff}$ is the effective attenuation, related to the product of absorption and scattering parameters, $\mu_{eff} = \sqrt{3\mu_s'\mu_a}$ , and $\mu_{tr} = (\mu_a + \mu_s')$ is the total attenuation of light contributed by both absorption and scattering. The light source is spatially modulated to project a light pattern that is normal to the place of incidence:

$$q = q_0(z)cos(k_x x + \alpha), \tag{2}$$

where $q_0$ is the power at depth $z$, the spatial frequency is $k_x = 2\pi f_x$ and $\alpha$ represents phase shift offset in radians. We can model the measured light intensity or fluence rate ($\varphi$) reflecting from the medium with the same frequency as the source, $q$:

$$\varphi = \varphi_0(z)cos(k_x x + \alpha). \tag{3}$$

Substituting Equations (2) and (3) into (1) yields a one-dimensional photon diffusion equation for the fluence rate as a function of depth $z$, which is the Helmholtz type differential equation:

$$\frac{d^2}{dz^2}\varphi_0(z) - \mu_{eff}'^2\varphi_0(z) = -3\mu_{tr}q_0(z), \tag{4}$$

This diffusion equation (Equation 4) implies that the solution for fluence rate can be modeled as an exponentially-damping signal with respect to depth z with a decay rate of $\mu_{eff}'$, which is defined as the effective attenuation,

$$\mu'_{eff} = \sqrt{\mu_{eff}^2 + k_x^2} \tag{5}$$

Equation 5 indicates that the decay rate depends on the usual effective attenuation ($\mu_{eff}^2$) for the continuous wave (CW) case when there is no modulation, with an additional term of spatial frequency modulation, $k_x^2$. Thus, the effective attenuation increases with spatial frequency, and higher frequencies are more attenuated (tissue acts as a low-pass filter). Thus, higher frequencies are more sensitive to superficial tissue, while lower frequencies probe deeper tissue. Since absorption length ($1/\mu_a \sim 100\ mm$) is much larger than and scattering length ($1/\mu'_s\ \sim 1mm$) higher frequencies are more sensitive to scattering (photons definitely scatter at the illuminated superficial region). From this, we can also infer that spatial modulation allows depth sectioning (or depth sensitivity), with the effective penetration depth can be defined as $\delta'_{eff} = 1/\mu'_{eff}$. Following the derivation from *"Quantitation and mapping of tissue optical properties using modulated imaging"*(Cuccia et al., 2009), the diffuse reflectance (the measured reflected light) can be obtained as:

$$R_d(k) = \frac{3Aa'}{(\mu'_{eff}/\mu_{tr} + 1)(\mu'_{eff}/\mu_{tr} + 3A)}, \tag{6}$$

where $a' = \mu'_s/\mu_{tr}$ is the reduced albedo and $A = (1 - R_{eff})/2(1 + R_{eff})$ is the proportionality constant. Here, $n$ is the refractive index of tissue and $R_{eff} \approx 0.0636n + 0.668 + (0.710/n) - (1.440/n^2)$ is the effective reflection coefficient. Thus, one can simulate photon diffuse reflectance with respect to different spatial frequencies for different cases of optical parameters by using this simple and fast analytical solution via

MATLAB. The optical properties, $\mu_a$ and $\mu_s'$, can be recovered by fitting this model to the experimental data. The optical absorption parameter depends on the concentration of chromophores in the tissue. At near-infrared wavelengths, the dominant absorbers are oxygenated hemoglobin (HbO) and deoxygenated hemoglobin (Hb). The total absorption can be represented as the sum of these two contributors,

$$\mu_a(\lambda) = \varepsilon_{HbO}(\lambda)C_{HbO} + \varepsilon_{Hb}(\lambda)C_{Hb}$$

Where, $\varepsilon_{HbO}, \varepsilon_{Hb}$ are the molar extinction coefficients for the chromophores at wavelength $\lambda$. The extinction coefficients are an inherent property of the chromophores themselves and are dependent on how strongly the chromophore absorbs light at a given concentration. The unknowns in the above equation $(C_{HbO}, C_{Hb})$ represent the concentrations of the chromophores and can be recovered by taking measurements at two optical wavelengths. From this, the tissue oxygen saturation (StO2 %) can be obtained:

$$StO2\,\% = \frac{C_{HbO}}{C_{HbT}} * 100$$

Where total hemoglobin concentration, $C_{HbT} = C_{HbO} + C_{Hb}$.

StO2 is an important physiological measure that can be used as an indicator of hypoxic conditions.

### 2.1.2 Application – SFDI

In practice, the spatially modulated photon density waves are projected as three separate, phase-shifted sinusoidal patterns. As shown in Figure 1-2, below.

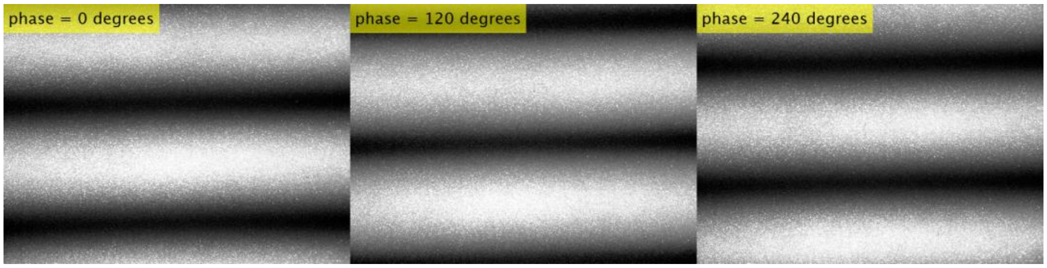

FIGURE 2-1 THREE-PHASE EXAMPLE OF SPATIALLY MODULATED LIGHT PROJECTION PATTERNS

The above three photon diffusion wave patterns encode the reflectance information for a single spatial frequency, which is obtained through demodulation:

$$M_{AC}(x_i, f_x) = \frac{\sqrt{2}}{3}\sqrt{[I_1(x_i) - I_2(x_i)]^2 + [I_2(x_i) - I_3(x_i)]^2 + [I_3(x_i) - I_1(x_i)]^2}, \tag{7}$$

Where $I_1$, $I_2$, $I_3$ represent the modulated SFDI patterns. Each demodulated spatial frequency corresponds to a point of the modulation transfer function (MTF) that is fit to find the optical properties. This three-phase approach is advantageous because it allows for removing common image noise and digitization offsets in each image (Cuccia et al., 2005) .

Experimental modulation amplitude, $M_{AC}(x_i, f_x)$ depends on the source intensity, the modulation transfer function (MTF) of the illumination and imaging optical system, and tissue MTF, $R_d$ , also called diffuse reflectance of the tissue depending on the spatial frequencies:

$$M_{AC}(x_i, f_x) = I_0 \, MTF_{system}(x_i, f_x) \, R_d(x_i, f_x) \qquad (8)$$

Since we are only interested in tissue response, $R_d$ , one can obtain it by normalizing the measurements to a reference standard, where the intensity and instrument response are assumed to be the same for both unknown and reference measurements. Thus, unknown diffuse reflectance, $R_d$, which contains the tissue response (and optical properties) can be written as:

$$R_d(x_i, f_x) = \frac{M_{AC}(x_i, f_x)}{M_{AC,ref}(x_i, f_x)} * R_{d,ref,pred}(f_x), \qquad (9)$$

where $R_d$ is the calibrated reflectance curve, $M_{AC}$ is the MTF of the tissue, $M_{AC,ref}$, and $R_{d,ref,pred}$ is the reflectance curve for the known reference phantom. This normalization allows eliminating absolute intensity and instrument response measurements(Cuccia et al., 2005). An example of $R_d$ curve measured from a human skin is shown in Figure 2-2, below:

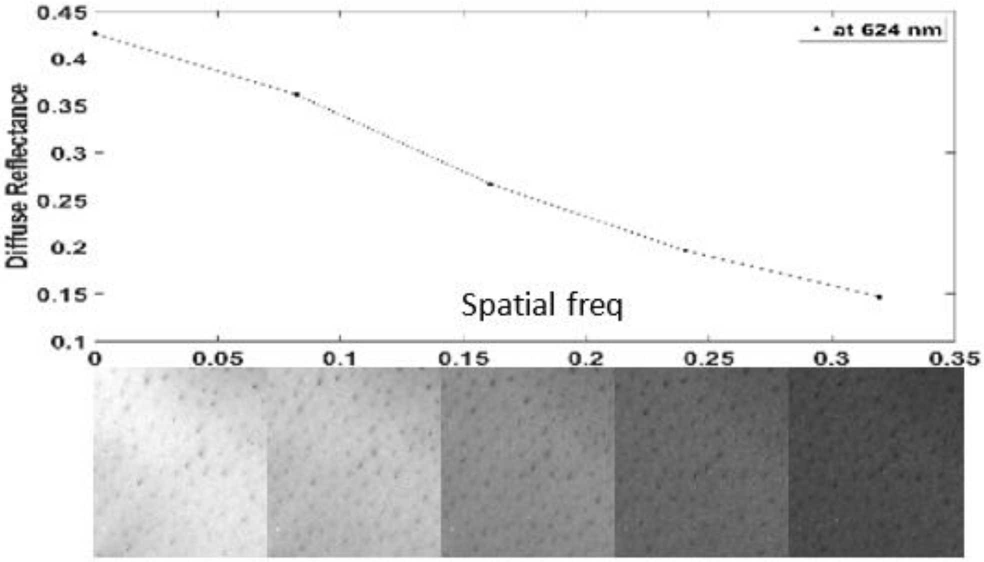

FIGURE 2-2 DIFFUSE REFLECTANCE RELATIONSHIP WITH SPATIAL FREQUENCY

By fitting the reflectance, $R_d$, curve for each pixel, the optical properties can be obtained, locally. As mentioned above, one of the main advantages of SFDI is the sensitivity to both scattering and absorption by projecting different spatial frequencies. This can be seen clearly in Figure 2-3, where $R_d$, curve is plotted with respect to spatial frequencies by changing the optical parameters at a single pixel. For example, Figure 2-3 (right) shows $R_d$ values do not change at high frequencies at different absorption coefficients. This indicates that $R_d$ is not sensitive to absorption parameter ($\mu_a$) but only scattering parameter ($\mu_s'$).

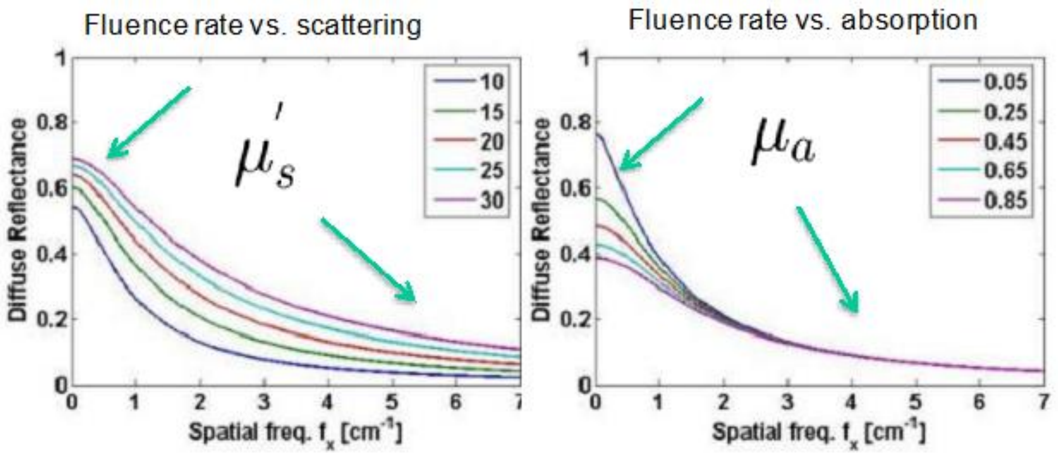

FIGURE 2-3 DIFFUSE REFLECTANCE DEPENDENCE ON OPTICAL PROPERTIES. SCATTERING (LEFT) AND ABSORPTION (RIGHT)

The figure on the left indicates that the scattering parameters are sensitive to both high and low spatial frequencies. As mentioned before, this spatial frequency-dependent sensitivity allows for accurate quantification of both $\mu_a$ and $\mu_s'$.

There is a trade-off between the accuracy of optical property quantification and data acquisition time. Typically, three spatial frequencies at $DC$, $low - frequency\, mm^{-1}$, and $high - frequency\, mm^{-1}$ components are used to obtain accurate quantification of both $\mu_a$ and $\mu_s'$. A least squares minimization method is used to fit $R_d$ for each pixel to obtain the optical property maps. A flow chart of optical property map quantification is shown Figure 2-4 below.

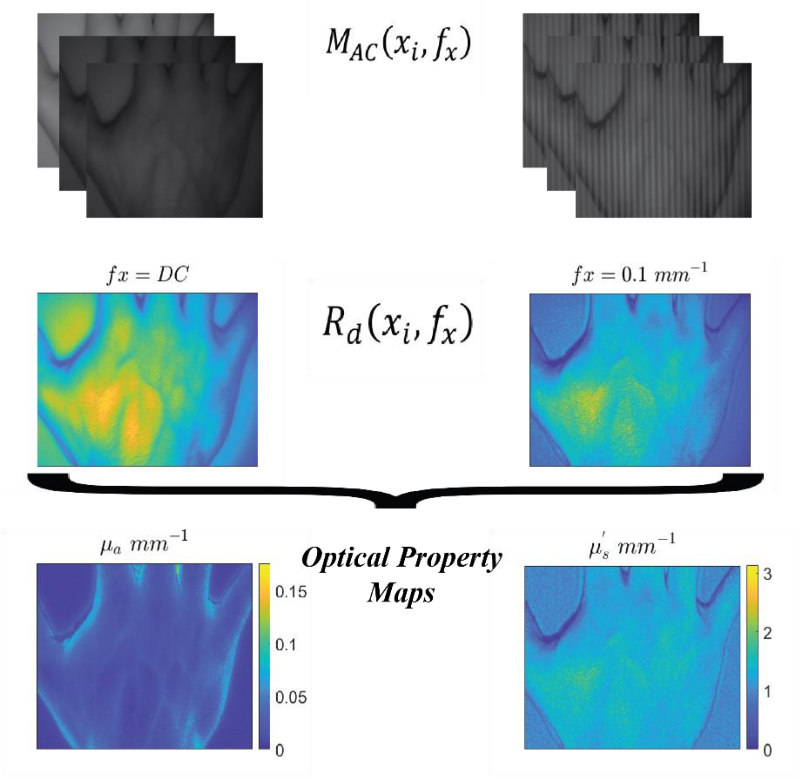

FIGURE 2-4 TWO-DIMENSIONAL OPTICAL PROPERTY FITTING PROGRESSION

One of the advantages of SFDI is that the instrumentation is relatively inexpensive compared to other functional imaging modalities, such as functional magnetic resonance imaging (fMRI) and single photon emission computed tomography (SPECT). A diagram of a traditional spatial frequency domain imaging instrument is shown below in Figure 2-5.

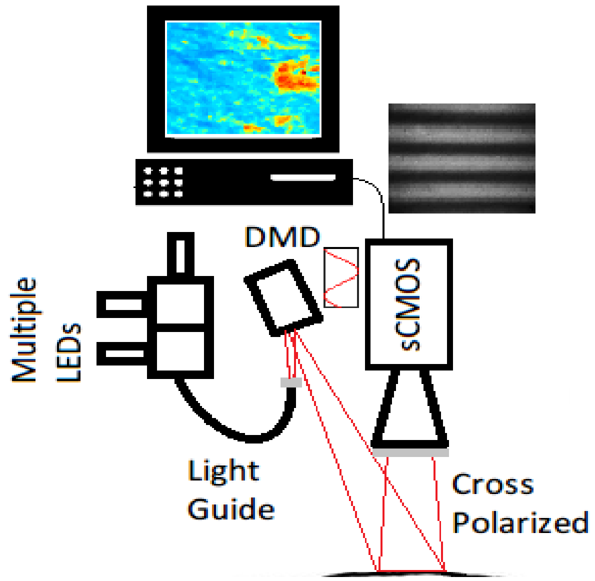

FIGURE 2-5 DIAGRAM OF THE SPATIAL FREQUENCY DOMAIN IMAGING SYSTEM FROM "QUANTITATION AND MAPPING OF TISSUE OPTICAL PROPERTIES USING MODULATED IMAGING" (CUCCIA ET AL., 2009)

Multiple LED light at different wavelengths coupled with a light guide focused onto a spatial light modulator (SLM), in our case a projector with an internal digital micromirror device (DMD), that produces the sinusoidal modulation patterns. Light from the DMD illuminates the target tissue and diffuse reflected light is measured by a scientific CMOS (sCMOS) camera. Cross-polarizers eliminates specular reflection so that only photons that diffuse in the tissue is measured.

## 2.2 Laser Speckle Contrast Imaging

Laser speckle contrast imaging (LSCI) is an optical imaging technique used for wide-field imaging of blood flow. The LSCI technique observes fluctuations in a dynamic laser speckle pattern to detect the movements of particles. The technique is similar to how both laser and ultrasound Doppler observe frequency shifts to measure particle speed(JD, 2001). LSCI is a powerful tool to measure in-vivo blood flow. However, due to the reliance on reflected speckle patterns, the penetration depth is limited to the range of millimeters(P et al., 2003). Therefore, LSCI is most useful in imaging shallow blood flow, such as perfusion in the skin or the retina. LSCI has also been used to image exposed tissue in animal models.

Laser speckle patterns are generated from the random interference of coherent light. A photodetector will receive light that has scattered from varying positions within the medium. As a result, the light photons have traveled over a distribution of distances, which results in constructive and destructive interference(Boas & Dunn, 2010) . These interference patterns manifest themselves as a randomly varying intensity pattern in space, which can reflect onto the photodetector surface, as shown in the example speckle image shown below in Figures 2-6.

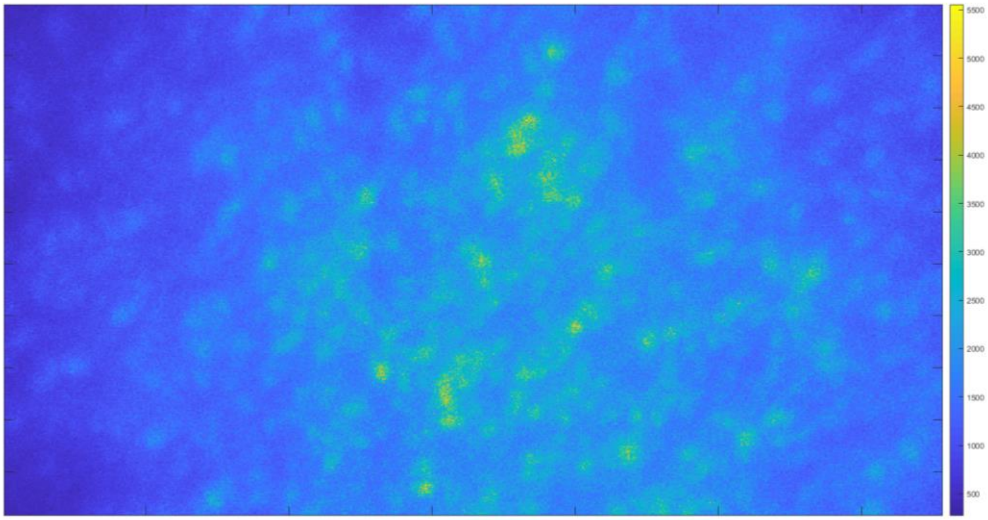

FIGURE 2-6 SPECKLE INTERFERENCE PATTERN EXAMPLE

Moving particles within the imaging field will cause spatial blurring in the speckle pattern. In areas of increased blood flow, the intensity fluctuations are more rapid and will cause increased blurring over the camera exposure time. Therefore, spatial maps of relative blood flow can be obtained by acquiring images of the speckle pattern and quantifying the blurring of the speckles in the image by measuring the spatial contrast of the intensity variations. The quantification of speckle blurring is defined as the ratio of the standard deviation of the mean intensity:

$$K_s = \frac{\sigma_s}{<I>} \tag{1}$$

Where, $\sigma_s$ is the spatial standard deviation of speckle intensity within a region of interest,$< I >$ is the mean intensity over that same region of interest and $K_s$ is the speckle contrast measurement as previously defined. $K_s$ values are between 0 and 1. $K_s$ values decrease as scatterer velocity increases until a value of $K_s = 0$ theoretically occurs when the scatterers are moving fast enough to blur all the pixels. On the contrary, the speckle contrast will approach 1 as the scatterer velocity decreases. However, the maximum speckle contrast will depend on the diffusion properties of the medium. The two-dimensional sliding window leads to the inverse square of the speckle contrast, $K_t$, being directly proportional to blood flow. An example blood flow map of brain blood vessels obtained by LSCI is shown below in Figure 2-7 (Boas & Dunn, 2010):

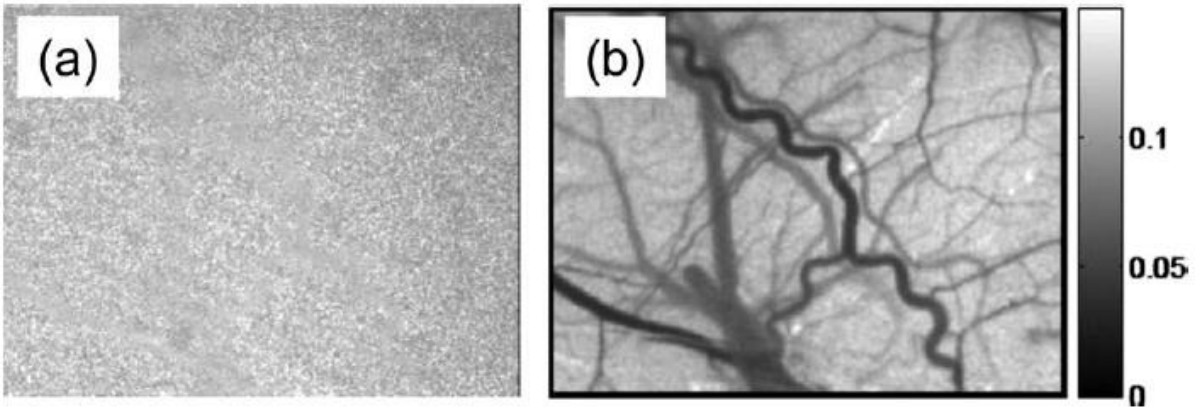

FIGURE 2-7 IN-VIVO SPECKLE CONTRAST EXAMPLE. A) SPECKLE INTERFERENCE PATTERN; B) INVERSE SPECKLE CONTRAST IMAGE VISUALIZING VESSEL BLOOD FLOW

Where (a) is the raw speckle image and (b) is the inverse squared speckle contrast image, $K_t$.

The main advantages of speckle contrast are the high spatial (micron) and temporal resolution which allow for visualization of individual blood vessels and flow perturbation identification on the order of milliseconds, due to the typical acquisition time being in the range of 10-20 milliseconds for a single speckle image. The downside of LSCI is the shallow penetration depth. Due to the wide-field nature of the technique and the high scattering properties of tissue, the typical LSCI image in the near-infrared range will be sample tissue only millimeters deep. Therefore, LSCI is most useful when probing surface tissues such as the skin or when tissue can be partially exposed, such as with in vivo animal models.

## 2.3 Diffuse Correlation Spectroscopy

Diffuse correlation spectroscopy is an optical imaging modality similar to LSCI where laser light speckle patterns are measured to quantify blood flow speed. However, DCS measures temporal fluctuations, whereas LSCI monitors spatial fluctuations. A point source signal is generated by a coherent laser source and propagated into the tissue of interest. Moving red blood cells within the tissue will scatter the light and reflect some of the light back to the tissue surface where the intensity of this reflected light is measured with a photodetector. The dynamic scattering of the moving blood cells causes the detected intensity to temporally fluctuate. The time scale of these fluctuations is quantified with the intensity temporal autocorrelation function of the collected light (Buckley et al., 2014) .

The motion of the blood cell scatterers is directly related to the unnormalized electric field temporal autocorrelation function ($G_1$), which itself follows a correlation diffusion equation (Boas et al., 1995) . The correlation diffusion equation is defined as:

$$(D\nabla^2 - \nu\mu_a - \frac{1}{3}\nu\mu_s' k_0^2 \alpha\langle \Delta r^2(\tau)\rangle)G_1(\underset{r}{\rightarrow},\tau) = -\nu S(\underset{r}{\rightarrow})$$

Where, $\nu$ is the speed of light in the tissue, $\mu_a$ is the tissue absorption coefficient, $\mu_s'$ is the tissue reduced scattering coefficient, $D = {}^{\nu}/_{(3\mu_s')}$ is the photon diffusion coefficient, $k_0$ is the wavenumber, $S(\underset{r}{\rightarrow})$ is the source light distribution and $\langle \Delta r^2(\tau)\rangle$ is the mean-square displacement of scatterers in delay time, $\tau$, which characterizes the scatterer movement. It has been shown that the diffusion model $\langle \Delta r^2(\tau)\rangle = 6D_B\tau$ fits the autocorrelation curves well for human muscle(Cheung et al., 2001) and brain tissue(J. Li et al., 2005) where $D_B$ is the effective Brownian diffusion coefficient. The combined term of $\alpha D_B$ is known as the blood flow index (BFI) and can be used to calculate relative blood flow (rBF) changes compared to a baseline flow index.

The point source and detector capability of DCS allows much deeper tissue to be probed (on the order of cm) as compared to LSCI (µm to mm). However, there is a trade-off in the spatial resolution (cm) with point detectors being used for DCS as compared with a camera wide-field detector being used for LSCI.

# 3. Preliminary Results

The following chapter contains excerpts from the journal article, “Quantification of perfusion and metabolism in an autism mouse model assessed by diffuse correlation spectroscopy and near-infrared spectroscopy”, published in the *Journal of Biophotonics*, July 30, 2021(Rinehart et al., 2021)

## 3.1. Autism Spectrum Disorder

As previously stated in section 1.1, there existed a need for a low-cost, non-invasive optical approach that is capable of measuring brain blood flow in the ASD mouse model. Our preliminary research has focused on adapting a custom-built diffuse correlation spectroscopy (DCS) system that was previously used in our human studies(Poon et al., 2020).

### 3.1.1 Materials and Methods

### 3.1.2 Animals

Three-month-old mice were sourced from Jackson Labs (Bar Harbor, ME, USA). The study groups contained 6 male C57BL/6J (control) and 6 male BTBR T+ Itpr3tf/J (ASD) mice of the same age. The groups will hereby be referred to using their common names of C57/B and BTBR, respectively. The BTBR mouse model was previously phenotyped to show symptoms and behaviors similar to the human form of ASD(Chadman et al., 2012; Meechan et al., 2015). The structural abnormality of an absent corpus callosum is believed to be a key component associated with the core behavioral problems of ASD(Stephenson et al., 2011; Wahlsten et al., 2003).

The heads of the mice were shaved and a chemical depilatory agent was applied to ensure that the imaging area was clear of hair. The hair removal procedure was performed 24 hours prior to imaging to allow time for any redness or swelling caused by minor skin irritation to subside.

Immediately prior to imaging, mice were anesthetized by gaseous administration of an isoflurane and oxygen mixture. To control for decreased blood flow caused by hypertension as a result of isoflurane administration, all mice were anesthetized and imaged on a precise schedule(Constantinides et al., 2011). Each mouse was incubated with 5% isoflurane at a flow rate of 300 ml/min for 2 minutes. The mice were then transferred to a nose cone where the isoflurane dose was reduced to 2.5% at the same flow rate. DCS measurements were taken 7 minutes after initial anesthesia administration and frequency domain measurements were taken 9 minutes after.

All procedures related to animal care were carried out with the approval of the Institutional Animal Care and Use Committee of Wright State University.

### 3.1.3 DCS Instrumentation

In this study, the DCS system consists of a continuous-wave laser source (785 nm CrystaLaser, Reno, NV, USA) with coherence length longer than 10 m, eight NIR-optimized single-photon counting modules (SPCM-NIR, Excelitas, QC, Canada), and a 8-

channel autocorrelator board (Correlator.com), of which one channel was used. A single multimode fiber (600 um core diameter, 0.39 numerical aperture (NA)) was used to guide the 785 nm laser light to the scalp and a singlemode fiber (5 um core diameter, NA of 0.13) collected the light emitted from the scalp to the single-photon counting modules, as shown below in (Figure 3-1 A). The separation distance between the source and detector fiber was set at 5 mm, with the detector fiber placed at the midpoint of the cerebral cortex and a translational stage was used to place the source fiber 5 mm anterior to the detector fiber, as shown below (Figure 3-1 B).

The optical parameters (absorption coefficient, µa, and reduced scattering coefficient, µs’) at 690 nm and 830 nm were resolved using a frequency-domain NIRS system (OxiplexTS, ISS Inc., Champaign, IL, USA). A custom probe with source-detector separations at 2, 4, 6, and 8 mm was fabricated using 400 um multimode source fibers and a single 1000 um detector fiber to allow probing optical property measurements at a similar depth as our DCS measurements. The optical properties measured at 830 nm were used as inputs for the BFI calculations from the DCS data.

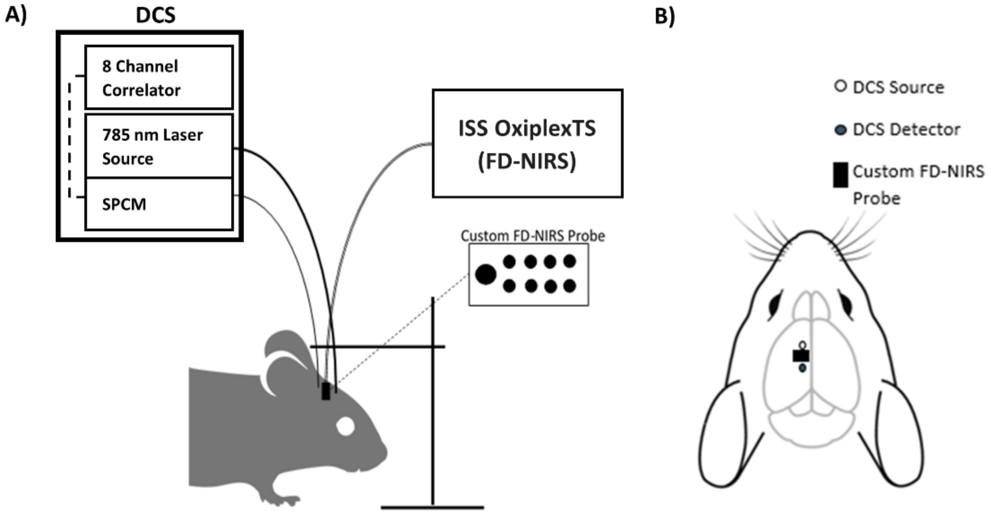

FIGURE 3-1 OPTICAL INSTRUMENTATION OF DCS AND FD-NIRS SYSTEMS. A) WHOLE SYSTEM OVERVIEW B) TOP-DOWN VIEW OF PROBE PLACEMENT ON MOUSE SCALP

### 3.1.4 Results

Results of the optical absorption coefficient (μa) and reduced scattering coefficient (μs’) results at 690 and 830 nm are summarized for the BTTR and C57/B6 groups in Figure 3-2. The following summary statistics in this section are presented in the form of the median ± standard deviation. For μa measurements at 690 nm (in Figure 3-2 A), the BTBR group had 0.24 ± 0.02 and the C57/B6 group had 0.22 ± 0.01 $cm^{-1}$. For $\mu_a$ measurements at 830 nm (in Figure 3-2 B), the BTBR group had 0.22 ± 0.02 cm-1 and the C57/B6 group had 0.20 ± 0.02 $cm^{-1}$. The Wilcoxon rank sum test did not show significant differences in $\mu_a$ between the groups at wavelengths of neither 690 nm (p = 0.56) nor 830 nm (p = 0.61) wavelengths (in Figure 3-2 C and in Figure 3-2 D). For reduced scattering coefficient ($\mu_s$’) measurements at 690 nm, the BTBR group had 8.50 ± 0.71

$cm^{-1}$ and the C57/B6 had 8.90 ± 0.98 $cm^{-1}$. The Wilcoxon rank sum test showed no significant differences in scattering at 690 nm (p = 0.85). For $\mu_s'$ measurements at 830 nm, the BTBR group had 6.30 ± 1.90 $cm^{-1}$ and the C57/B6 group had 6.10 ± 0.35 $cm^{-1}$. The Wilcoxon rank sum test showed no significant differences in the scattering coefficient at 830 nm (p = 0.70).

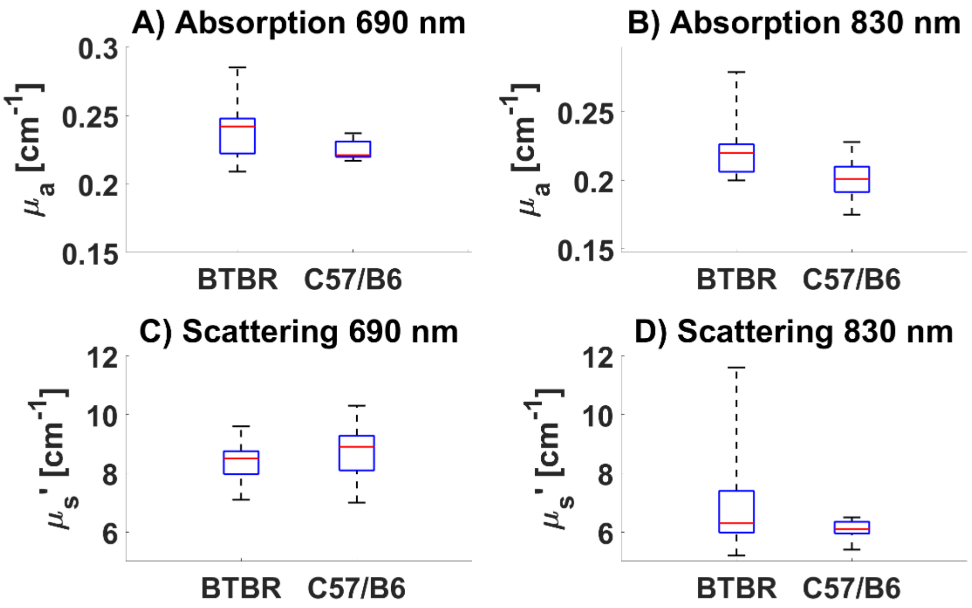

FIGURE 3-2 BOX AND WHISKER PLOTS PRESENTING GROUPED OPTICAL ABSORPTION AND SCATTERING MEASUREMENTS ON THE BTBR AND C57/B6 GROUPS RECORDED FROM THE FD-NIRS SYSTEM. BOX MIDLINES DENOTE MEDIAN VALUES OVER A 30 SECOND PERIOD. THE BOTTOM AND TOP EDGES OF THE BOX INDICATE THE 25TH AND 75TH PERCENTILES, RESPECTIVELY. WHISKERS EXTEND TO THE MOST EXTREME DATA POINTS (A) ABSORPTION COEFFICIENT (μA) MEASUREMENTS AT 690NM, NO STATISTICAL SIGNIFICANCE. B) ABSORPTION COEFFICIENT MEASUREMENTS AT 830 NM, NO STATISTICAL SIGNIFICANCE. C) SCATTERING COEFFICIENT MEASUREMENTS AT 690 NM, NO STATISTICAL SIGNIFICANCE. D) SCATTERING COEFFICIENT MEASUREMENTS AT 830 NM, NO STATISTICAL SIGNIFICANCE.

The dual-wavelength approach of the FD-NIRS system allows the calculation of cerebral hemodynamic parameters by assuming absorption originates mainly from oxygenated and deoxygenated hemoglobin concentrations ($C_{HbO}$, $C_{Hb}$). The resulting group averages for $C_{HbO}$ and $C_{Hb}$ are shown in Figures 3-3 A and B, respectively. $C_{HbO}$ and $C_{Hb}$ for the BTBR group were 69.0 ± 7.9 µM and 41.3 ± 10.8 µM, respectively, while for the C57/B6 group were 66.0 ± 9.0 µM and 40.6 ± 4.1 µM, respectively. The Wilcoxon rank sum test indicated that $C_{HbO}$ and $C_{Hb}$ did not show significant differences (*p*-values = 0.82, 0.70, respectively). Tissue oxygenation ($StO_2$) was recovered using hemoglobin parameters as shown in Figure 3-3 C. The results showed no significant difference between the groups (*p*-value = 0.82).

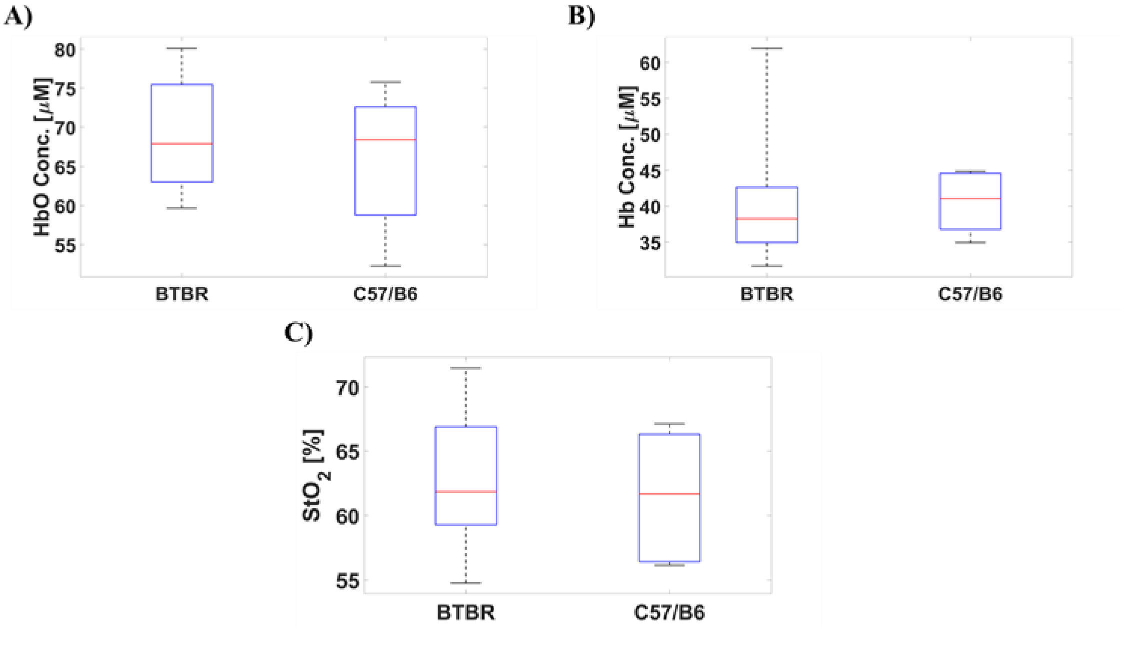

FIGURE 3-3 (A) OXYGENATED HEMOGLOBIN AND B) DEOXYGENATED HEMOGLOBIN MEASUREMENTS FOR BTBR AND C57/B6 MICE. WILCOXON RANK SUM DID NOT INDICATE STATISTICAL DIFFERENCES ($P > 0.05$) FOR GROUP COMPARISONS IN BOTH (A) AND (B). (C) TISSUE OXYGEN SATURATION CALCULATED FROM HEMOGLOBIN PARAMETERS. WILCOXON RANK SUM INDICATED THAT THERE WAS NO SIGNIFICANT DIFFERENCE BETWEEN THE TWO GROUPS ($P > 0.05$).

As shown above, the optical property measurements from the FD-NIRS device showed a high amount of variance in certain cases. The absorption and scattering measurements taken at 830 nm were used as inputs when fitting for blood flow index (BFi). Therefore, two sets of optical properties were used when fitting for BFi. The first case, shown below in Figure 3-4 A, fits for BFi using distinct optical properties for each mouse group, taken as the median values shown in Figures 3-2 B and 3-2 D for absorption and scattering, respectively. The median BFi for the BTBR group of (1.22 ± 0.49) * $10^{-8}$ $cm^2/s$ was significantly lower than the median BFi for the C57/B6 group of (1.93 ± 0.80) *$10^{-8}$ $cm^2/s$ according to the Wilcoxon rank sum test, p = 0.026. The second case, shown in Figure 3-4 B, fits the BFi using the mean $\mu_a$ and $\mu_s'$ for the entire mouse population ($\mu_{a, 830nm}$ = 0.21 $cm^{-1}$, $\mu_s'_{830nm}$ = 6.71 $cm^{-1}$). The median BFi for the BTBR group of (1.16 ± 0.26) * $10^{-8}$ $cm^2/s$ was significantly lower than the median BFi for the C57/B6 group of (1.93 ± 0.73) *$10^{-8}$ $cm^2/s$ according to the Wilcoxon rank sum test, p = 0.001.

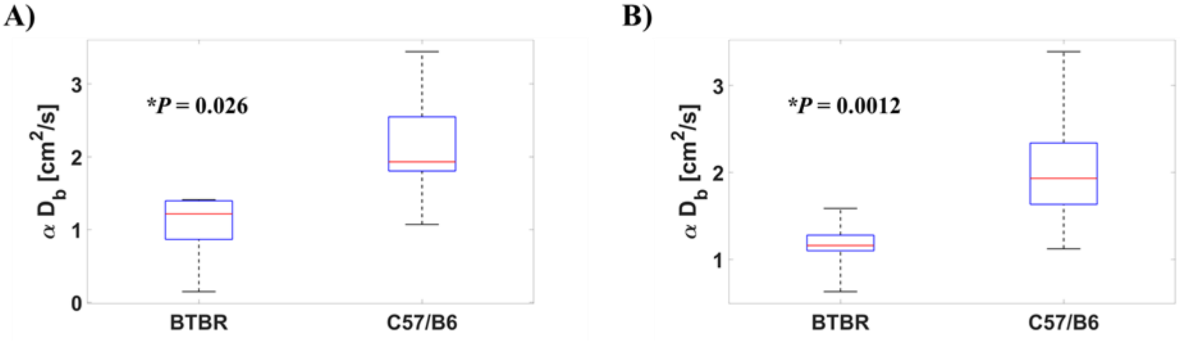

**FIGURE 3-4 GROUPED BLOOD FLOW INDEX (BFI) MEASUREMENTS OF BOTH MOUSE GROUPS IN TERMS OF ADB. (A) GROUPED AVERAGE BFI MEASUREMENTS WHERE THE OPTICAL PROPERTIES USED AS INPUT FOR THE BFI FITTING WERE INDEPENDENT FOR THE TWO GROUPS, TAKEN FROM THE AVERAGED ABSORPTION AND SCATTERING VALUES AT 830 NM SHOWN IN FIGURE 2. (B) GROUP AVERAGE OF BFI MEASUREMENTS WHERE OPTICAL PROPERTY VALUES USED IN FITTING WERE THE SAME FOR ALL MICE. TAKEN AS THE AVERAGE ABSORPTION AND SCATTERING RESULTS FROM THE FD-NIRS MEASUREMENTS FOR ALL MICE (μA, 830NM = 0.21 CM-1, μS', 830NM = 6.71 CM-1).**

Parameters of blood flow and hemoglobin concentration can be further combined to estimate the cerebral metabolic rate of oxygen ($CMRO_2$), which reflects the differences between oxygen input and output through a specific region of the brain of interest (Verdecchia et al., 2013). The standard expression for estimating $CMRO_2$ was used(Chong et al., 2015): $CMRO_2 = OE * CBF$ ,

where $OE = (1 - (StO2/SaO2))/\gamma$ , is the oxygen extraction defined as the difference between arterial and venous oxygen saturation. OE was calculated using equation above where arterial oxygen saturation ($SaO_2$) and cerebral arteriovenous mixing fraction (γ) are assumed to be constant values of 0.97 and 0.75, respectively(Culver et al., 2016). The resulting $CMRO_2$ group averages are shown below in Figure 3-5. $CMRO_2$ for the BTBR group was estimated as 52.4 ± 16.6 µmol/100 g/min and $CMRO_2$ for the C57/B6 group was estimated as 177.2 ± 45.8 µmol/100 g/min. The difference in $CMRO_2$ was significant between the two groups, (Wilcoxon rank sum, *p* = 0.015).

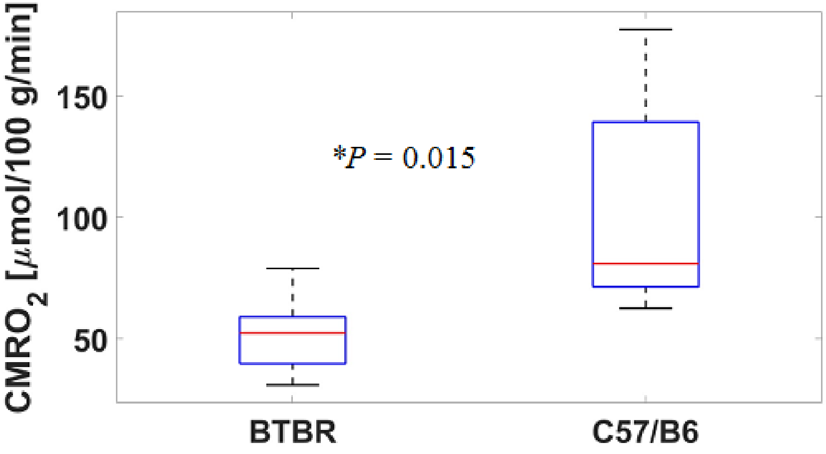

FIGURE 3-5 GROUPED CEREBRAL METABOLIC RATE OF OXYGEN (CMRO2) ESTIMATED FOR BOTH MOUSE GROUPS IN TERMS OF µMOL/100 G/MIN.

The decreased blood flow in the ASD mouse model is consistent with the results seen in past research of the BTBR model measured by the optical methods(Abookasis et al., 2018) . Recent reviews have also shown supporting evidence for cerebral hypoperfusion from both PET/SPECT and fMRI studies(Philip et al., 2012; Zürcher et al., 2015). The prevailing theory for this pathology is a dysfunctional vasodilation response in the autism cerebral arteries. A healthy brain will exhibit CBF that is largely unchanged over time due to the combined effect of the basal tone in smaller arterioles and the mechanical vascular resistance of larger arteries(Zürcher et al., 2015). When the cerebral metabolic demands increase in an area, such as during an activity or task that recruits neurons from that brain region, blood vessels dilate to reduce resistance and increase blood flow(Faraci & Heistad, 1990). In ASD there appears to be a lack of this normal compensatory dilation and increased blood flow when engaged in a task, such as speaking or focusing on solving a problem(Allen & Courchesne, 2003; Ohnishi et al., 2000). When the blood vessels do not properly dilate, the smaller cross-sectional area of the lumen can cause restricted blood flow.

There are also possible intrinsic structural explanations for these hypoperfusion results. Exacerbated inflammatory responses have been extensively documented in ASD patients(Kern et al., 2016; Theoharides et al., 2016; Vargas et al., 2005). The resulting intracranial pressure can potentially cause mechanical vasoconstriction and, as a result, decreased blood flow(Morgan et al., 2010; Vargas et al., 2005). Furthermore, evidence from recent research suggests that most children with ASD also exhibit ongoing general neuroinflammatory disorders(Kern et al., 2016) . The increased absorption observed in the BTBR group could also be a result of neuroinflammation. The increase in local tissue volume due to inflammation would result in an increase in chromophore concentration (in the form of hemoglobin and water) that would increase the measurement of the absorption coefficient.

The lack of a significant difference in the scattering parameter between the BTBR and C57/B6 models is contrary to expectations based on the decreased neurogenesis cell count shown in the previous literature(Abookasis et al., 2018). This could be due to the variations in the quantification accuracy by the multi-distance method but could also be due to the physiological difference between the two mouse models. If we write $\mu_s'$ = $a\lambda^{-b}$ for the Mie scattering representation, the Figure 2B shows that b parameter (related to scattering power) shows a smaller trend in autistic group (BTBR) than the control group (C57/B6). We will investigate this further by fitting both a and b from the measurements having additional wavelengths. Further investigation should also be conducted in terms of physiological measurements of differences in scalp and skull thicknesses between the two models.

The closest study to this study is by laser speckle imaging  performed by Abookasis et al(Abookasis et al., 2018). on the same animal groups. Although laser speckle imaging probing depth is superficial, they also found that blood flow was significantly lower, and the difference in $CMRO_2$ was not statistically different (Autism group had lower $CMRO_2$). Since DCS and FD-NIRS have been implemented for measuring cerebral blood flow, oxygenation and metabolism in children and adults(Buckley et al., 2014; Durduran &

Yodh, 2014; Mesquita et al., 2011), our approach and findings are expected to be clinically more relevant.

As for the limitations of the study, although we try to keep the mice on the same physiological conditions, there is a possibility that temperature, heart rate, and other physiological variations may affect the results and cause larger variations in our measurements. The optical probe was custom-built in the lab, and ferrule fibers were one of the limiting factors for the compact probe, which FD-NIRS measurements could be more prone to errors due to multi-distance method and could lead to variations in absorption and scattering parameter quantification. These variations can propagate to the estimation of hemoglobin concentrations, metabolism, and scattering amplitude and power.  This limitation may be eliminated or reduced by using bare fibers that are widely available commercially. Furthermore, heterogeneity was not investigated in this study; a depth-resolved imaging-based system may be more suitable for this aim and can be further pursued in the near future.  Although here we mainly focused on quantification of baseline values of the parameters, the information could be enriched by investigating additional biomarkers based on resting state functional connectivity and low-frequency oscillations in these parameters, as demonstrated before(Cheng et al., 2019; Cornew et al., 2012; Y. Li et al., 2018; Y. Li & Yu, 2016; Zang et al., 2007; H. Zhu et al., 2014).

## 3.2 Huntington’s Disease

A preliminary study was  conducted on the R6/2 mouse model of Huntington’s disease. The goal here was to correlate the decrease in force generation in the Huntington’s disease mouse model with an observed change in blood flow. DCS point source imaging was used to monitor changes in BFI after repeated tetanic contractions in the R6/2 mouse model and compared with a wild type (WT) counterpart.

### 3.2.1 Methods

Mice were anesthetized with isoflurane using a low-flow anesthesia system (SS-01, Kent Scientific, Torrington, CT), with body temperature maintained at ~35 ℃ using a heat lamp and temperature probe. Plantar flexor muscles (including the lateral and medial gastrocnemius, plantaris, and soleus muscles) and sciatic nerve were exposed by removing the surrounding skin. To minimize the influence of adjacent muscles, the common peroneal and tibial nerves were crushed. During surgery, the muscles were bathed in physiological saline to prevent them from drying out. The mice were then transferred to a custom Sylgard-filled platform and mounted on a micromanipulator (XR25/M, Thorlabs, Newton, NJ). The leg was stabilized to prevent movement. The proximal end of the plantar flexor muscles (Achilles’ tendon) was attached to the lever of the force transducer (300D-305C dual-mode muscle lever, Aurora Scientific, Ontario, Canada) using 5.0 or 6.0 silk suture and a modified Miller’s knot. The optimal length was obtained by measuring the maximum twitch force while lengthening the muscle using the micromanipulator.

Nerve-evoked contractions were stimulated with platinum electrodes resting on the sciatic nerve. Direct muscle contractions were stimulated using platinum electrodes placed above and below the plantar flexor muscles. For muscle-stimulated contractions, neuromuscular transmission was blocked using ~150 µl of 0.5 mg/ml α-bungarotoxin (α-BTX) injected into the gastrocnemius muscles. After injection of α-BTX, neuromuscular transmission was confirmed to be blocked by ensuring that the twitch force was 25% of the maximum nerve-stimulated twitch. Stimulus amplitude and the pulse width was ≤5 V at 1 ms or ≤50 V at 1.5 ms for nerve stimulated and muscle-stimulated contractions, respectively. A Dagan S-900 Stimulator and S910 Stimulus Isolation Unit were used for stimulation

A repeated stimulation protocol was developed that consisted of sweeps of 10 tetani to study muscular fatigue and the response to blood flow due to repeated contractions. The nerve was stimulated with 20 pulse trains at 30 Hz. Stimulus amplitude and the pulse width were ≤5 V at 1 ms. Sweeps of 10 trains were stimulated with 2 seconds between trains. There was two minutes of rest between sweeps, and five sweeps were performed in total. The whole protocol consisted of five sweeps with 10 trains at 30 Hz. From now on, this protocol will be referred to as a 10x5 repeated tetani protocol. The 10x5 repeated tetani protocol was immediately followed by 44 min of rest. During the rest period, some baseline and a single twitch were recorded every 2 min.

The same custom-built DCS device described previously in the ASD preliminary results was used here with the sole change being the source-detector separation was reduced to 3 mm to ensure that most of the detected photons traveled through the belly of the exposed muscle.

### 3.2.2 Results

Representative BFI traces are shown below for a WT mouse (Figure 3-6, left) and a R6/2 mouse (Figure 3-6, right) captured immediately after contractile phases that occurred at time = 120, 180, 240, 300 and 360 seconds.

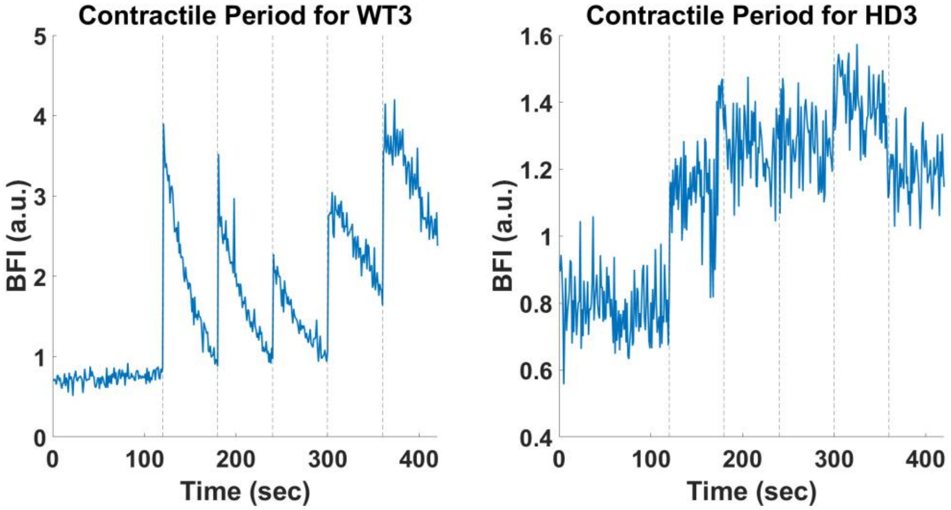

FIGURE 3-6 REPRESENTATIVE BFI MEASUREMENTS FOR WT (LEFT) AND HD (RIGHT) MICE

The WT mouse exhibited the expected increase in blood flow post-contraction. The hampered increase in blood flow post contraction for the R6/2 mouse suggested possible vascular dysfunction. Findings have shown that the skeletal muscle of the R6/2 model is not releasing nitric oxide through the myogenic mechanism. To quantify the blood flow difference, we measured the percent increase in BFI for each mouse and averaged the percent increase across all five post contraction phases. Results for the individual mice and the group mean results for both groups are shown below in Figure 3-7 (left and right, respectfully).

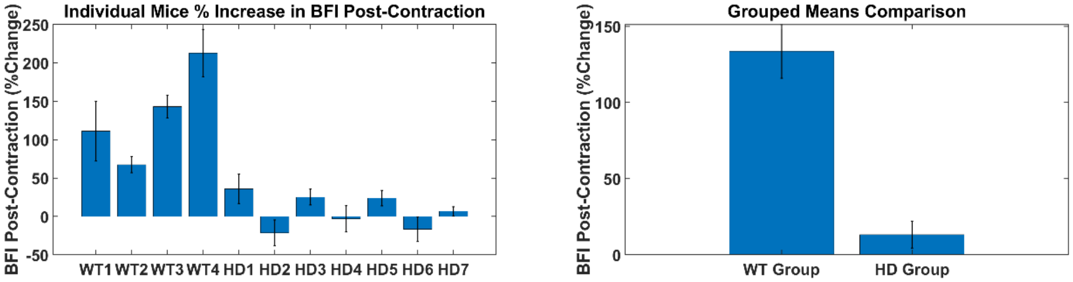

FIGURE 3-7 PERCENT INCREASE QUANTIFICATION FOR INDIVIDAL (LEFT) AND GROUP MEAN (RIGHT) DATA

Dynamic blood flow changes also showed potential differences between the two groups. Specifically, the blood flow curves observed during the post-contractile recovery periods presented with much higher decay rates in the WT group compared with the R6/2 group. To quantify these decay rates, the 60 seconds of blood flow data immediately following each contraction was fitted to a single exponential decay model via a least-squares nonlinear fitting technique (lsqcurvefit, MATLAB): $BFI = a * e^{-bt}$. Representative results for the five recovery periods and resulting exponential fits are shown below for a WT (Figure 3-8.A) and R6/2 (Figure 3-8.B) model.

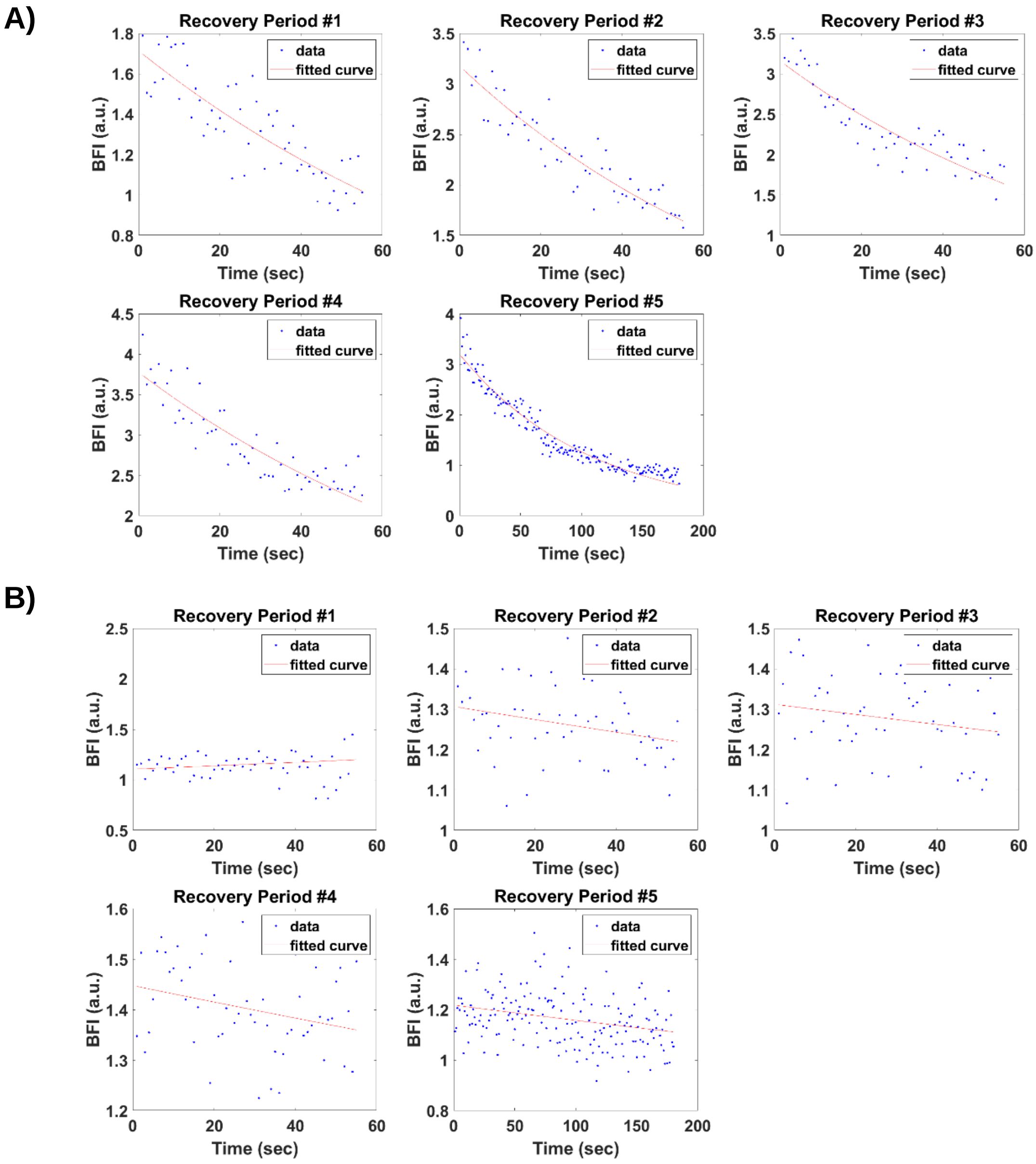

FIGURE 3-8 REPRESENTATIVE BLOOD FLOW DECAY AND ASSOCIATED EXPONENTIAL FIT RESULTS FOR A WT (A) AND R6/2 (B) MODEL

Next, the decay rate coefficients ‘b’ were tested for statistical significance with a Wilcoxon rank sum test ($p << 0.001$) and the grouped results are shown below in Figure 3-9.

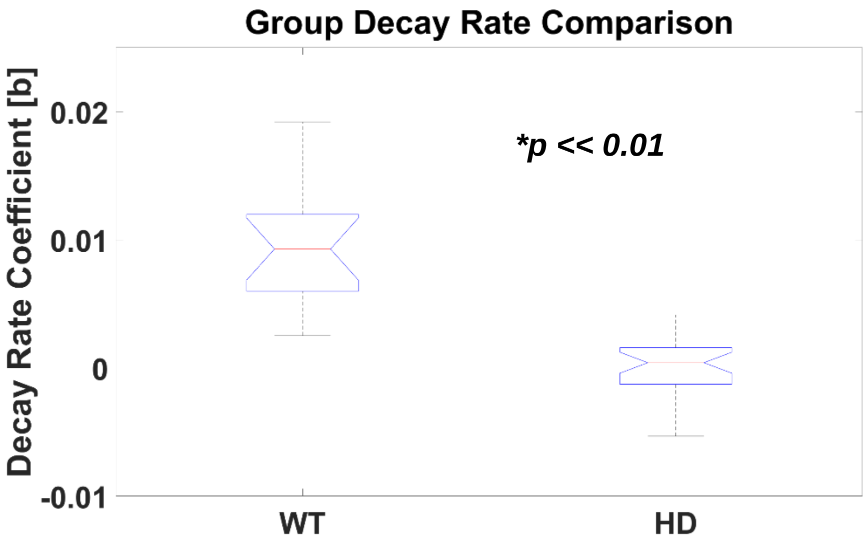

FIGURE 3-9 GROUPED COMPARISON FOR THE POST CONTRACTILE BLOOD FLOW EXPONENTIAL DECAY COEFFICIENT

These results are encouraging in that they show decreased blood flow post-contraction and hampered blood flow recovery in the R6/2 Huntington's mouse model. However, the point source and detector measurement technique used was unable to capture blood flow measurements during the contraction phase of the experiment due to the movement of muscle contraction that interfered with the positioning of the point source. Therefore, a non-contact blood flow monitoring system was needed.

# 4. Non-contact LSCI + SFDI

A noncontact LSCI + SFDI system was constructed to address the shortcomings of the contact DCS measurements,. A noncontact camera-based system allows blood flow measurements to be obtained without interruption during electrically induced muscular contractions, addressing the primary downside of  contact probe DCS measurements. Blood oxygenation consumption and re-oxygenation was also of interest due to skeletal muscle myopathy(CM et al., 2007), but also the pulmonary dysfunction observed in HD that could manifest itself in decreased oxygen supply to the muscles(Reyes et al., 2014). Therefore, a multiwavelength SFDI system was deployed to image tissue optical properties and oxygen saturation. In addition, a camera-based system enables two-dimensional maps to be obtained. Thus, allowing spatially dependent analysis to be performed. The instrumentation and dual application of LSCI and SFDI are detailed in this chapter.

## 4.1 SFDI Instrumentation

The SFDI system constructed for this application was based on the designs of the “openSFDI” project, kindly provided by the Biomedical Optical Technologies Lab at Boston University(Applegate et al., 2020). A system overview with labelled components is shown below in Figure 4-1. The essential components of the SFDI system are the light sources, structured light array, and camera. The system was constructed using three light emitting diodes (LEDs) as light sources. The emission wavelengths of these LEDs are centered at 660, 730 and 850nm (Thorlabs: M660D2, M730D2, M850D2, respectively).

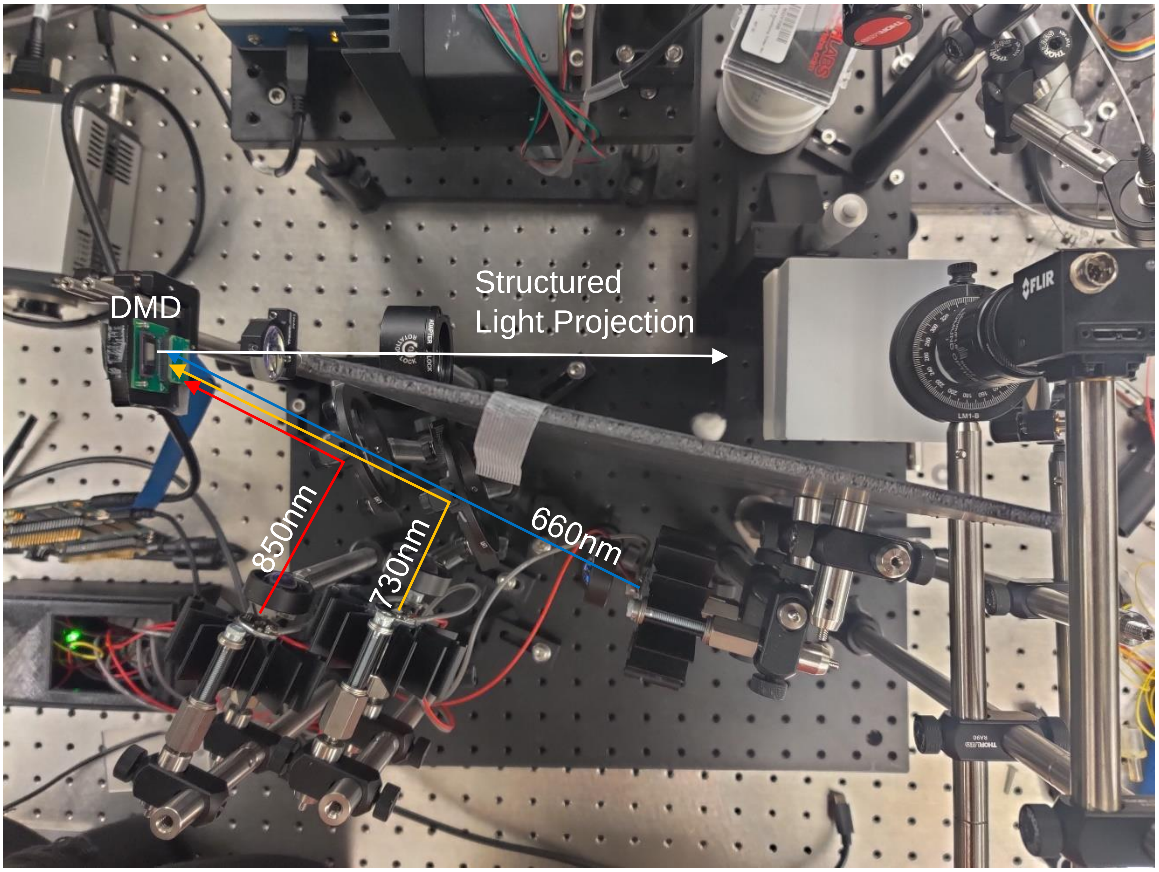

FIGURE 4-1 OPTICAL PATHS OF WIDE-FIELD SFDI SYSTEM

Multiple source wavelengths allow for the calculation of oxygenated and deoxygenated hemoglobin concentrations. A digital micromirror device (DMD) was used to generate the structured light array in this system (DMD: DLP4500NIRFQE and Controller Board: LC4500, Keynote Photonics). The camera used in this system was a Blackfly S USB3 (Teledyne FLIR, model: BFS-U3-04S2C-CS).

The structured light image is projected onto the imaging field of view (FOV) through a multiple lens setup. First, 16 mm collimating lenses are used to focus the emission of each LED onto the surface of the DMD. In order to combine the three LEDs onto a single optical path a pair of 700nm and 800nm shortpass dichroic mirrors are used to reflect the 660nm and 730nm LED emissions towards the DMD, respectively. Once the focused light reaches the DMD a structured light pattern will be reflected towards the imaging FOV. After reflecting off of the DMD the light has become divergent; therefore, the light is passed through an achromatic lens to focus the structured light onto a 45-degree angled mirror, which reflects the light onto the imaging FOV. From this, the light interacts with the tissue or sample of interest and, depending on the tissue properties, a portion of the light is reflected towards the camera. The reflected light passes through a 35 mm fixed focal length lens before being deposited onto the camera sensor.

### 4.1.1 SFDI System Validation

Before this system was applied in vivo, it was necessary to validate the quantification accuracy on tissue phantoms with calibrated optical properties. The first step in this process is to calibrate the spatial light projections of the system. Due to the nature of the open optical setup, any slight changes in the position or angle of the optics can cause deviations in the geometry of the structured light projection onto the sample. Therefore, the data collection during the contractile periods must be omitted. The geometry of the structured light projection is directly related to the spatial frequency of the patterns used in SFDI. Therefore, there is a scaling factor that relates the spatial frequency of the patterns on the surface of the DMD to the spatial frequency of the projected pattern on the surface of the sample. This scaling factor was calculated through the following process, visualized in Figures 4-2 and 4-3. 1). Generate an image file containing a 100 x 100 pixel black square on a white background 2) Project the 100 x 100 pixel square onto the sample 3) Use a ruler to measure the vertical FOV of the camera sensor on the surface of the sample ($FOV_v$) and divide the vertical resolution of the camera ($Res_v$) by this value to find the FOV of each pixel on the sample, $FOV_{pix} = Res_v/FOV_v$, units pixels/millimeter 4) Capture an image of the 100 x 100 pixel square and measure the height of the square in terms of camera pixels, called 'w' 5) Determine the square height in millimetres, $h = w / FOV_{pix}$ 6) Finally, the conversion factor, k, can be determined by dividing the height of the square, in terms of DMD pixels, by the height of the square in millimetres, k = 100 / h. The factor k now is in terms of DMD pixels per spatial length of the sample. Once this conversion factor was determined, we could easily construct digital images for our sinusoidal patterns based on the desired spatial frequency of those projections on the sample.

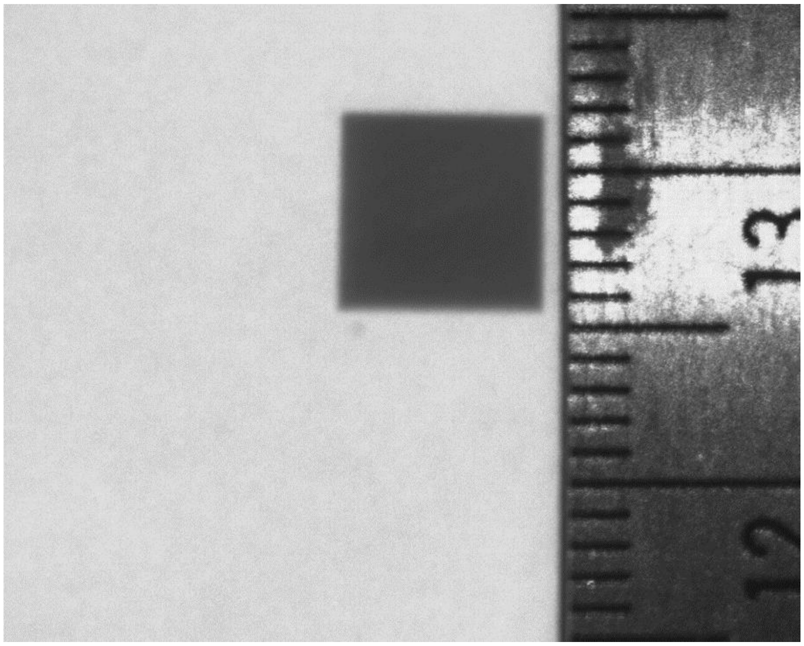

FIGURE 4-2 STEP 1-3) GENERATE 100 X 100 SQUARE PROJECTION. PROJECT SQUARE ONTO SAMPLE. MEASURE THE FOV OF THE CAMERA, 20.5 MM HERE.

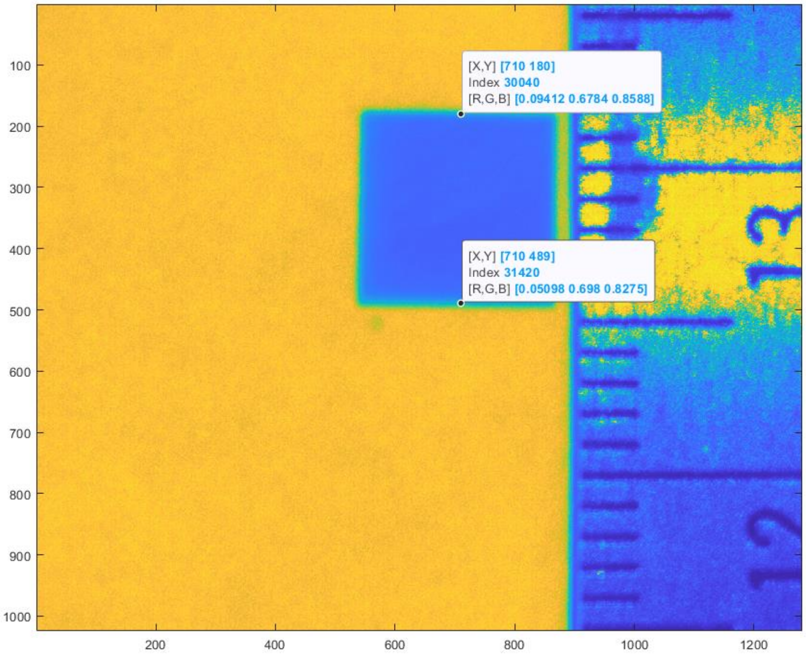

FIGURE 4-3 STEP 4) CAPTURE AN IMAGE AND MEASURE THE SQUARE WIDTH IN CAMERA PIXELS, 309 PIXELS HERE

The next step in the validation process for SFDI was to measure the quantification accuracy on phantoms of known optical properties. Before the SFDI imaging tests could be performed, we had to decide which spatial frequencies to use for our projections. The approach for this was to first simulate a diffuse reflectance ($R_d$) curve using the standard analytic diffusion approximation(Cuccia et al., 2009) and visualize the results as shown below in Figure 4-4.

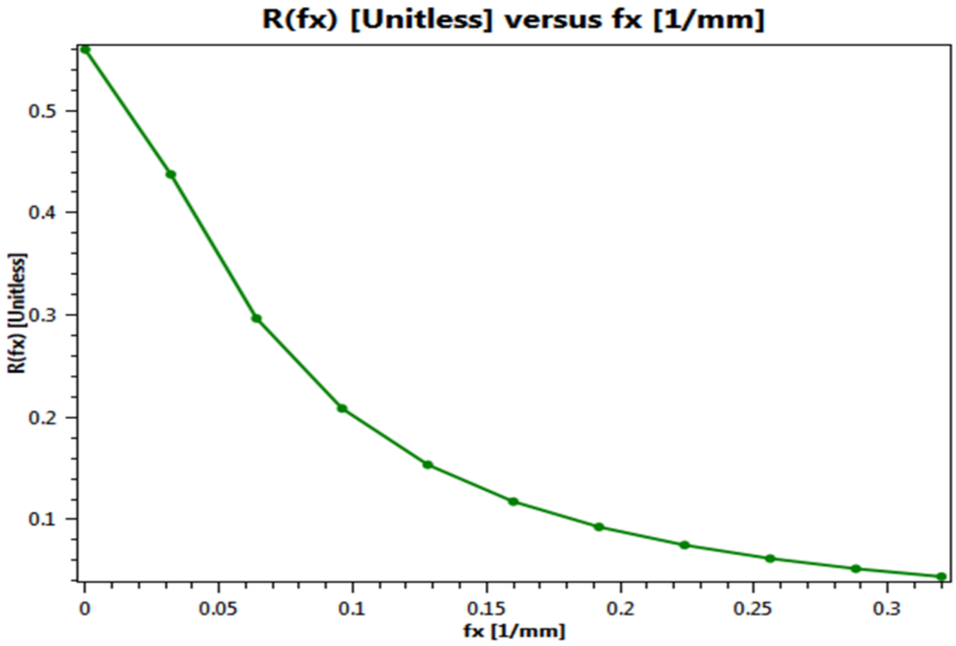

FIGURE 4-4 DIFFUSE REFLECTANCE SIMULATION RESULTS FOR A SPATIAL FREQUENCY RANGE FX = 0 - 0.3196 MM-1. ABSORPTION COEFFICIENT = 0.01 MM-1 AND REDUCED SCATTERING COEFFICIENT = 1.0 MM-1 FOR THE SIMULATION.

Based on this simulation, we choose spatial frequency and three phase shit approach to test for quantification accuracy. Three spatial frequencies are preferred for reconstruction to allow for a relatively low spatial frequency (more sensitive to absorption), a relatively high spatial frequency (more sensitive to scattering) alongside the necessary DC illumination pattern, where spatial frequency is equal to zero. The spatial frequency triplets tested in our validation procedure were as follows: (1) [0,0.0556,0.3196] mm-1 (2) [0,0.1612,0.2668] mm-1 and (3) [0,0.0556,0.082]. Reflectance images for these spatial frequencies were collected at an illumination wavelength of 660 nm on five liquid phantoms. The optical properties of these phantoms were controlled by diluting precise amounts of India ink, to control scattering, and intralipid, to control scattering, in water. The absorption coefficient of the five phantoms was set at 0.005, 0.010, 0.015, 0.020, and 0.025 mm$^{-1}$. The scattering coefficient was kept constant at 1.0 $mm^1$. The absorption coefficient was varied to simulate changes in absorption that occur when total hemoglobin concentration and tissue oxygen saturation change as a result of skeletal muscle contractions. Each of these spatial frequencies was collected using 660 nm illumination and the calibrated $R_d$ curve shown below in Figure 4-5 was recovered by using the $\mu_a$ = 0.015 $mm^{-1}$ phantom as a reference.

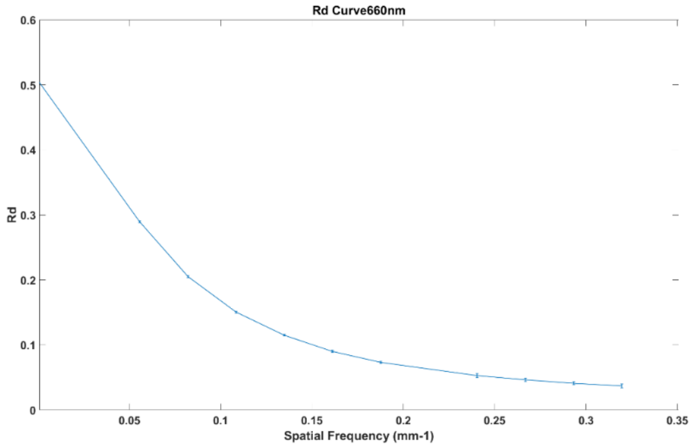

FIGURE 4-5 DIFFUSE REFLECTANCE CURVE RECOVERED DURING SFDI VALIDATION TEST

The optical properties of each liquid phantom were fitted from the spatial frequency triplets using the fitting procedure detailed earlier in Chapter 2.1.2. Triplet #1 [0,0.0556,0.3196] mm-1 returned the most accurate results for $\mu_a$ showing a standard error of 11.41% across all five levels of titration and 1.34% across the middle three levels of titration. Triplet #2 [0,0.1612,0.2668] mm-1 showed a standard error of 76.24 % across all five levels of titration and 95.01% across the middle three levels of titration. Triplet #3 [0,0.0556,0.082] mm-1 showed a standard error of 3.96% across all five levels of titration and 4.78% across the middle three levels of titration. The $\mu_a$ results are shown below in Figure 4-6 where the blue trace shows the $\mu_a$ data measured by the SDFI system and the red trace shows the optical properties of the phantom, which were measured by a commercial FD-NIRS system (OxiplexTS, ISS). Based on the results, both triplet #1 and triplet #3 appear to be viable options for this system. However, when SDFI is performed in vivo, the optical properties of the reference phantom will be prepared as closely to those of the target tissue as possible. Therefore, the quantification accuracy for the middle 3 titration steps, where the absorption coefficient of the reference phantom is within 0.005 $mm^{-1}$ of the titrated sample, is given increased consideration. Triplet #3 has the lowest standard error for the middle 3 titration steps (1.34%). The spatial frequencies of this triplet will be used in the future while performing SFDI in vivo.

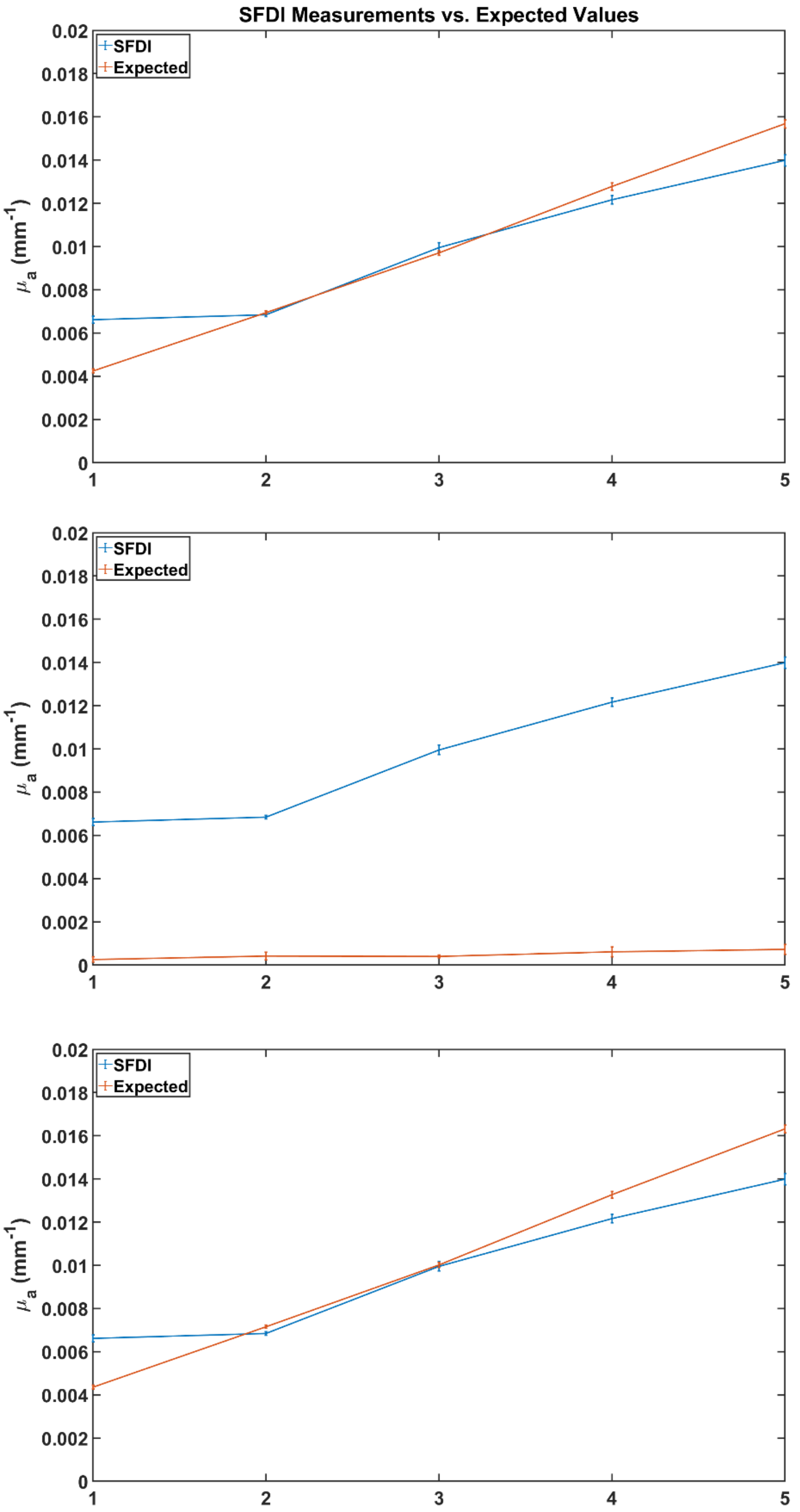

**FIGURE 4-6 ABSORPTION COEFFICIENT RESULTS FOR SFDI (BLUE) SHOWN COMPARED TO THE COMMERCIAL FD-NIRS SYSTEM (BLUE). PLOTS ARE ARRANGED FROM TOP TO BOTTOM AS: TRIPLET 1, TRIPLET 2, TRIPLET 3**

## 4.2 Laser Speckle Contrast Imaging

### 4.2.1 Instrumentation

Compared to SFDI, the instrumentation required for LSCI is rather simple. The components required to perform speckle contrast imaging are a laser source, camera, and an aperture. For our LSCI system we used the same camera and 35 mm fixed focal length lens described previously in Section 5.1. This allowed performing sequential SFDI and LSCI measurements, then performing a combined pixel-wise analysis. For the LSCI laser source we used a 785 nm, 70 mW, long coherence (> 10 meters), diode-pumped continuous wave laser (Compact Red, Crystalaser). A multimode optical fiber (400 micrometer core, Thorlabs M99L01) was used to guide the light from the laser to be centered under the camera FOV, as shown below in Figure 4-7. The light was cross-polarized and set at an angle of +20 degrees in relation to the camera axis to avoid back-reflection.

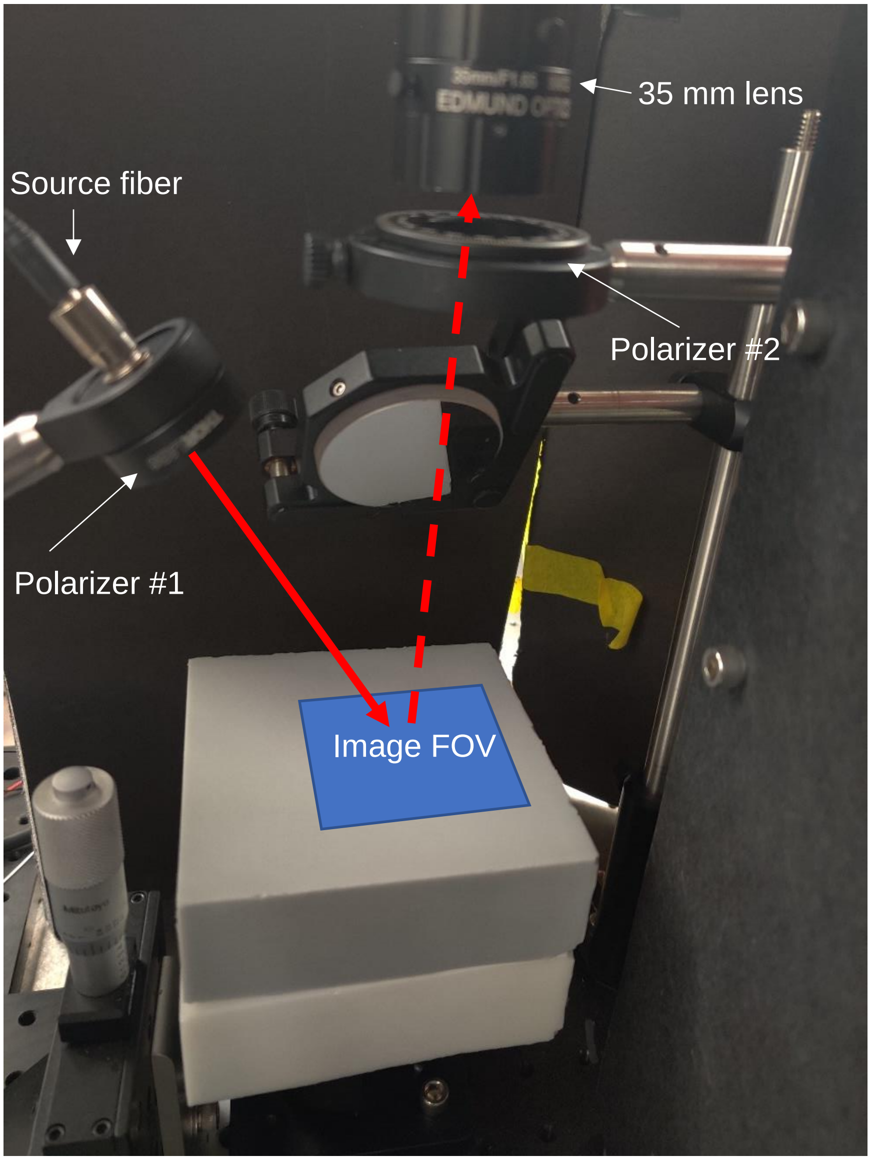

FIGURE 4-7 LASER SPECKLE CONTRAST IMAGING SETUP, SHOWING THE SOURCE LIGHT PATH (RED, SOLID) AND REFLECTED LIGHT PATH (RED, DOTTED)

### 4.2.2 LSCI Validation

Before using the LSCI system in vivo, a calibration and validation procedure was performed. First, the size of the individual speckles must be calibrated. The size of the speckles imaged on the camera, $\rho_{speckle}$, is given by (Fercher & Briers, 1981):

$$\rho_{speckle} = 2.44\lambda(1 + M)f/\#$$

Where, $\lambda$ is the wavelength of the light, M is the magnification of the imaging system, and f/# is the f-number of the system. Magnification is defined as the ratio of the camera sensor size to the FOV of the image, M = 0.2 in this system. The f-number is defined as the ratio of the camera focal length to the diameter of the aperture. By varying the aperture diameter, the f-number of this system could be varied from f/# = 1.65 – 22. For our case, the light wavelength is confined in the NIR region, and the magnification of the system was previously calibrated for the SFDI imaging path. Therefore, the f-number of the system is the primary factor we changed to alter the speckle size. The 35 mm lens on the camera was implemented with a variable aperture, allowing the f-number to be swept from 1.65 – 22. It has been previously shown that LSCI must satisfy the Nyquist sampling criteria(Duncan et al., 2008). Therefore, each speckle must be sampled by at least two pixels, that is, the minimum speckle size must be two times larger than the camera pixel size: $\rho_{speckle} \geq 2^{*} \rho_{pixel}$.

Empirically, under sampling manifests as a drop-off in speckle contrast as the speckle size falls below two pixels in diameter, as shown below in Figure 4-8.

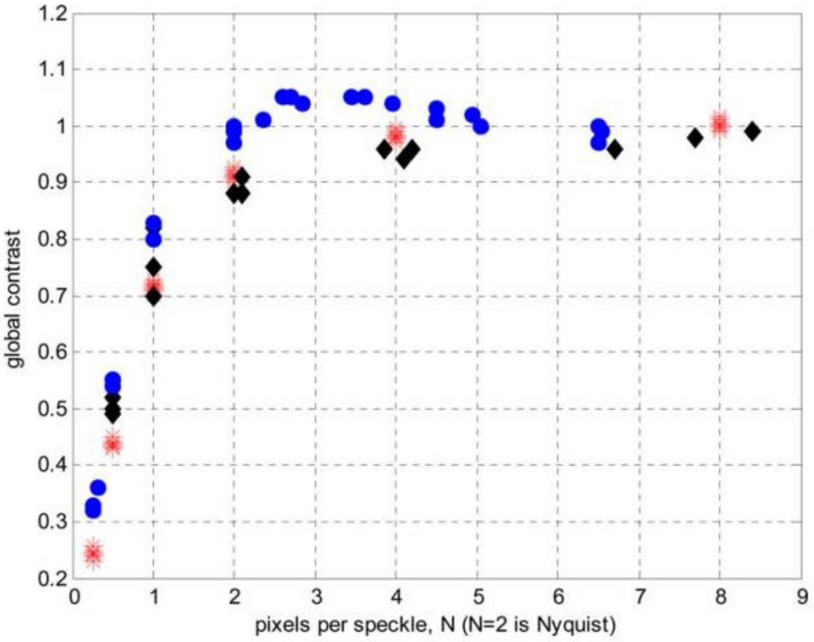

FIGURE 4-8 SIMULATED EFFECT OF PIXEL SIZE VS SPECKLE CONTRAST, FROM KIRKPATRICK ET AL. "DETRIMENTAL EFFECTS OF SPECKLE-PIXEL SIZE MATCHING IN LASER SPECKLE CONTRAST IMAGING" (2008).

As the speckle size decreases below two pixels in diameter, the global speckle contrast, and therefore the image contrast, drops exponentially. However, the global contrast plateaus once the speckle size is greater than or equal to 2 pixels. Increasing the speckle size above two pixels gives no further increase in resolution, but does result in lower spatial resolution given that the size of the kernel must be increased during analysis to compensate for the larger speckles. Given that a speckle size of two pixels is optimal, the system was calibrated to achieve this.

Measuring the speckle size manually was impractical and doing so algorithmically would be prone to inaccuracies caused by noise in the image. Given that the contrast vs. speckle size relationship is known, we estimated the speckle size by adjusting the f-number to be consistent in the notation of the system and observing the resulting speckle contrast at each step. The resulting speckle images and calculated speckle contrast are shown below in Figure 4-9 and Figure 4-10.

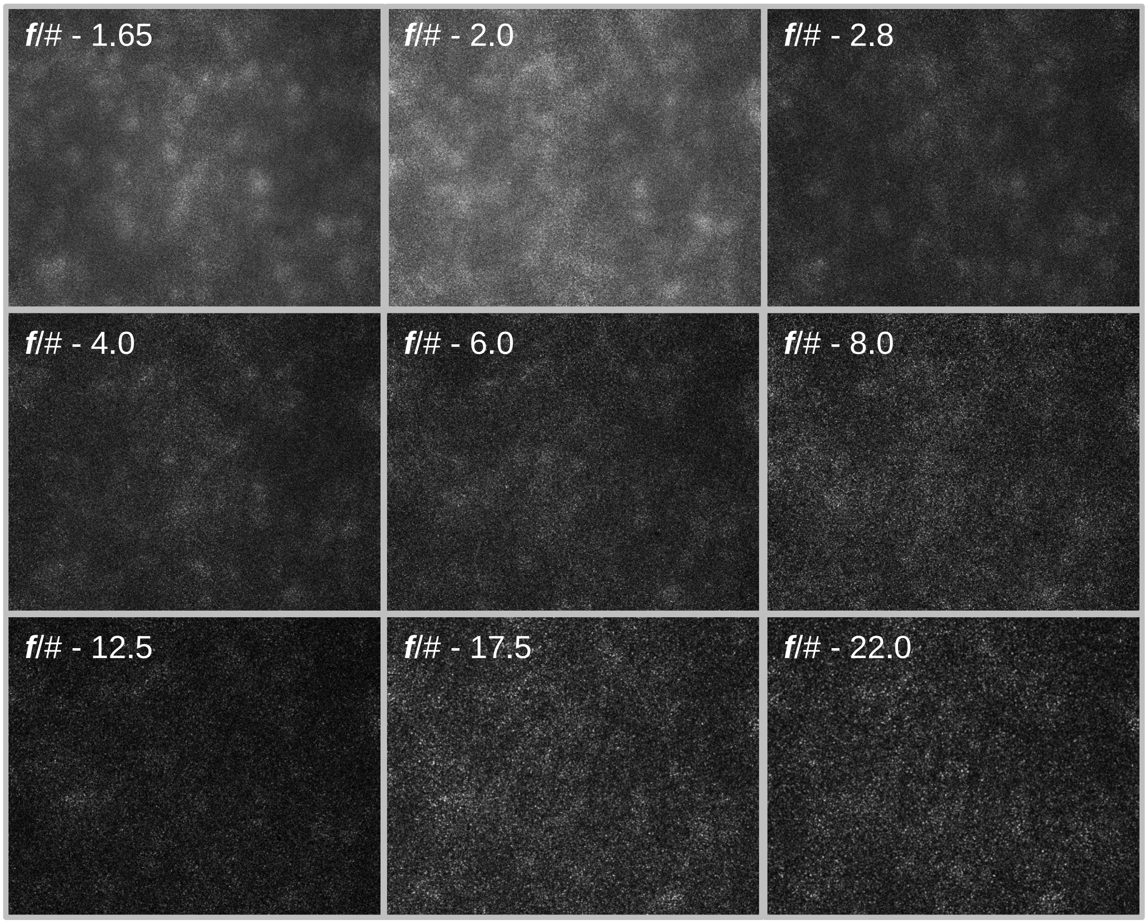

**FIGURE 4-9 SPECKLE SIZE INCREASING AS THE F/# OF THE APERTURE IS DECREASED FROM 22 - 1.65 IN 9 DISCRETE STEPS**

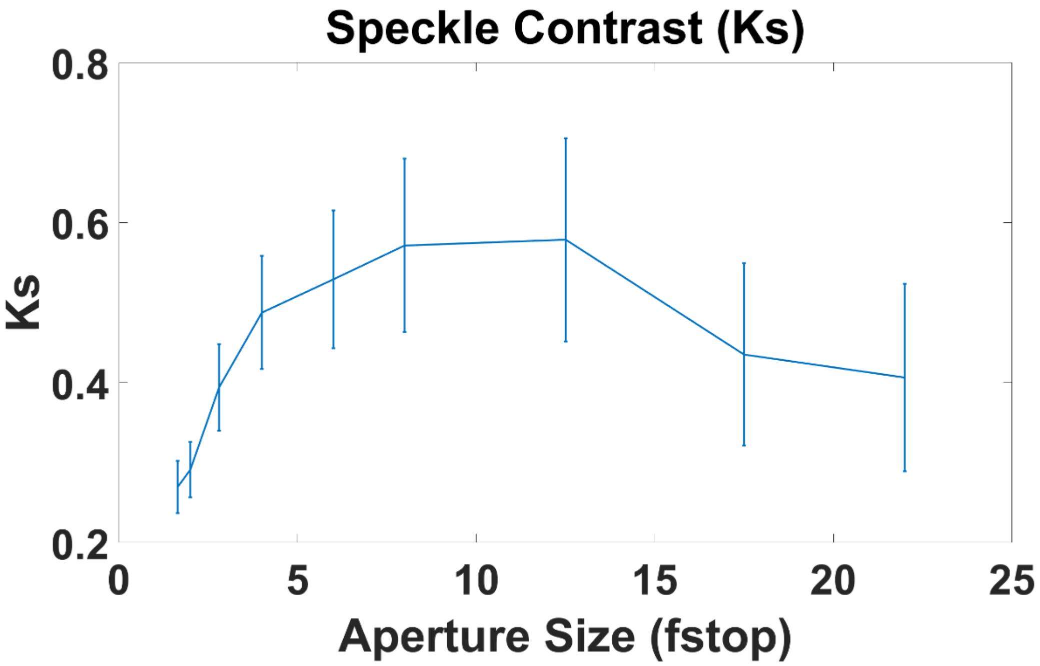

FIGURE 4-10 SPECKLE CONTRAST (KS) VS APERTURE SIZE CALIBRATION

Based on these results, the optimal aperture size for maximizing speckle contrast (Ks) was ***f/#*** = 17.5, which we maintained for the remainder of our experiments moving forward.

Once the speckle size was optimized, the next step was to validate the accuracy of the flow speed measurements. To do this, we constructed a phantom with a plastic tube running across an open well, shown below in Figure 4-11. The well is filled with a liquid tissue phantom with optical properties of $\mu_a$ = 0.01 $cm^{-1}$ and $\mu_s'$ = 1.0 $cm^{-1}$ to mimic human tissue. The tube was then connected to a syringe pump, where the same liquid tissue phantom was pumped through the tube at a series of set flow speeds.

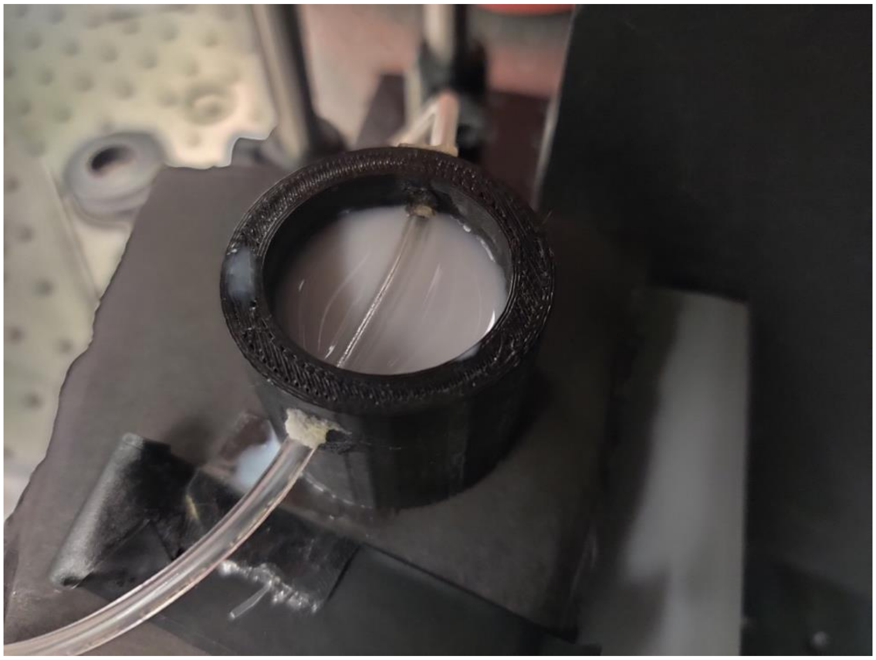

FIGURE 4-11 FLOW PHANTOM

The effect of moving scatterers on speckle contrast can be observed in the raw speckle images, shown below in Figure 4-12 and the inverse speckle contrast (Kt) images in Figure 4-13. The speckle image collected while the tube phantom was not flowing, left, shows a clear speckle pattern on the tube similar to that of the background liquid. The speckle image of the flowing tissue phantom, on the right, shows a distinctly blurred speckle pattern on the tube. We quantified the relative blood flow over the flow speed range of 1.0 – 5.0 mm/sec to mimic the expected flow speeds in mouse skeletal muscles(Ivanov et al., 1981)(Ivanov et al., 1981)(Ivanov et al., 1981)(Ivanov et al., 1981)(Ivanov et al., 1981)(Ivanov et al., 1981)(Ivanov et al., 1981)(Ivanov et al., 1981). We observed that the inverse speckle contrast shows a linear response ($R^2 = 0.979$) over the 1.0 – 5.0 mm/sec flow speeds, shown below in Figure 4-14.

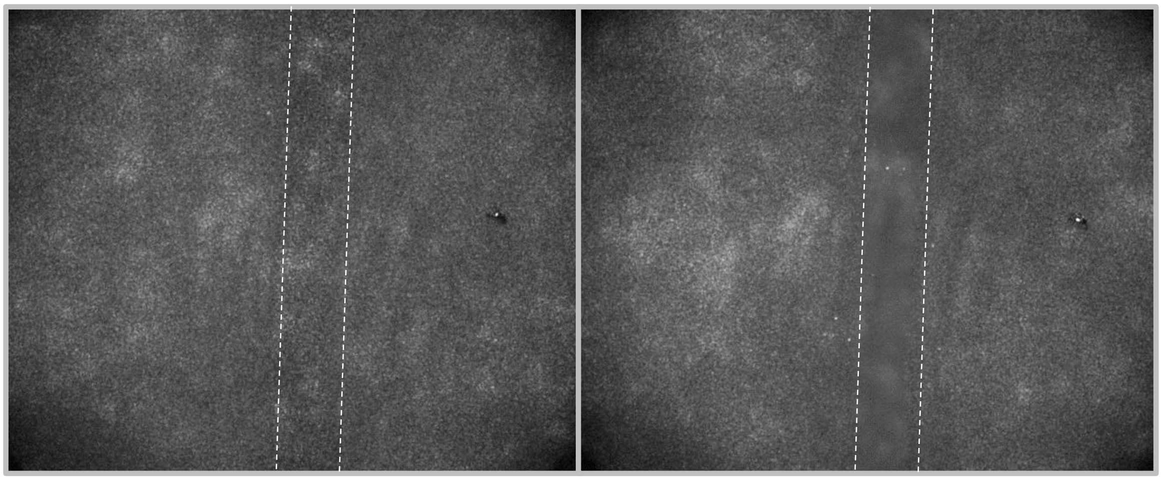

FIGURE 4-12 SPECKLE IMAGE COMPARISON. THE TUBE (WHITE OUTLINE) IS NOT VISIBLE IN THE IMAGE WITH NO FLOW, LEFT, WHILE THE TUBE REGION IS CLEARLY BLURRED IN THE IMAGE WHERE THE TUBE PHANTOM IS FLOWING AT 5.0 MM/SEC, RIGHT.

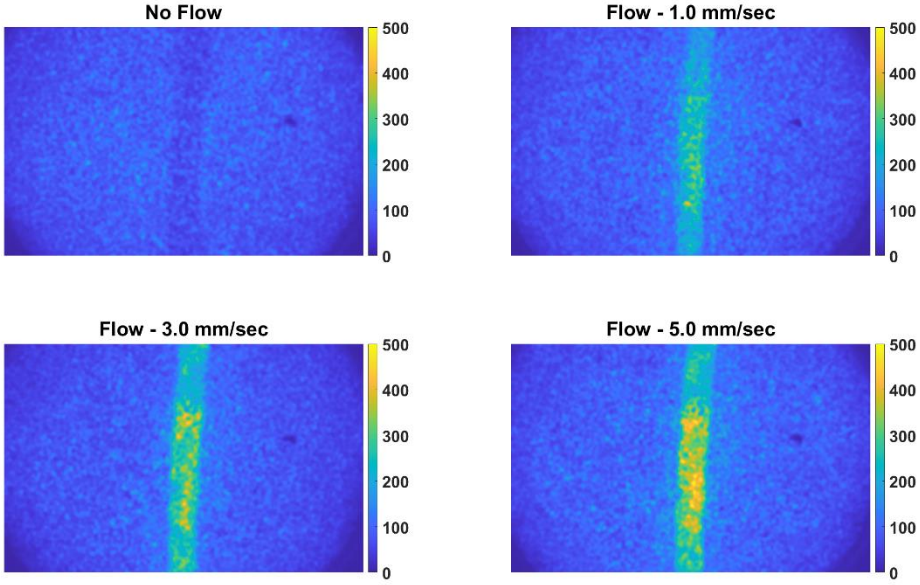

FIGURE 4-13 INVERSE SPECKLE CONTRAST IMAGES OF VARYING FLOW SPEEDS FROM ZERO (NO FLOW) TO A MAXIMUM OF 5.0 MM/SEC. THE COLORBAR REPRESENTS THE INVERSE SPECKLE CONTRAST.

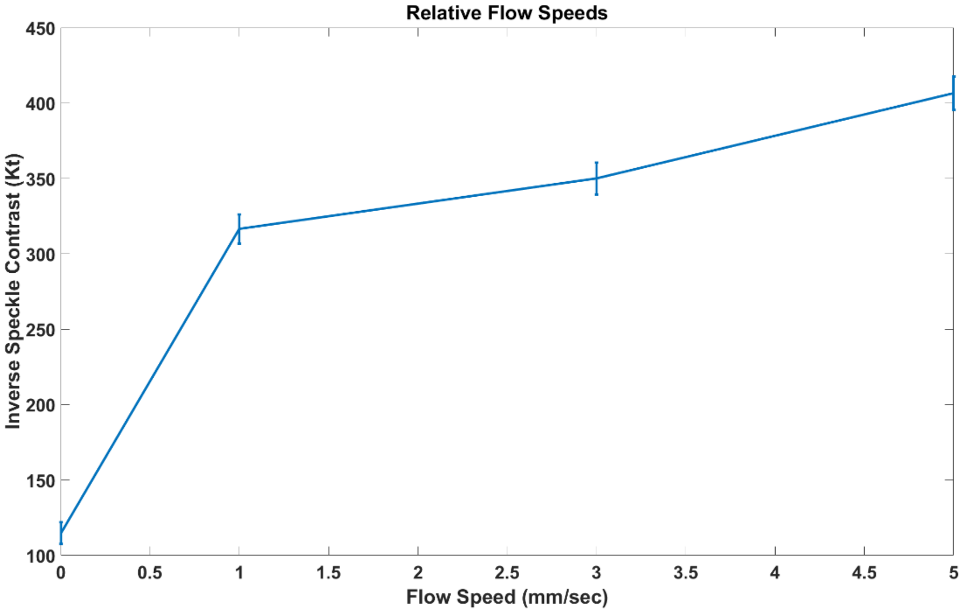

**FIGURE 4-14 RELATIVE INVERSE CONTRAST MEASUREMENTS IN A REGION OF INTEREST FOCUSED ON THE FLOW TUBE PHANTOM DURING VARIABLE FLOW SPEEDS**

After calibrating the speckle size of the system and validating the linearity of the measurements in the expected flow speed range, the system is tested in vivo. For his, we required a physiological perturbation which results in a large change in relative blood flow. Arterial cuff ischemia followed by post occlusive reactive hyperemia is a commonly studied procedure that produces large changes in arterial blood flow(M et al., 2004; O'Doherty et al., 2009)(M et al., 2004; O'Doherty et al., 2009)(M et al., 2004; O'Doherty et al., 2009)(M et al., 2004; O'Doherty et al., 2009)(M et al., 2004; O'Doherty et al., 2009)(M et al., 2004; O'Doherty et al., 2009)(M et al., 2004; O'Doherty et al., 2009)(M et al., 2004; O'Doherty et al., 2009). First, we aligned the right, dominant, hand of the subject under the LSCI system in a flat, pronated position. A sphygmomanometer was fitted around the bicep of the subject. A non-contact DCS system was also used to perform simultaneous blood flow measurements to serve as a validated comparison to the LSCI system. Initially, we recorded baseline blood flow measurements with the subject at rest for 1 minute. Then, the sphygmomanometer was inflated to 220 mmHg of pressure to completely arrest venous and arterial circulation for a duration of 1 minute. Finally, the pressure on the sphygmomanometer was released and 1 minute of post-occlusive reactive hyperemia was recorded, with a total measurement time of 3 minutes. Representative inverse speckle (kappa) maps during the four experimental phases (baseline, ischemia, post occlusion reactive hyperemia, recovery) are shown below in Figure 4-15 and the longitudinal flow measurements for LSCI and noncontact DCS are shown in Figure 4-16 and normalized in Figure 4-17.

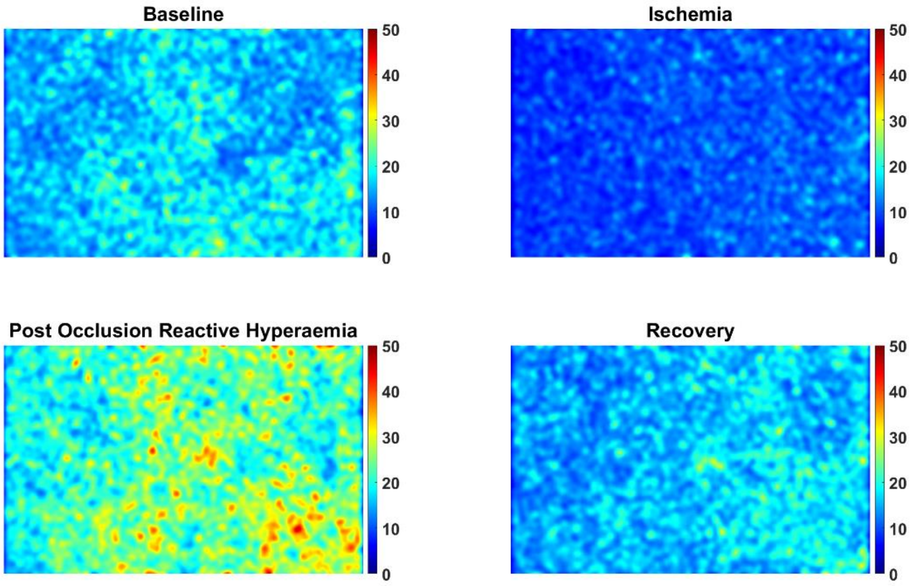

FIGURE 4-15 INVERSE SPECKLE CONTRAST IMAGES (KT) DURING THE FOUR EXPERIMENTAL PHASES OF ARTERIAL OCCLUSION THROUGH COMPRESSION OF THE SPHYGMOMANOMETER

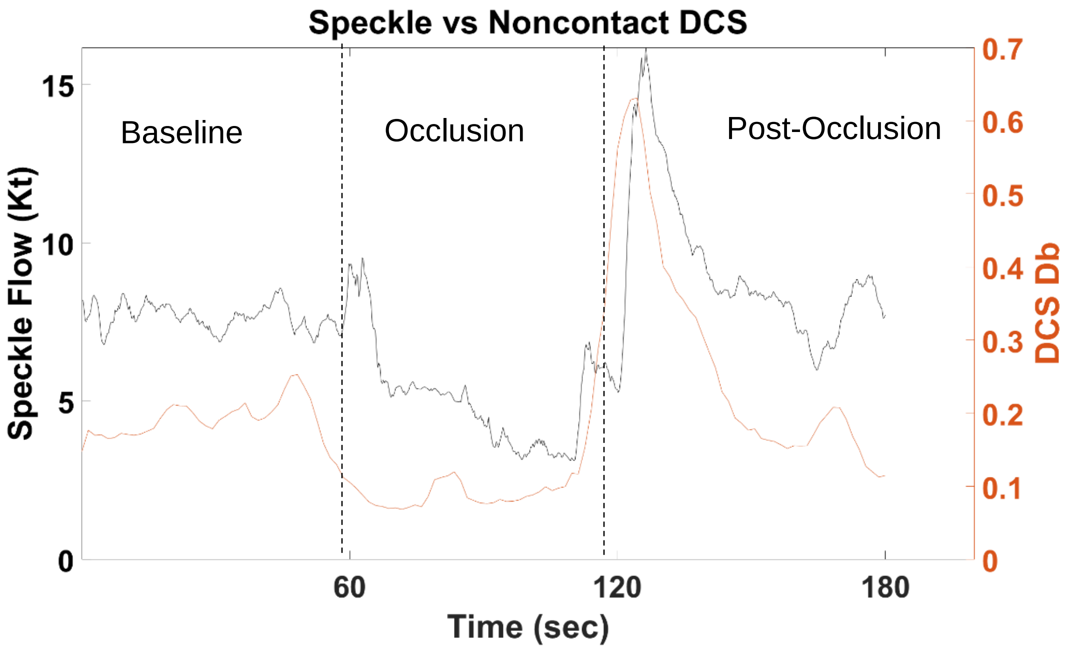

FIGURE 4-16 COMPARISON BETWEEN SPECKLE FLOW MEASUREMENTS (INVERSE SPECKLE CONTRAST, KT, BLUE LINE) AND DCS FLOW MEASUREMENTS (BROWNIAN DIFFUSION COEFFICIENT, DB, ORANGE LINE) DURING ARTERIAL ISCHEMIA EXPERIMENT

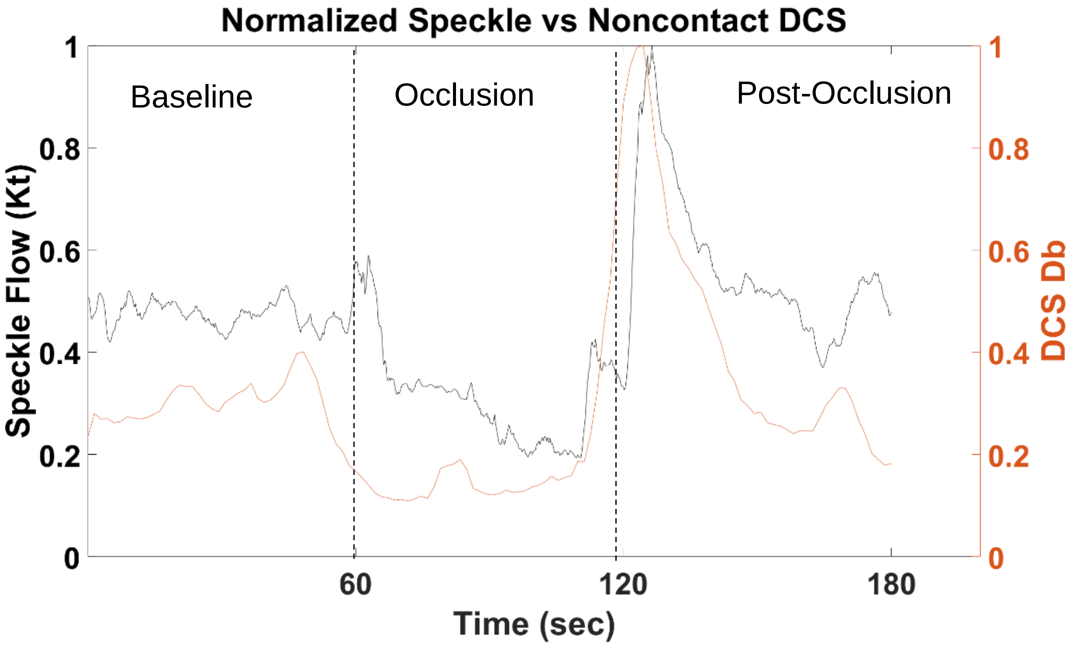

FIGURE 4-17 NORMALIZED COMPARISON BETWEEN SPECKLE FLOW MEASUREMENTS (INVERSE SPECKLE CONTRAST, KT, BLUE LINE) AND DCS FLOW MEASUREMENTS (BROWNIAN DIFFUSION COEFFICIENT, DB, ORANGE LINE) DURING ARTERIAL ISCHEMIA EXPERIMENT

The results of the ischemia procedure show similar trends in the LSCI and DCS results. The LSCI measurement showed a 22.16% decrease from the baseline phase to the occlusion phase. The DCS measurements showed a decrease in $D_b$ of 55.4% during occlusion (0.19 +/- 0.0046 to 0.0881 +/- 0.016) and the LSCI measurements showed a decrease in Kt of 31.93% during occlusion (7.67 +/- 0.0268 to 5.22 +/- 0.0992). A Wilcoxon Rank Sum analysis was performed between the baseline and ischemia data for the DCS and LSCI data. The measured blood flow in both DCS and LSCI was significantly lower ($p \ll 0.001$) for both instruments. Box plots illustrating the summary statistics are shown below for DCS in Figure 4-18 and LSCI in Figure 4-19.

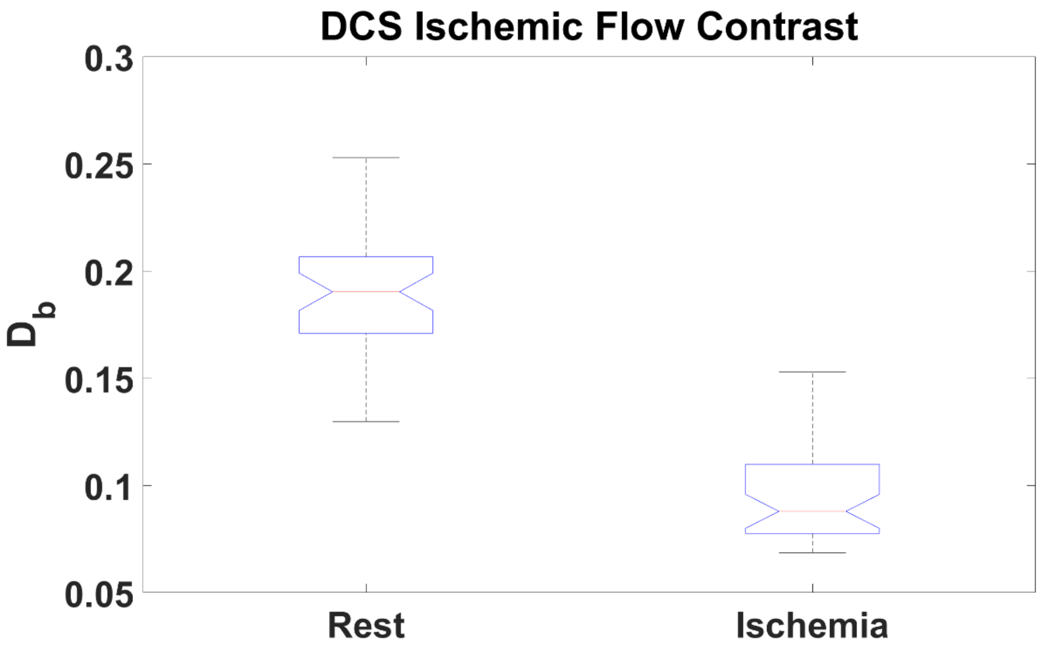

FIGURE 4-18 FLOW SPEED DECREASE FROM REST TO OCCLUSION MEASURED BY THE NON-CONTACT DCS SYSTEM

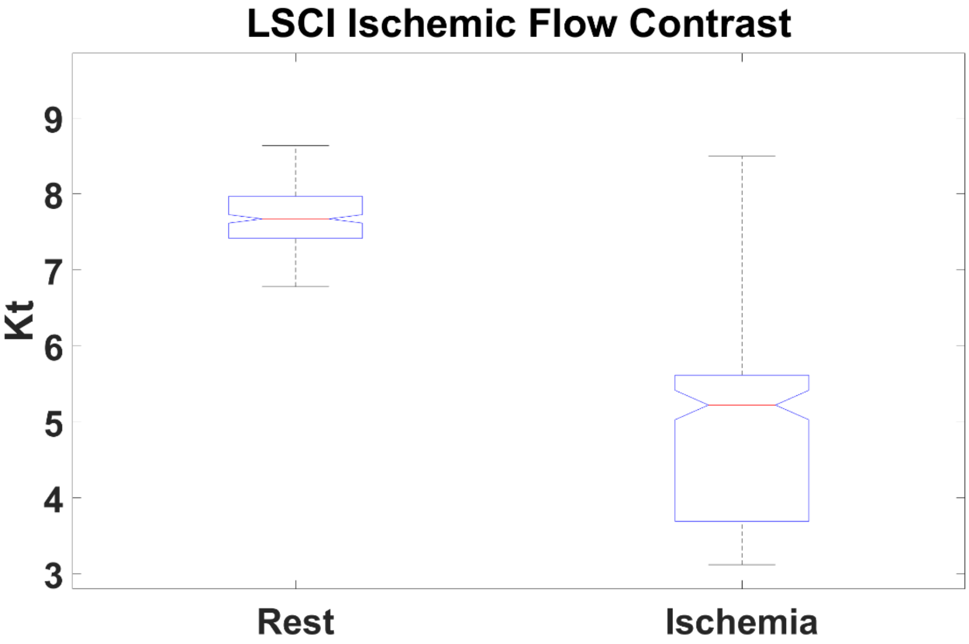

FIGURE 4-19 FLOW SPEED DECREASE FROM REST TO OCCLUSION MEASURED BY THE LSCI SYSTEM

Both blood flow measurement systems showed large increases in blood flow during the post-occlusive reactive hyperemia phase as the pressure was released from the sphygmomanometer. The DCS measurements reached a maximum of 0.6311 a.u. which is an increase of 231.68% from the median baseline value and an increase of 616.65% from the median occluded value. Comparatively, the DCS measurements reached a maximum of 16.17 a.u. which is an increase of 110.78% from the median baseline value and an increase of 209.64% from the median occluded value.

## 4.3 In-vivo Stimulated Skeletal Muscle Imaging

After the LSCI + SFDI system was calibrated and validated in vivo, continuous blood flow (LSCI) and optical property (SFDI) measurements in mice were performed during electrically stimulated skeletal muscle contractions. This non-contact imaging approach solved the challenge of performing measurements during muscle contractions, as detailed in Section 3.2, with the added benefit of two-dimensional blood flow and optical property maps being generated so that one can investigate blood flow heterogeneity or localization during the contractions.

### 4.3.1 Methods

Two adult wild type (WT) mice (C57BL/6J) were imaged under the non-contact LSCI + SFDI system. The first, called WT1, was prepared in a similar manner to our previous study in section 3.2. The plantar flexor muscles and the sciatic nerve were exposed by resecting the surrounding skin and the leg was stabilized to restrict movement. Nerve-evoked contractions were stimulated with platinum electrodes resting on the sciatic nerve, as shown below in Figure 4-20.

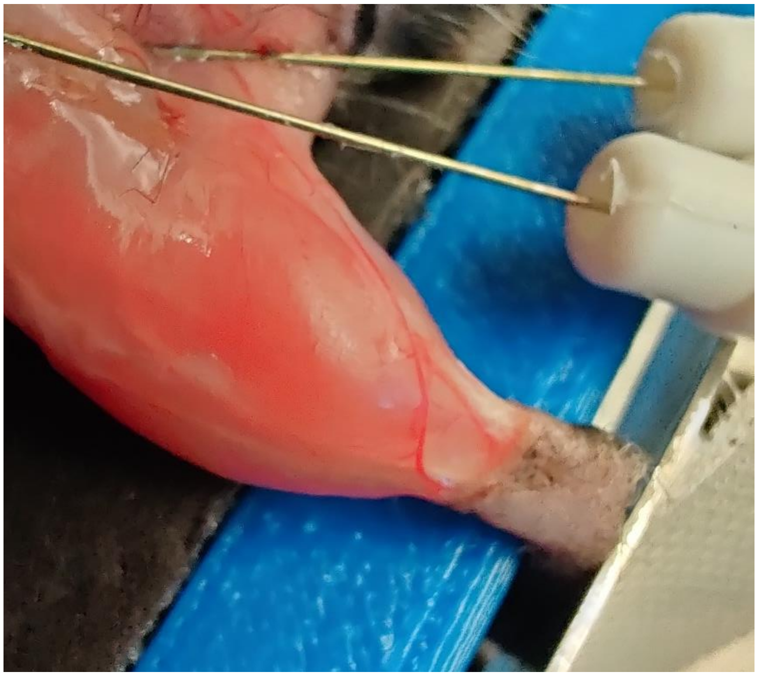

FIGURE 4-20 ELECTRODE PLACEMENT AND LOWER LIMB MUSCLE SHOWN WITH TISSUE RESECTED IN WT1

The stimulus amplitude and the pulse width was ≤5 V at 1 ms were delivered with platinum electrodes supplied by a function / arbitrary waveform generator (Rigol DG4162). A 10x5 repeated tetani stimulation protocol was administered as previously described in section 3.2. The second mouse, WT2, was imaged noninvasively with intact skin. Platinum electrodes were implanted on the left and right of the sciatic notch. Electrical stimulation was delivered in a 10x5 repeated tetani protocol, the same as WT1. LSCI was performed for a 1-minute baseline period, 10*5 repeated tetani, and a 5-minute recovery period for a total measurement time of 18 minutes. SFDI was performed at two distinct time points; once during the baseline period and a second time immediately following the 10x5 repeated tetani protocol.

For post-processing a region of interest was manually defined to avoid large blood vessels that showed much higher blood flow, such as the saphenous nerve, and focus the analysis on perfusion of the microvasculature to the muscle fibers. The definition of the region of interest (black dotted) for WT1 and WT2 is shown below in Figure 4-21.

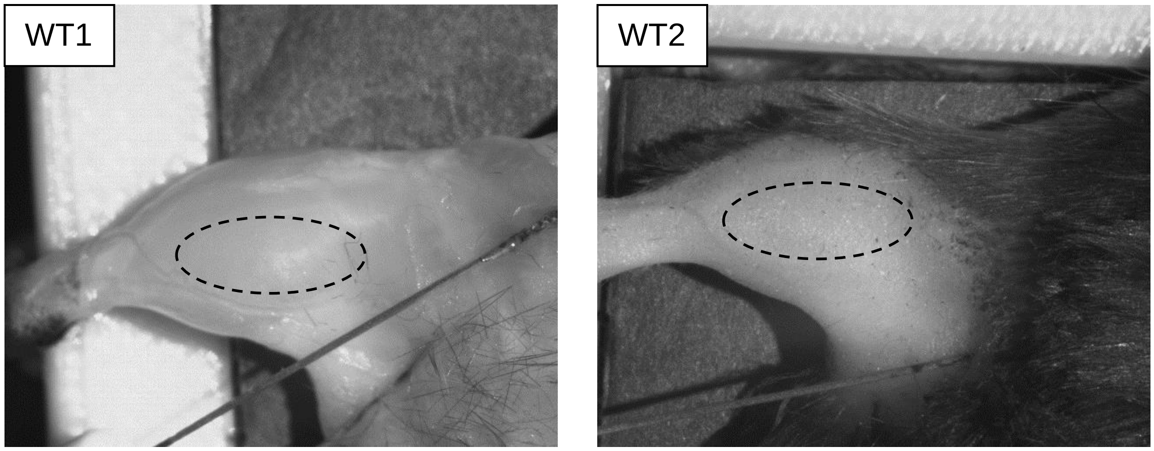

FIGURE 4-21 WT1 AND WT2 SHOWN WITH WHITE LIGHT ILLUMINATION UNDER CAMERA FOV. BLACK DOTTED OVALS DENOTE REGION OF INTEREST FOR LSCI ANALYSIS

### 4.2.3 Results - LSCI

Representative Kt images for WT1 (Figure 4-22) and WT2 (Figure 4-23) are shown below. There were 11 points in time chosen corresponding to baseline and the maximum and minimum blood flow measurements during each of the five post-contraction recovery periods. The entire lower leg is shown in these images to give a full representation of the spatial resolution capabilities of the LSCI technique. The order of images from 1 – 11 for each mouse is as follows: **1 –** baseline, **2 –** maximum blood flow following tetani #1, **3 –** minimum blood flow after recovery from tetani #1, **4 –** maximum blood flow following tetani #2, **5 –** minimum blood flow after recovery from tetani #2, **6 –** maximum blood flow following tetani #3, **7 –** minimum blood flow after recovery from tetani #3, **8 –** maximum blood flow following tetani #4, **9 –** minimum blood flow after recovery from tetani #4, **10 –** maximum blood flow following tetani #5, **11 –** minimum blood flow after recovery from tetani #5.

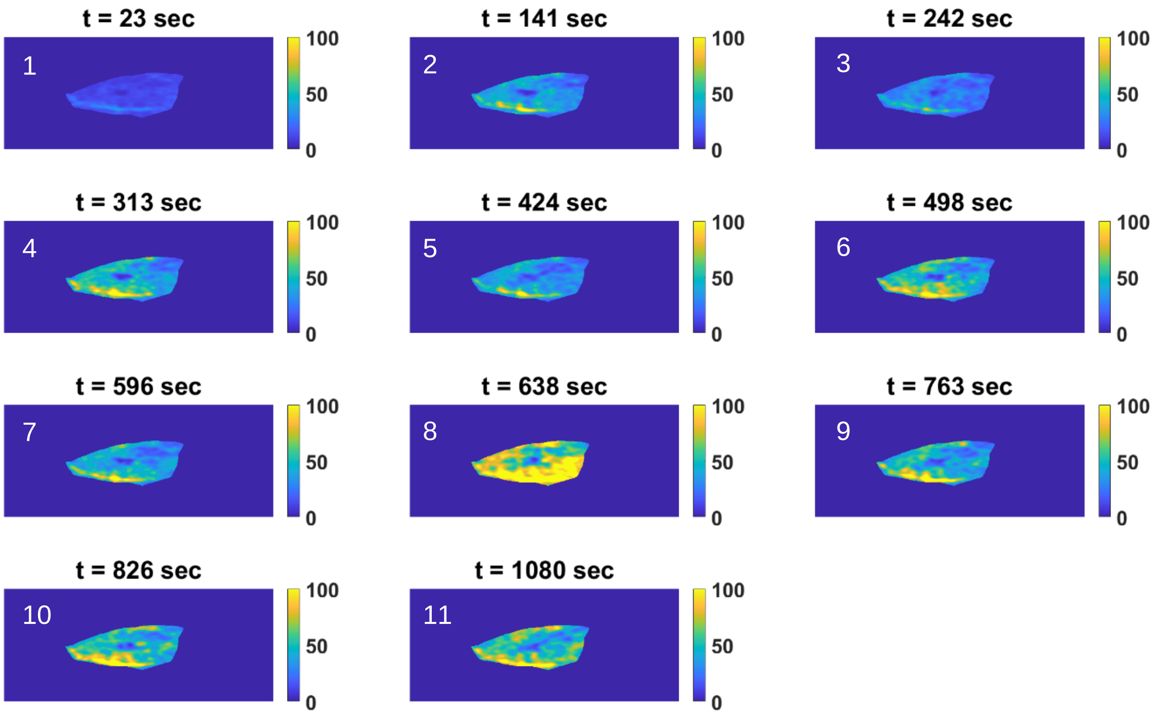

FIGURE 4-22 WT1 - INVERSE SPECKLE IMAGES MAPPING RELATIVE FLOW SPEED DURING 10X5 TETANIC CONTRACTION PROTOCOL

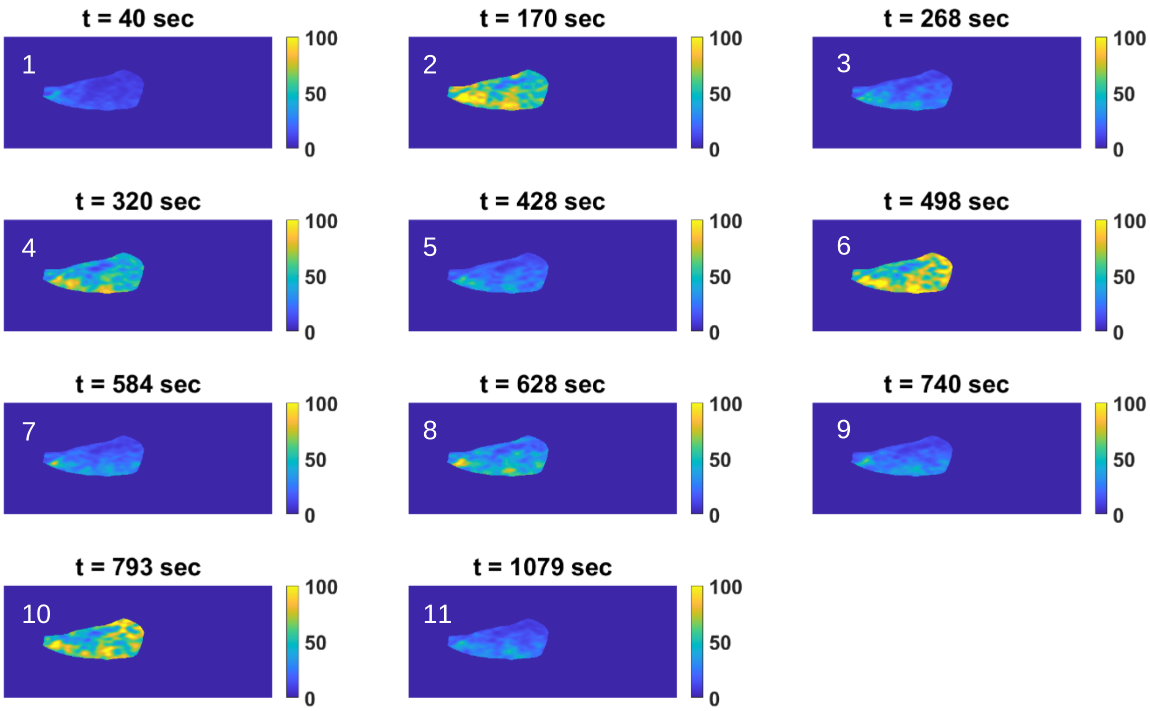

FIGURE 4-23 WT2 - INVERSE SPECKLE IMAGES MAPPING RELATIVE FLOW SPEED DURING 10X5 TETANIC CONTRACTION PROTOCOL

To make a quantitative comparison on the inverse speckle contrast blood flow imaging capability in the exposed muscle, WT1, versus the noninvasive model, WT2, we calculated the mean speckle contrast within the region of interest located immediately medial to the saphenous artery and centralized in the gastrocnemius muscle. The mean inverse speckle contrast for WT1 is shown below in Figure 4-24 and for WT2 in Figure 4-25. The top and bottom plots both contain the inverse speckle contrast, where the bottom plots in each figure have the speckle contrast axis truncated to better visualize the blood flow trends following the recovery periods post-contraction. The large spikes that are seen in the inverse speckle contrast data are motion artefact from the tetanic contractions. We have observed that LSCI was also sensitive to large mechanical motion artefact as well, which was to be expected.

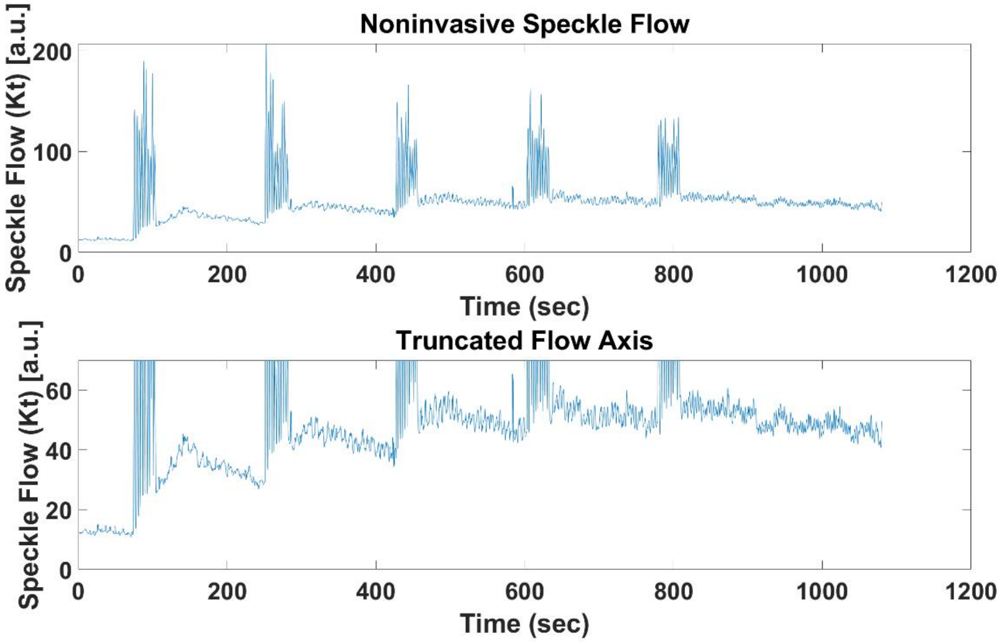

**FIGURE 4-24 MOUSE WT1 - MEAN INVERSE SPECKLE CONTRAST (KT) TRACES INSIDE OF ROI SHOWN IN FIGURE 26. THE TOP AND BOTTOM PLOTS CONTAIN THE SAME DATA, WITH THE BOTTOM PLOT BEING TRUNCATED TO SHOWCASE THE KT TRENDS DURING THE POST-CONTRACTION RECOVERY PERIODS.**

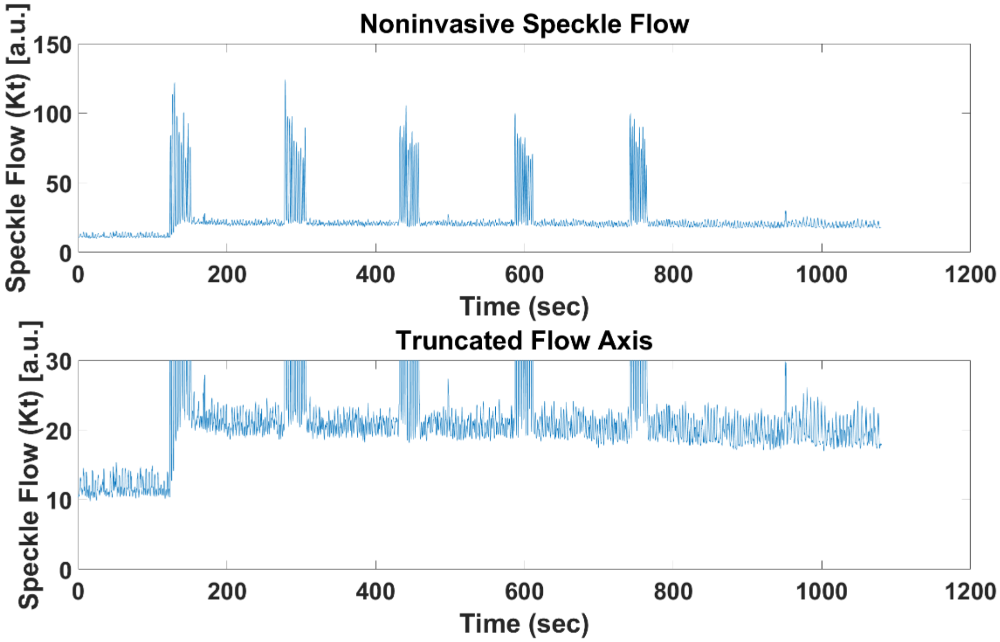

FIGURE 4-25 MOUSE WT2 - MEAN INVERSE SPECKLE CONTRAST (KT) TRACES INSIDE OF ROI SHOWN IN FIGURE 26. THE TOP AND BOTTOM PLOTS CONTAIN THE SAME DATA, WITH THE BOTTOM PLOT BEING TRUNCATED TO SHOWCASE THE KT TRENDS DURING THE POST-CONTRACTION RECOVERY PERIODS.

The exposed muscle measurements in WT1 showed a maximum increase in mean inverse speckle contrast from baseline, 12.31 +/- 0.091, to the fifth tetani post-contraction hyperemia period, 53.61 +/- 0.27 of 335%. The non-invasive muscle measurements of WT2 showed a maximum increase in mean inverse speckle contrast from baseline, 10.84 +/- 0.19, to the fifth tetani post-contraction hyperemia period, 18.84 +/- 0.20 of 73.8%. The blood flow measurements from baseline to the fifth post-contraction hyperemia period showed a statistically significant increase in both WT1 ($p >> 0.001$) and WT2 ($p >> 0.001$). The measurements in both cases are encouraging. The much higher blood flow increase shown in WT1 is expected due to the resection of the skin. The resulting images are higher contrast and the speckles are interacting directly with the muscle instead of diffusing through the skin. The increase observed in WT2 was lower; however, the observed increase of 73.8% was comparable to the percent increase shown in the wild-type group in the contact DCS experiments in Chapter 3.2.2, Figure 3-7 of 130%. Therefore, the LSCI camera-based post-contraction hyperemia imaging has been validated in both a skin resected (WT1) and non-invasive (WT2) model.

### 4.2.4 Results – SFDI

Spatial frequency domain imaging was performed on WT1 before and after a muscular contraction to validate the SFDI system in vivo. Blood oxygenation kinetics during and after skeletal muscle contractions have been extensively tested extensively(B et al., 2003; BJ et al., 2008; Ferguson et al., 2018; Ferrari et al., 1997; Pollonini, 2018; RA et al., 1994). During muscle contraction, oxygen metabolism in the muscle will increase, causing a decrease in oxygenated hemoglobin concentration (HbO) and an increase in deoxygenated hemoglobin concentration (Hb). At the conclusion of muscular contraction a hyperemia reaction will cause an influx of blood volume into the exercised tissue during a recovery period. During this time, the HbO and total hemoglobin concentration (HbT = HbO + Hb) should increase. First, the SFDI maps for absorption, Figure 4-26, and scattering, Figure 4-27, coefficients before and after muscular concentrations at the three wavelengths probed by the system (660, 730, 850 nm) are shown at ROI positions similar to those of the LSCI results in Chapter 4.2.3.

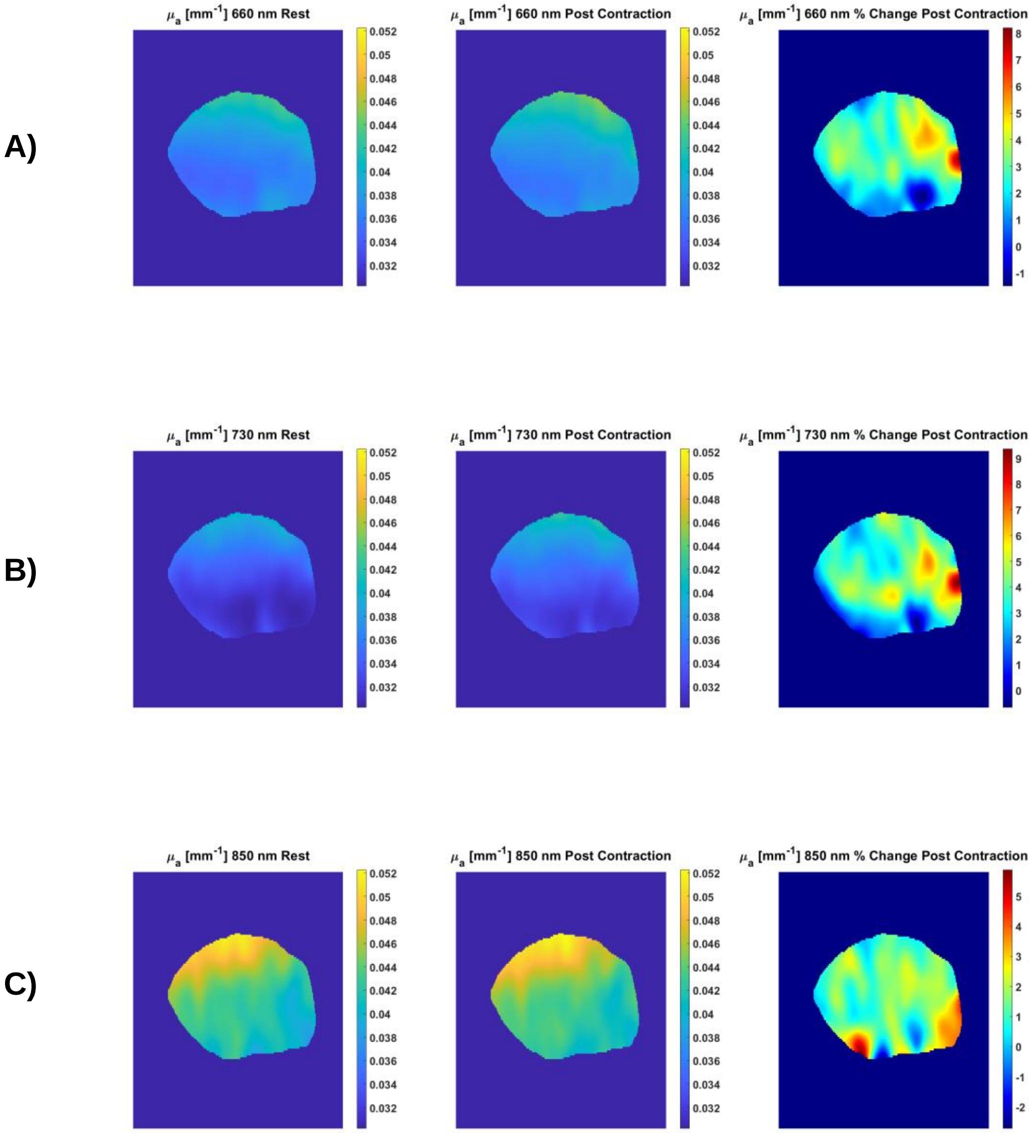

**FIGURE 4-26 ABSORPTION COEFFICIENT MAPS [MM-1] FOR A) 660 NM, B) 730 NM, C) 850 NM. FROM LEFT TO RIGHT: REST, POST-CONTRACTION AND PERCENT CHANGE FROM REST TO POST CONTRACTION IS SHOWN.**

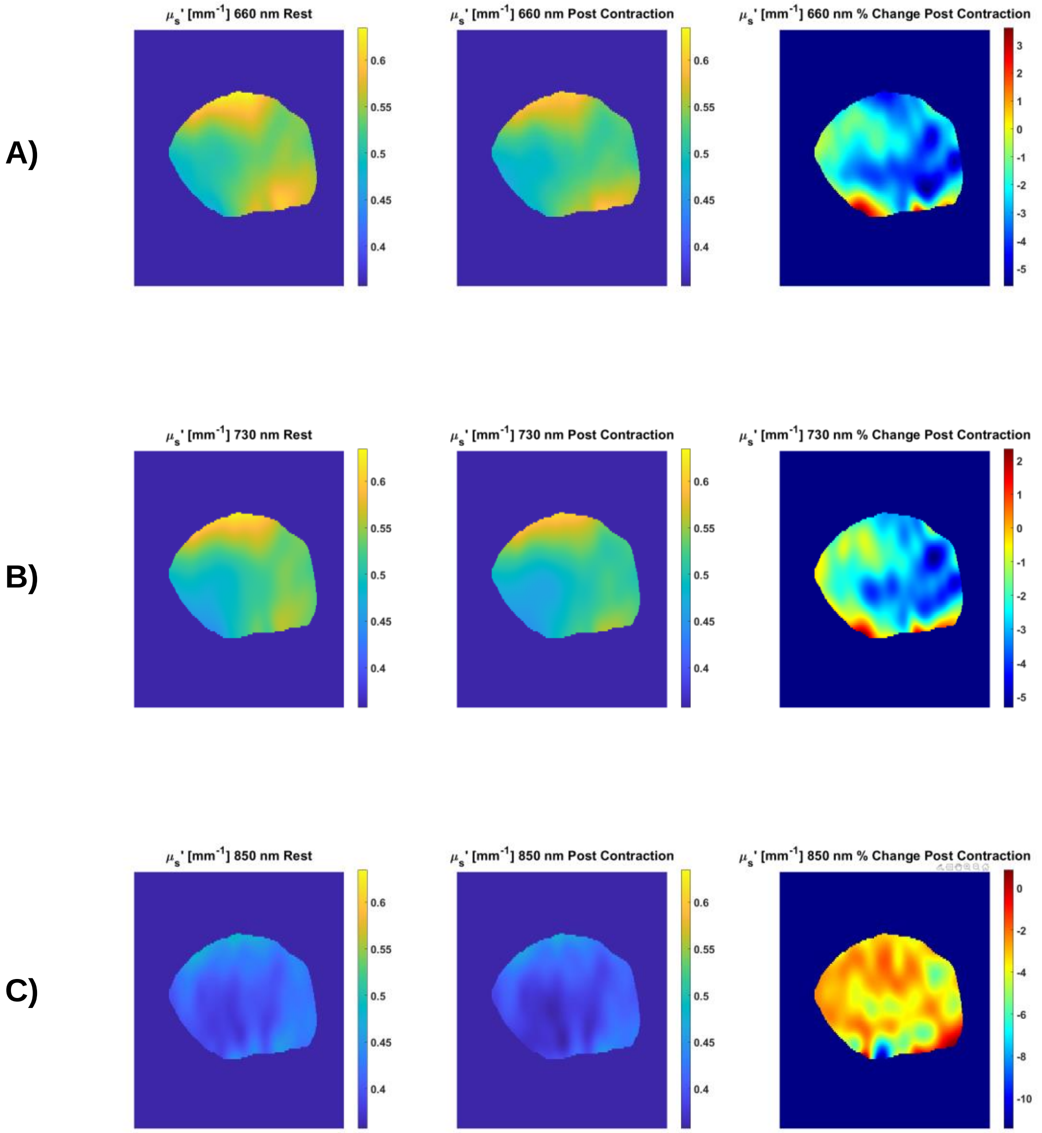

**FIGURE 4-27 SCATTERING COEFFICIENT MAPS [MM-1] FOR A) 660 NM, B) 730 NM, C) 850 NM. FROM LEFT TO RIGHT: REST, POST-CONTRACTION AND PERCENT CHANGE FROM REST TO POST CONTRACTION IS SHOWN.**

To quantify the results, the mean percent change from rest to post-contraction was calculated for each of the plots above. The post-contraction absorption coefficient maps showed mean percent changes of 2.69 +/- 0.0096 at 660 nm, 3.70 +/- 0.0105 at 730 nm, and 1.54 +/- 0.0072 at 850 nm. The post-contraction absorption coefficient maps showed mean percent changes of -2.53 +/- 0.00031 at 660 nm, -2.41 +/- 0.0089 at 730 nm and -3.37 +/- 0.0091 ta 850 nm. An increase in the absorption coefficient is expected during the post-contraction phase. The hyperemia reaction causes vasodilation and increased blood flow, as shown in the LSCI results. Therefore, total blood volume increases, which is reflected in an increased absorption coefficient. In theory, the measurements of the scattering coefficient should also increase during hyperemia. Possible explanations could include a decrease in relative tissue density during the vasodilation phase of hyperemia or a crosstalk between the absorption and scattering coefficient solutions, which has previously been reported previously(LF et al., 2007).

The multiwavelength absorption coefficient results were also used to calculate HbO and Hb by way of the Modified Beer Lambert Law:

$$\mu_a(\lambda_1) = 2.303 * \varepsilon_{oxy}(\lambda_1) * HbO + 2.303 * \varepsilon_{deoxy}(\lambda_1) * Hb$$

$$\mu_a(\lambda_2) = 2.303 * \varepsilon_{oxy}(\lambda_2) * HbO + 2.303 * \varepsilon_{deoxy}(\lambda_2) * Hb$$

Where, $\mu_a$ = absorption coefficient, $\lambda$ = source wavelength, $\varepsilon_{oxy}$ and $\varepsilon_{deoxy}$ are the molecular extinction coefficients for oxygenated and deoxygenated hemoglobin, respectively. The extinction coefficients were sourced from Wray et al(S et al., 1988). Wavelengths 1 and 2 were chosen to be 730 nm and 850 nm because of the much higher extinction coefficient for deoxygenated hemoglobin at 660 nm, which would weight the error statistics of the system towards 660 nm. The hemoglobin results are shown below in Figure 4-28. Also shown in this figure are the tissue oxygen saturation (StO2) which is defined as: $StO2 = (HbO/HbT) * 100$

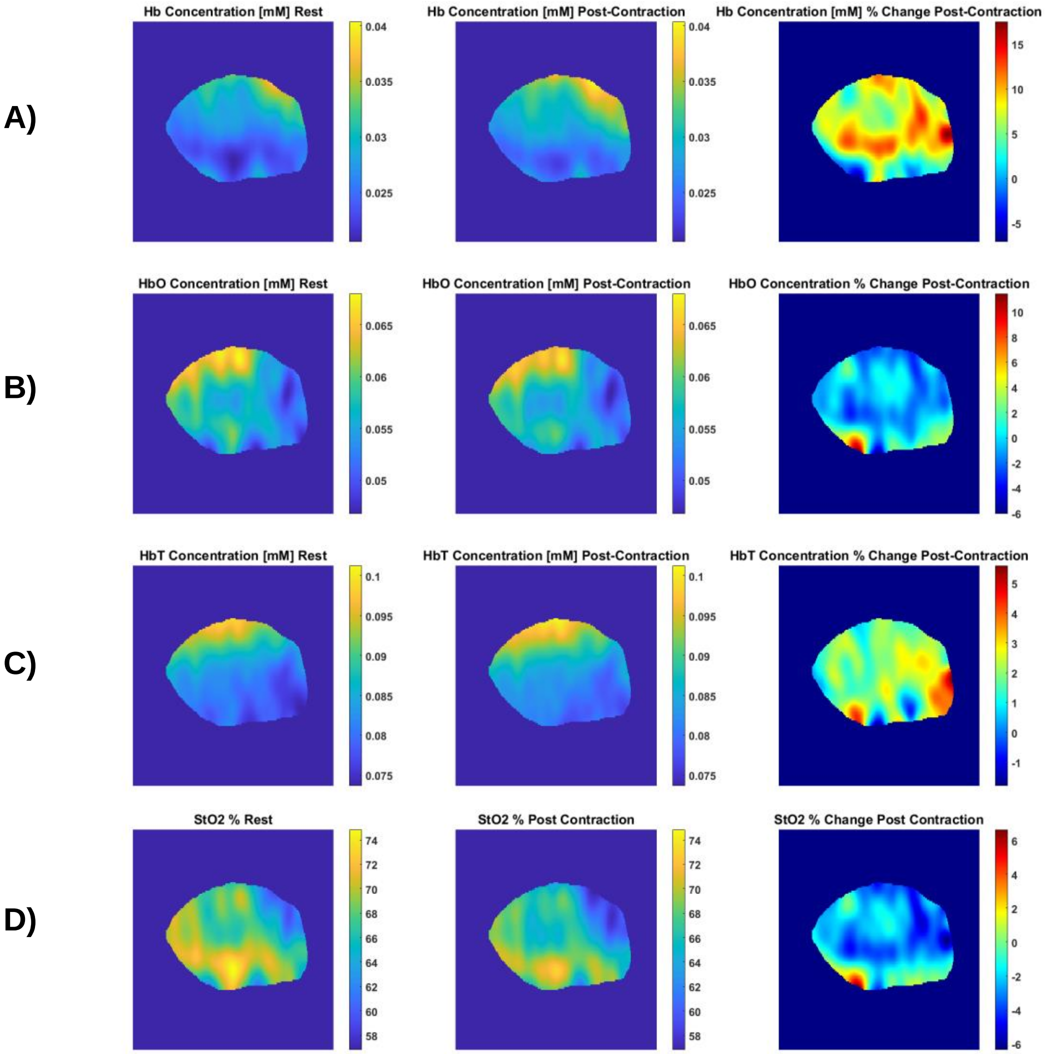

**FIGURE 4-28 HEMOGLOBIN AND STO2 MAPS FOR A) HB, B) HBO, C) HBT, D) STO2. LEFT TO RIGHT: REST, POST-CONTRACTION, PERCENT CHANGE POST CONTRACTION**

Quantification of the hemoglobin results gave us an insight into post-contraction recovery and oxygenation. The post concentration maps showed percent changes of 7.09 +/- 0.025 for Hb, -0.35 +/- 0.014 for HbO, 2.039 +/- 0.0067 for HbT and -2.34 +/- 0.012 for StO2. The decrease in HbO increase in Hb post-contraction was an expected result resulting from oxygen consumption in muscle tissue during tetanic contractions. We see that HbT has increase, which occurs as the hyperemia effect of muscular contractions has begun. For spatial distribution, we observed that the bottom sections of the image showed an opposite effect where HbO and HbT increase, while Hb decreases. These sections of the ROI covered muscle tissue directly next to the saphenous artery, which delivers oxygenated blood to the tissue. Therefore, the muscle tissue imaged here has been further reoxygenated.

StO2 results both before and after contraction are in the expected range of 65-75%(Y et al., 2015) . The StO2 results, expectedly, show the same trend as the hemoglobin results. The lower edge of the map has increased in oxygenation from hyperemia, while the remainder of the ROI, which is focused on the belly of the gastrocnemius muscle, shows a depleted oxygen saturation immediately post-contraction.

# 5. Human Grip Strength + DCS

The final stage of our research was aimed at translating the success of our Huntington's disease research in mice to the humans. The first step was to design and validate a protocol to measure blood flow in humans during a grip strength task. The decrease in grip force production capacity has been shown to be a marker of Huntington's disease progression. Simultaneous measurements of blood flow in the gripping muscles of the forearm allow an additional biomarker to further inform the clinician of myopathy and cardiovascular defects associated with disease progression.

## 5.1 Methods

DCS measurements will be recorded with the previously described DCS system with a custom probe made for forearm blood flow measurements with source-detector separations ranging from 1.5 to 3.0 cm, shown below in Figure 5-1. Fiber optic patch cables were used to transport light between the probe and the DCS system. From left to right; source fiber, 1.5 cm detector, 2.0 cm detector, 2.5 com detector, 3.0 detector. The source light was delivered with a 400-micrometer core optical fiber (Thorlabs, M99L01) and the reflected light was collected with 5 micrometer core, single-mode optical fibers (Thorlabs, P3-780Y-FC). Right-angle prisms were used to couple the fiber optic faces to the surface of the skin. This allowed fiber optics to run lengthwise along the arm of the patient, which decreased the tension on the tips and resulted in a low-profile design. A housing was 3D extrusion printed from polylactic acid (PLA) with ports precisely designed to fit the terminating ceramic ferrules of the optical fibers and the right-angle prisms. Loops were printed on both sides of the probe, where a nylon arm band was weaved through to provide an adjustable diameter to fit the subject’s forearm. This lightweight and low-profile design allowed blood flow measurements to be taken without inhibiting the patient from performing the grip strength task.

**FIGURE 5-1 DCS IMAGING PROBE USED TO MEASURE BLOOD FLOW DURING GRIP FORCE TASK. OPTICAL FIBERS ARE USED FOR LIGHT TRANSPORT. FROM LEFT TO RIGHT; SOURCE FIBER, 1.5 CM DETECTOR, 2.0 CM DETECTOR, 2.5 CM DETECTOR, 3.0 CM DETECTOR.**

The grip strength production of the subjects was measured with a grip strength dynamometer (ADInstruments, MLT004/ST) and recorded with

An experimental grip strength protocol with a difficult level capable of inducing muscle fatigue was devised in healthy subjects. To begin, the subject will be fitted with an amplified data acquisition system (Powerlab 26T). The subject was instructed to rest his arm on a table and hold the force dynamometer with his hand pronated. The DCS probe was then aligned over the carpi ulnaris flexor muscle, which was located asking the subject to perform a grip and release procedure while the researcher located the belly of the muscle by palpation. The final experimental setup is shown below in Figure 5-2.

FIGURE 5-2 SETUP POSITION OF AN EXAMPLE SUBJECT FOR THE GRIP STRENGTH AND BLOODFLOW MEASUREMENT EXPERIMENT. THE GRIP FORCE DYNAMOMETER IS GRIPPED IN THE RIGHT (DOMINANT) HAND, AND THE DCS PROBE IS POSITIONED ON THE FOREARM, SECURED BY A FLEXIBLE NYLON BAND.

The experimental timeline was executed as follows, with DCS blood flow measurements performed continuously at 785 nm, 1 Hz sampling rate: 1 minute of rest (allow for baseline blood flow measurement to be established, 5 seconds of maximum grip force, 1 minute rest, 1 minute of grip force at 30% of maximum followed by 30 seconds of rest (repeated three time), 1 minute of grip force at 60% of maximum followed by 30 seconds of rest (repeated three times, with the final rest period being extended to 2 minutes in length). The total measurement time was 14 minutes. During the experiment the subject was shown a live view of their grip strength measurements plotted over time via a computer monitor. During the 30% and 60% grip strength segments, a target line was also shown on the plot and the subjects were instructed to aim for the target line.

A total of 5 healthy control subjects (male, 18-50, dominant right hand dominant) were recruited for a feasibility study in which they performed the grip strength task while simultaneously collecting blood flow measurements with the DCS probe.

## 5.2 Results

The initial phase of the analysis was focused on assessing the signal viability of the various channels. As the separation between the source and detector increases, there is a potential for the signal coherence factor, β, to drop below an acceptable level (0.45 – 0.5). The coherence factor and associated blood flow traces are shown below for subjects 1-5 in Figures 5-3 thru 5-7. These coherence factor measurements show that the two longer distance channels (2.5 cm and 3.0 cm) were unstable, which also manifests itself in both unstable and dropped data points in the diffusion coefficient fits. This was most likely due to uncoherent light leakages from the room light, which is insignificant compared to measured coherent laser light source. As a result, only the 1.5 cm and 2.0 cm channels were considered for further analysis.

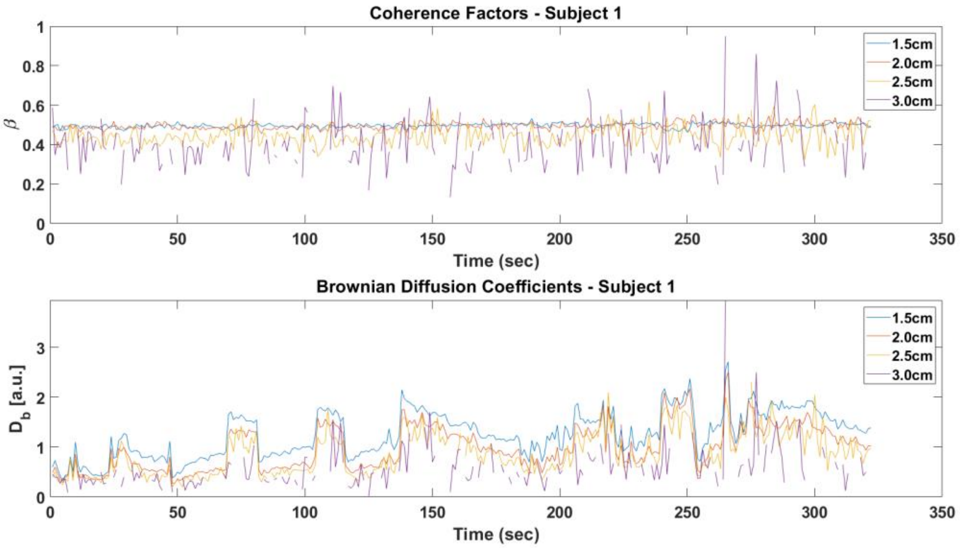

FIGURE 5-3 SUBJECT 1 - COHERENCE FACTOR MEASUREMENTS OVER TIME, TOP GRAPH, FOR EACH CHANNEL AND DIFFUSION COEFFICIENT, BOTTOM GRAPH, SHOWN FOR EACH ASSOCIATED CHANNEL

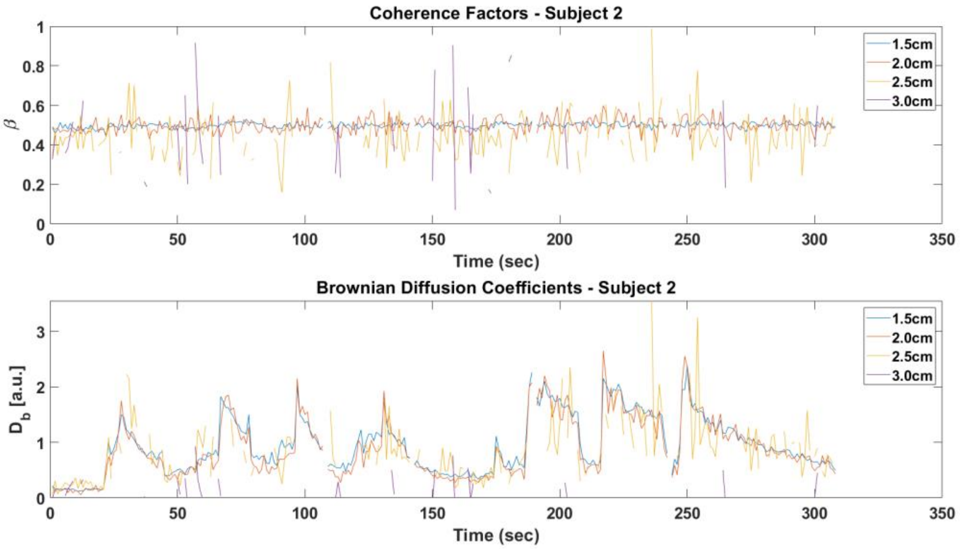

FIGURE 5-4 SUBJECT 2 - COHERENCE FACTOR MEASUREMENTS OVER TIME, TOP GRAPH, FOR EACH CHANNEL AND DIFFUSION COEFFICIENT, BOTTOM GRAPH, SHOWN FOR EACH ASSOCIATED CHANNEL

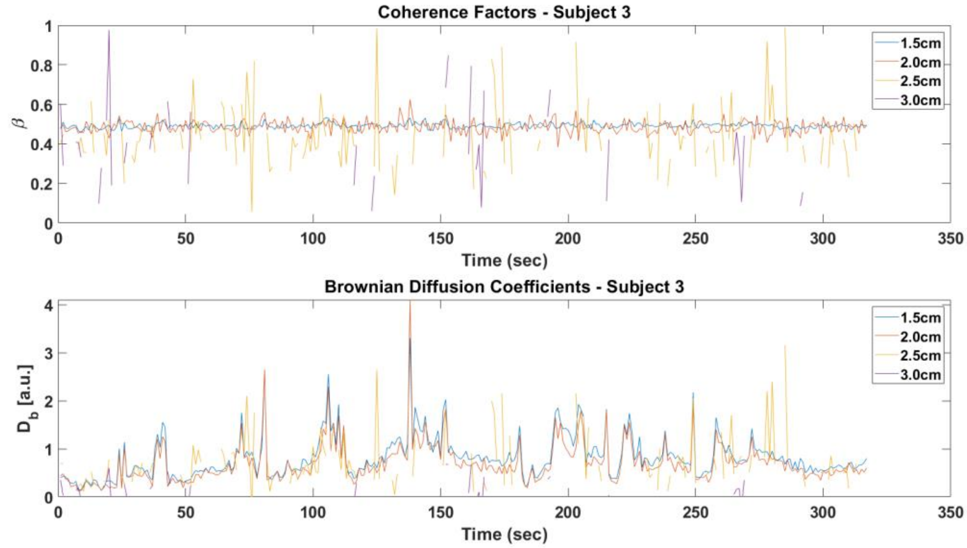

FIGURE 5-5 SUBJECT 3 - COHERENCE FACTOR MEASUREMENTS OVER TIME, TOP GRAPH, FOR EACH CHANNEL AND DIFFUSION COEFFICIENT, BOTTOM GRAPH, SHOWN FOR EACH ASSOCIATED CHANNEL

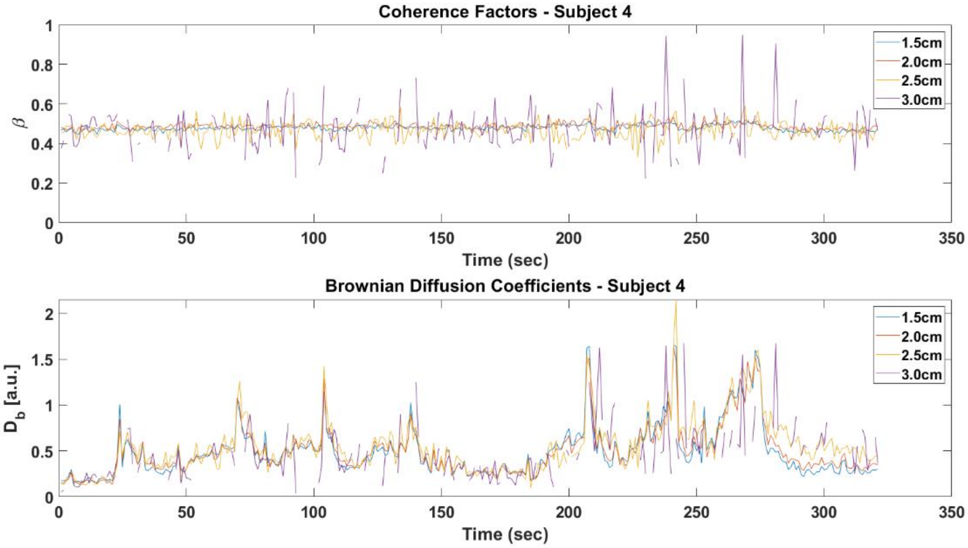

FIGURE 5-6 SUBJECT 4 - COHERENCE FACTOR MEASUREMENTS OVER TIME, TOP GRAPH, FOR EACH CHANNEL AND DIFFUSION COEFFICIENT, BOTTOM GRAPH, SHOWN FOR EACH ASSOCIATED CHANNEL

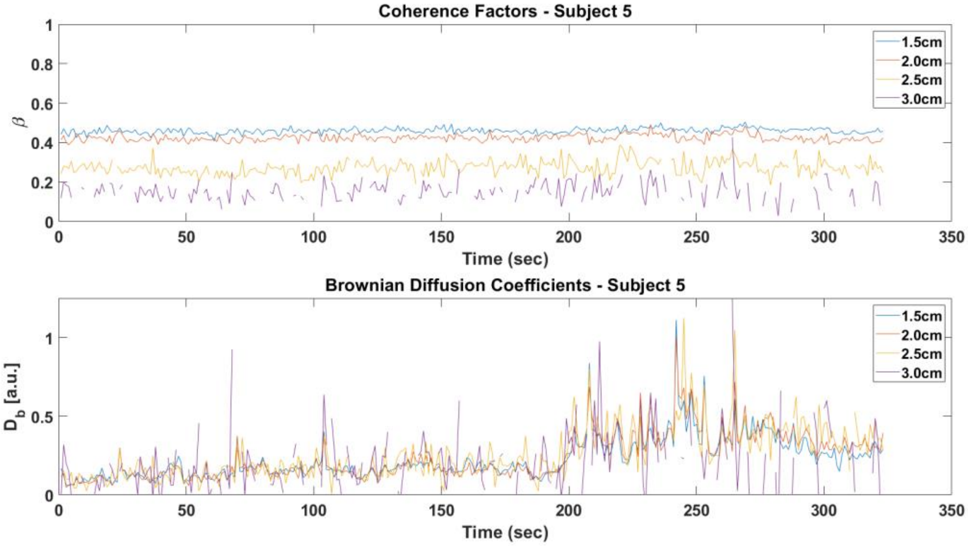

FIGURE 5-7 SUBJECT 5 - COHERENCE FACTOR MEASUREMENTS OVER TIME, TOP GRAPH, FOR EACH CHANNEL AND DIFFUSION COEFFICIENT, BOTTOM GRAPH, SHOWN FOR EACH ASSOCIATED CHANNEL

The results of the DCS blood flow measurements are shown below for subjects 1-5 in Figures 5-8 thru 5-12. For each figure the normalized diffusion coefficient is shown on the left axis with the 1.5 cm channel plotted in blue and the 2.0 cm channel plotted in red. Normalized grip strength is shown on the right axis and plotted as a dotted black line. Clean-up processing was performed on the blood flow data to better visualize the slower trends which are indicative of blood flow and remove the high frequency instrument noise. First, outlier data points were identified as more than three standard deviations above or below the mean of a 9 data point window, centered on the interrogate data point. The outliers were replaced through a linear interpolation of the same 9 data point window. The data was then smoothed with a second-order Savitzky-Golay filter with a sliding window of 15 data points. The Savitzky-Golay smoothing filter design was chosen due to the strength of removing high frequency noise while still maintaining the relative height and width of waveform peaks at high efficiency(Savitzky & Golay, 2002; Schafer, 2011) .

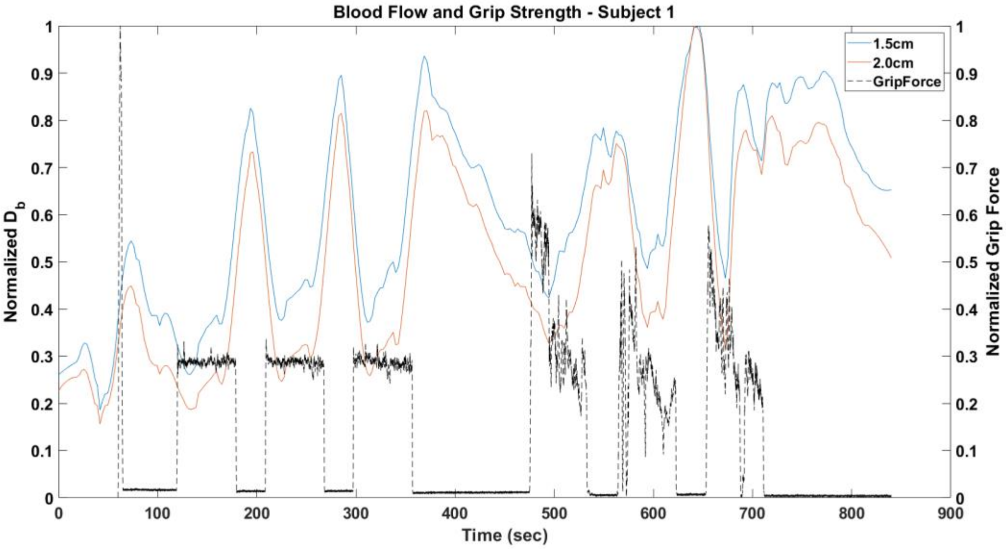

FIGURE 5-8 SUBJECT 1 - SIMULTANEOUS GRIP STRENGTH FORCE (BLACK DOTTED, RIGHT AXIS) AND DCS BLOOD FLOW MEASUREMENTS (LEFT AXIS) AT 1.5 CM (BLUE) AND 2.0 CM (RED)

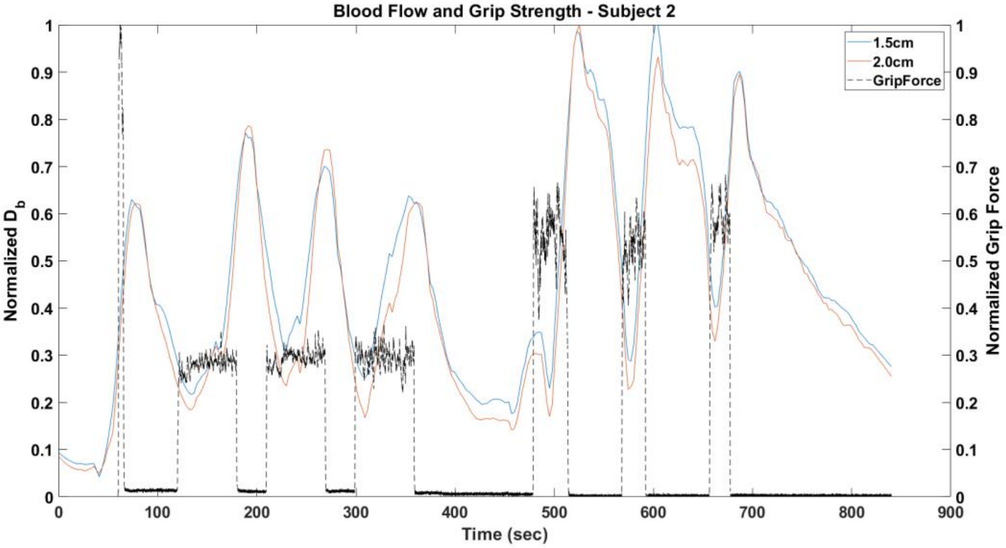

FIGURE 5-9 SUBJECT 2 - SIMULTANEOUS GRIP STRENGTH FORCE (BLACK DOTTED, RIGHT AXIS) AND DCS BLOOD FLOW MEASUREMENTS (LEFT AXIS) AT 1.5 CM (BLUE) AND 2.0 CM (RED)

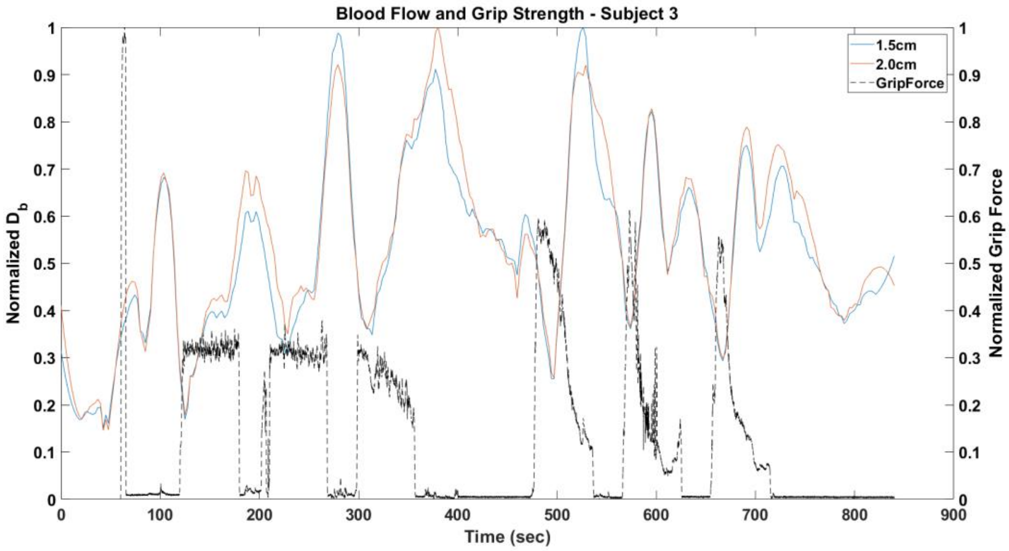

FIGURE 5-10 SUBJECT 3 - SIMULTANEOUS GRIP STRENGTH FORCE (BLACK DOTTED, RIGHT AXIS) AND DCS BLOOD FLOW MEASUREMENTS (LEFT AXIS) AT 1.5 CM (BLUE) AND 2.0 CM (RED)

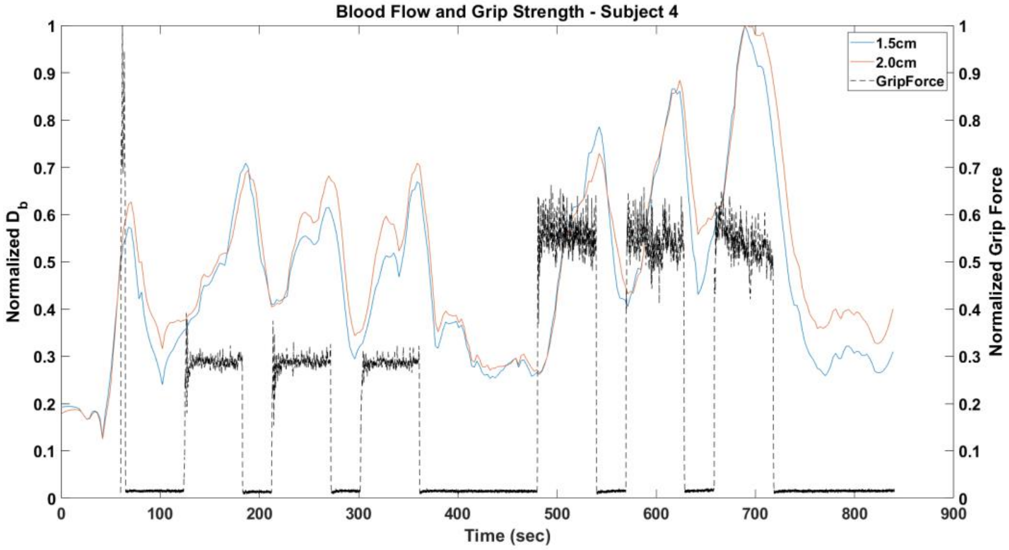

FIGURE 5-11 SUBJECT 4 - SIMULTANEOUS GRIP STRENGTH FORCE (BLACK DOTTED, RIGHT AXIS) AND DCS BLOOD FLOW MEASUREMENTS (LEFT AXIS) AT 1.5 CM (BLUE) AND 2.0 CM (RED)

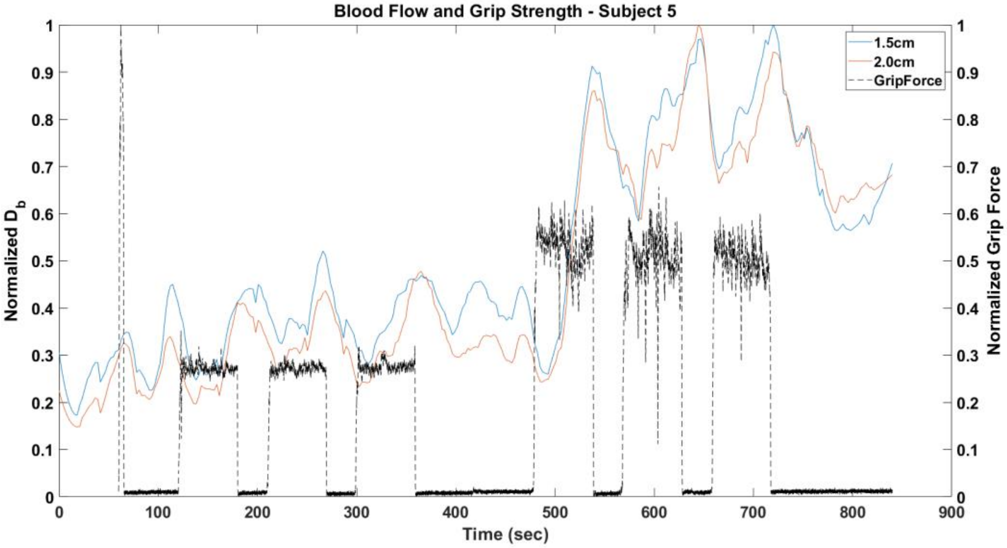

FIGURE 5-12 SUBJECT 5 - SIMULTANEOUS GRIP STRENGTH FORCE (BLACK DOTTED, RIGHT AXIS) AND DCS BLOOD FLOW MEASUREMENTS (LEFT AXIS) AT 1.5 CM (BLUE) AND 2.0 CM (RED)

Some general trends are presented by observing the data visualizations. First, all subjects were able to perform the 30% maximum grip strength phases. However, 60% of the subjects (Subjects 1,2 and 3) failed the first and, subsequently, all the 60% maximum grip strength phases with failure defined as dropping below 10% of the target force production for more than 5 consecutive seconds. The purpose of establishing this protocol was to establish benchmarks for when a healthy subject becomes fatigued. Interestingly, opposite trends were observed during the 60% maximum grip task between the subjects who failed and those who succeeded. Specifically, while Subjects 1, 2, and 3 initially attempted to perform the 60% grip strength task, their blood flow measurements decreased and only increased once they failed and partially or fully released their grip due to fatigue. This is the expected blood flow response during a 60% maximum grip strength task due to mechanical compression(OM et al., 1984) applied by the skeletal muscles, according to previous research(Barcroft & Millen, 1939; Kirby et al., 2007) . However, subjects 4 and 5 showed increased blood flow during the 60% maximum grip force tasks and decreased blood flow during the post- 60% maximum grip recovery periods. These blood flow responses are more indicative of sub- 50% maximum grip contractions, which would suggest that subjects 1 and 2 did not reach maximum grip force during the directed maximum contraction at the beginning of the protocol.

Subjects 1,2 and 3 showed decreased blood flow during the 60% grip force task. This was an expected response due to the vasodilation response that occurs after maximum voluntary contractions ~50% or greater(Kirby et al., 2007; PS et al., 2006) . Validating a true maximum grip strength during the maximum directed grip force is a challenge. Therefore, increased blood flow trends during 60% grip force like those shown by subjects 4 and 5 could possibly be used as an indicator of a submaximal evaluation during the directed max grip task. However, variability between subjects could cause significant differences in the %MVC where blood flow begins to decrease, so this observation requires further investigation. This will be an important note moving forward, as exclusion criteria may have to be employed for data collected on submaximal performing subjects to avoid contamination of the healthy population benchmarks.

# 6. Conclusion and Future Work

## 6.1 Conclusion

The focus of this dissertation work was applying previously established optical imaging techniques in specific disease states with the main goal of showing the feasibility of blood flow and oxygenation related parameters as predictive biomarkers for those diseases. The advantage of establishing quantitative biomarkers such as blood flow and oxygen saturation is that they can be used to track disease progression and the efficacy of treatments non-invasively. Autism spectrum disorder and Huntington's disease are both chronic in nature, where clinical intervention is performed through therapeutics aimed at improving quality of life and treatment of symptoms. Therefore, a quantitative measure would be valuable to clinicians for optimizing therapy response.

The first application discussed in this thesis was noninvasive cerebral blood flow monitoring in a mouse model of ASD. Hypoperfusion is a long-term research phenomenon in the autism population, where multiple other imaging modalities including ASL-MRI and laser Doppler flowmetry have been used. Our application of DCS and FD-NIRS allowed resting state cerebral blood flow (CBF) and oxygenation (StO2) measurements to be recorded over the course of a 10-minute imaging procedure. We measured CBF and optical properties in 6 BTBR and 6 C57 control mice of the same age. Significantly lower ($p = 0.0012$) CBF was observed in the autism group. Although no significant differences were observed between the groups in the optical property measurements recorded through FD-NIRS, those measurements were able to be utilized as input for the DCS fitting routine. CBF and optical property measurements were combined to estimate the cerebral metabolic rate of oxygen consumption ($CMRO_2$) through a previously derived relation. $CMRO_2$ measurements were also shown to be significantly (*p* = 0.015) lower in the ASD group. The results shown here agree with the hypoperfusion shown in previous studies of ASD through other imaging modalities(Boddaert & Zilbovicius, 2002; Dichter, 2012; Galuska et al., 2002; Jann et al., 2015; Ohnishi et al., 2000; Reynell & Harris, 2013; Sasaki et al., 2010; Yerys et al., 2018; Zilbovicius et al., 2000; Zürcher et al., 2015). Optical monitoring of ASD through combined DCS and FD-NIRS has been shown to be feasible and should be further considered for human applications.

The second application discussed in this thesis was Huntington's disease (HD). Most HD studies focus on the effects and mechanism of action within the central nervous system. Therefore, our research was a novel approach to study defects in the peripheral nervous system and skeletal muscle in HD. We applied DCS monitoring of blood flow in skeletal muscle of the R6/2 HD mouse model during electrically induced skeletal muscle contractions of the lower hind limb. The results indicate that the changes in blood flow amplitude were much smaller compared to the control group and the blood flow kinetics showed a delayed response with respect to time. This pilot study serves as a possible link between skeletal muscle dysregulation (Miranda et al., 2017) and the hyperemia mechanism in the R6/2 mouse model of Huntington's disease. However, there were some drawbacks in our initial HD measurement study. The contact-based DCS probe had to be removed during the stimulated muscle contractions, which led to the first moments of blood flow response post-contraction being missed as the probe was lowered back onto the muscle. Also, the DCS probe only provided a single point measurement which represented the average blood flow response in a banana shaped region where the detected photons diffused. Therefore, we identified a need for a non-contact blood flow measurement system.

A camera-based LSCI + SFDI measurement system was constructed and validated to image blood flow and oxygen saturation maps of mice in vivo. The optical property (absorption, scattering) and blood flow response of the system were characterized with tissue phantoms and a standard in vivo cuff ischemia procedure. The LSCI system was then validated in two control mice (C57BL/6J). The first mouse, WT1, was imaged with the skin removed to give a comparison to our previous results with contact DCS. The relative blood flow increase calculated by LSCI was similar to the relative blood flow increase found in the contact DCS measurement group with the same 10x5 tetani stimulation procedure (approximately 400% increase from baseline to post-contraction after the fifth tetani sweep). The LSCI blood flow noninvasive measurements in the mouse, WT2, showed a lower contrast at an approximate 200% increase from baseline to the post-contraction phase of the fifth tetani. A decrease in contrast from baseline to maximum blood flow was expected, after the fifth tetani, with the skin remaining intact on the animal. The added skin layer results in fewer photons reaching the muscle and for the relatively slower skin blood flow measurements to be averaged into the spatial map. However, the muted blood flow increase observed in the noninvasive mouse was still much higher than the Huntington’s disease group during the contact DCS measurements (~20% increase). Therefore, the LSCI system has shown promise in detecting increases in blood flow induced by electrically stimulated skeletal muscle contractions in mouse models.

Finally, the encouraging blood flow results shown in the mouse model of Huntington's disease led to a feasibility study for a similar experimental design in humans. Grip strength force experiments have been previously shown in human Huntington's disease subjects(Rao et al., 2011; van der Burg et al., 2009) to be an adequate indicator of disease state and progression. Similar to our research in mouse models, our aim was to add blood flow measurements as a biomarker for human HD. The first step in this process was testing the feasibility of a non-invasive blood flow measurement probe, using DCS, that can be worn during the grip strength task. We showed that DCS measurements can be obtained without interrupting the grip strength procedure and that blood flow results are qualitatively correlated with grip force production in five healthy control subjects.

## 6.2 Recommendations for Future Work

The research presented here has taken significant steps in establishing optical imaging modalities to measure tissue blood flow and oxygenation as valid biomarkers for both autism spectrum disorder and Huntington's disease. However, there remains opportunities for future work and refinements of the imaging systems implemented for this work.

First, the camera based LSCI+SFDI system has shown promise in monitoring both blood flow and tissue oxygenation non-invasively during skeletal muscle contractions. Therefore, a pilot study should be conducted to analyze blood flow and oxygenation maps and kinetics in a larger group of wild type and HD animals, similar to the study detailed in Chapter 3.2 performed with the contact DCS probe.

Before conducting this study, further improvements can be made in the LSCI + SFDI system. First, the SFDI and LSCI measurements could be combined into a single image, similar to the work being done by some other groups in the optical imaging field(Chen et al., 2021; Necochea et al., 2017) . This can be accomplished by either interleaving the laser speckle and SFDI illumination to achieve repeated sequential blood flow and oxygenation maps, or the two illumination sources could be combined into a structured light speckle image and later extracted though image processing methods.

# 7. References

Abookasis, D., Lerman, D., Roth, H., Tfilin, M., & Turgeman, G. (2018). Optically derived metabolic and hemodynamic parameters predict hippocampal neurogenesis in the BTBR mouse model of autism. *Journal of Biophotonics*, *11*(3). https://doi.org/10.1002/jbio.201600322

Allen, G., & Courchesne, E. (2003). Differential effects of developmental cerebellar abnormality on cognitive and motor functions in the cerebellum: an fMRI study of autism. *The American Journal of Psychiatry*, *160*(2), 262–273. https://doi.org/10.1176/appi.ajp.160.2.262

Applegate, M. B., Karrobi, K., Jr., J. P. A., Austin, W., Tabassum, S. M., Aguénounon, E., Tilbury, K., Saager, R. B., Gioux, S., & Roblyer, D. (2020). OpenSFDI: an open-source guide for constructing a spatial frequency domain imaging system. *Journal of Biomedical Optics*, *25*(1), 1. https://doi.org/10.1117/1.JBO.25.1.016002

Armstrong, M. J., & Miyasaki, J. M. (2012). *Evidence-based guideline: Pharmacologic treatment of chorea in Huntington disease*. www.neurology.org

Ayala-Peña, S. (2013). *Role of Oxidative DNA Damage in Mitochondrial Dysfunction and Huntington's Disease Pathogenesis*. https://doi.org/10.1016/j.freeradbiomed.2013.04.017

Barcroft, H., & Millen, J. L. E. (1939). The blood flow through muscle during sustained contraction. *The Journal of Physiology*, *97*(1), 17. https://doi.org/10.1113/JPHYSIOL.1939.SP003789

B, G., S, P., S, R., V, Q., M, F., C, M., & P, C. (2003). Muscle oxygenation and pulmonary gas exchange kinetics during cycling exercise on-transitions in humans. *Journal of Applied Physiology (Bethesda, Md. : 1985)*, *95*(1), 149–158. https://doi.org/10.1152/JAPPLPHYSIOL.00695.2002

Bilney, B., Morris, M. E., Churchyard, A., Chiu, E., & Georgiou-Karistianis, N. (2005). Evidence for a disorder of locomotor timing in Huntington's disease. *Movement Disorders: Official Journal of the Movement Disorder Society*, *20*(1), 51–57. https://doi.org/10.1002/mds.20294

BJ, L., LF, F., DC, P., D, T., & TJ, B. (2008). Muscle microvascular hemoglobin concentration and oxygenation within the contraction-relaxation cycle. *Respiratory Physiology & Neurobiology*, *160*(2), 131–138. https://doi.org/10.1016/J.RESP.2007.09.005

Boas, D. A., Campbell, L. E., & Yodh, A. G. (1995). Scattering and imaging with diffusing temporal field correlations. *Physical Review Letters*, *75*(9), 1855–1858. https://doi.org/10.1103/PhysRevLett.75.1855

Boas, D. A., & Dunn, A. K. (2010). Laser speckle contrast imaging in biomedical optics. *Journal of Biomedical Optics*, *15*(1), 11109. https://doi.org/10.1117/1.3285504

Boddaert, N., & Zilbovicius, M. (2002). Functional neuroimaging and childhood autism. *Pediatric Radiology*, *32*(1), 1–7. https://doi.org/10.1007/s00247-001-0570-x

Brandt, J. (2018). Behavioral Changes in Huntington Disease. In *Cognitive and Behavioral Neurology* (Vol. 31, Issue 1, pp. 26–27). Lippincott Williams and Wilkins. https://doi.org/10.1097/WNN.0000000000000147

Buckley, E. M., Parthasarathy, A. B., Grant, P. E., Yodh, A. G., & Franceschini, M. A. (2014). Diffuse correlation spectroscopy for measurement of cerebral blood flow: future prospects. *Neurophotonics*, *1*(1). https://doi.org/10.1117/1.NPh.1.1.011009

Carroll, J. B., Bates, G. P., Steffan, J., Saft, C., & Tabrizi, S. J. (2015). Treating the whole body in Huntington's disease. *The Lancet. Neurology*, *14*(11), 1135–1142. https://doi.org/10.1016/S1474-4422(15)00177-5

Chadman, K. K., Guariglia, S. R., & Yoo, J. H. (2012). New directions in the treatment of autism spectrum disorders from animal model research. *Expert Opinion on Drug Discovery*, *7*(5), 407–416. https://doi.org/10.1517/17460441.2012.678828

Chaturvedi, R. K., Adhihetty, P., Shukla, S., Hennessy, T., Calingasan, N., Yang, L., Starkov, A., Kiaei, M., Cannella, M., Sassone, J., Ciammola, A., Squitieri, F., & Flint Beal, M. (n.d.). *Impaired PGC-1a function in muscle in Huntington's disease*. https://doi.org/10.1093/hmg/ddp243

Cheng, H., Yu, J., Xu, L., & Li, J. (2019). Power spectrum of spontaneous cerebral homodynamic oscillation shows a distinct pattern in autism spectrum disorder. *Biomedical Optics Express*, *10*(3), 1383. https://doi.org/10.1364/boe.10.001383

Chen, M. T., Papadakis, M., & Durr, N. J. (2021). Speckle illumination SFDI for projector-free optical property mapping. *Optics Letters, Vol. 46, Issue 3, Pp. 673-676*, *46*(3), 673–676. https://doi.org/10.1364/OL.411187

Cheung, C., Culver, J. P., Takahashi, K., Greenberg, J. H., & Yodh, A. G. (2001). In vivo cerebrovascular measurement combining diffuse near-infrared absorption and correlation spectroscopies. *Physics in Medicine and Biology*, *46*(8), 2053–2065. https://doi.org/10.1088/0031-9155/46/8/302

Chong, S. P., Merkle, C. W., Leahy, C., & Srinivasan, V. J. (2015). Cerebral metabolic rate of oxygen (CMRO_2) assessed by combined Doppler and spectroscopic OCT. *Biomedical Optics Express*, *6*(10), 3941. https://doi.org/10.1364/boe.6.003941

CM, K., C, S., FN, G., Z, G., M, D., J, S., AB, Y., GB, L., KV, T., B, S., & KS, L. (2007). Myopathy as a first symptom of Huntington's disease in a Marathon runner. *Movement Disorders : Official Journal of the Movement Disorder Society*, *22*(11), 1637–1640. https://doi.org/10.1002/MDS.21550

Constantinides, C., Mean, R., & Janssen, B. J. (2011). Effects of Isoflurane Anesthesia on the Cardiovascular Function of the C57BL/6 Mouse. *ILAR Journal / National Research Council, Institute of Laboratory Animal Resources*, *52*, e21–e31. https://www.ncbi.nlm.nih.gov/pmc/articles/PMC3508701/

Cornew, L., Roberts, T. P. L., Blaskey, L., & Edgar, J. C. (2012). Resting-state oscillatory activity in autism spectrum disorders. *Journal of Autism and Developmental Disorders*, *42*(9), 1884–1894. https://doi.org/10.1007/s10803-011-1431-6

Costa, M. do C., Magalhães, P., Guimarães, L., Maciel, P., Sequeiros, J., & Sousa, A. (2006). The CAG repeat at the Huntington disease gene in the Portuguese population: insights into its dynamics and to the origin of the mutation. *Journal of Human Genetics*, *51*(3), 189–195. https://doi.org/10.1007/s10038-005-0343-8

Cruickshank, T., Reyes, A., Peñailillo, L., Thompson, J., & Ziman, M. (2014). Factors that contribute to balance and mobility impairments in individuals with Huntington's disease. *Basal Ganglia*, *4*(2), 67–70. https://doi.org/10.1016/j.baga.2014.04.002

Cuccia, D. J., Bevilacqua, F., Durkin, A. J., Ayers, F. R., & Tromberg, B. J. (2009). Quantitation and mapping of tissue optical properties using modulated imaging. *Journal of Biomedical Optics*, *14*(2), 024012. https://doi.org/10.1117/1.3088140

Cuccia, D. J., Bevilacqua, F., Durkin, A. J., & Tromberg, B. J. (2005). Modulated imaging: quantitative analysis and tomography of turbid media in the spatial-frequency domain Experiments performed on turbid phantoms demonstrate that spatially modulated illumination facilitates quantitative wide-field optical property mapping. In *OPTICS LETTERS* (Vol. 170, Issue 11).

Culver, J. P., Durduran, T., Furuya, D., Cheung, C., Greenberg, J. H., & Yodh, A. G. (2016). Diffuse Optical Tomography of Cerebral Blood Flow, Oxygenation, and Metabolism in Rat during Focal Ischemia: *Http://Dx.Doi.Org/10.1097/01.WCB.0000076703.71231.BB*, *23*(8), 911–924. https://doi.org/10.1097/01.WCB.0000076703.71231.BB

Cusin, C., Franco, F. B., Fernandez-Robles, C., DuBois, C. M., & Welch, C. A. (2013). Rapid improvement of depression and psychotic symptoms in Huntington's disease: a retrospective chart review of seven patients treated with electroconvulsive therapy. *General Hospital Psychiatry*, *35*(6), 678.e3-5. https://doi.org/10.1016/j.genhosppsych.2013.01.015

Dichter, G. S. (2012). Functional magnetic resonance imaging of autism spectrum disorders. *Dialogues in Clinical Neuroscience*, *14*(3), 319–351. https://www.ncbi.nlm.nih.gov/pmc/articles/PMC3513685/

Duncan, D. D., Wells-Gray, E. M., & Kirkpatrick, S. J. (2008). Detrimental effects of speckle-pixel size matching in laser speckle contrast imaging. *Optics Letters, Vol. 33, Issue 24, Pp. 2886-2888*, *33*(24), 2886–2888. https://doi.org/10.1364/OL.33.002886

Durduran, T., & Yodh, A. G. (2014). Diffuse correlation spectroscopy for non-invasive, micro-vascular cerebral blood flow measurement. *NeuroImage*, *85 Pt 1*, 51–63. https://doi.org/10.1016/j.neuroimage.2013.06.017

Faraci, F. M., & Heistad, D. D. (1990). Regulation of large cerebral arteries and cerebral microvascular pressure. *Circulation Research*, *66*(1), 8–17. https://doi.org/10.1161/01.res.66.1.8

Fercher, A. F., & Briers, J. D. (1981). Flow visualization by means of single-exposure speckle photography. *Optics Communications*, *37*(5), 326–330. https://doi.org/10.1016/0030-4018(81)90428-4

Ferguson, S. K., Harral, J. W., Pak, D. I., Redinius, K. M., Stenmark, K. R., Schaer, D. J., Buehler, P. W., & Irwin, D. C. (2018). Impact of cell-free hemoglobin on contracting skeletal muscle microvascular oxygen pressure dynamics. *Nitric Oxide*, *76*, 29–36. https://doi.org/10.1016/J.NIOX.2018.03.005

Ferrari, M., Binzoni, T., & Quaresima, V. (1997). Oxidative metabolism in muscle. *Philosophical Transactions of the Royal Society B: Biological Sciences*, *352*(1354), 677. https://doi.org/10.1098/RSTB.1997.0049

Folstein, S. E., Chase, G. A., Wahl, W. E., McDonnell, A. M., & Folstein, M. F. (1987). Huntington disease in Maryland: clinical aspects of racial variation. *American*

*Journal of Human Genetics*, *41*(2), 168. https://www.ncbi.nlm.nih.gov/pmc/articles/PMC1684204/

Galuska, L., Szakáll, S., Emri, M., Oláh, R., Varga, J., Garai, I., Kollár, J., Pataki, I., & Trón, L. (2002). [PET and SPECT scans in autistic children]. *Orvosi Hetilap*, *143*(21 Suppl 3), 1302–1304. http://www.ncbi.nlm.nih.gov/pubmed/12077922

Harper, P. S. (1992). The epidemiology of Huntington's disease. *Human Genetics*, *89*(4), 365–376. https://doi.org/10.1007/bf00194305

Ivanov, K. P., Kalinina, M. K., & Levkovich, Y. I. (1981). Blood flow velocity in capillaries of brain and muscles and its physiological significance. *Microvascular Research*, *22*(2), 143–155. https://doi.org/10.1016/0026-2862(81)90084-4

Jann, K., Hernandez, L. M., Beck-Pancer, D., McCarron, R., Smith, R. X., Dapretto, M., & Wang, D. J. J. (2015). Altered resting perfusion and functional connectivity of default mode network in youth with autism spectrum disorder. *Brain and Behavior*, *5*(9), e00358. https://doi.org/10.1002/brb3.358

JD, B. (2001). Laser Doppler, speckle and related techniques for blood perfusion mapping and imaging. *Physiological Measurement*, *22*(4). https://doi.org/10.1088/0967-3334/22/4/201

Johnson, C. P., & Myers, S. M. (2007). Identification and evaluation of children with autism spectrum disorders. *Pediatrics*, *120*(5), 1183–1215. https://doi.org/10.1542/peds.2007-2361

Kern, J. K., Geier, D. A., Sykes, L. K., & Geier, M. R. (2016). Relevance of Neuroinflammation and Encephalitis in Autism. *Frontiers in Cellular Neuroscience*, *9*. https://doi.org/10.3389/fncel.2015.00519

Khedraki, A., Reed, E. J., Romer, S. H., Wang, Q., Romine, W., Rich, M. M., Talmadge, R. J., & Voss, A. A. (2017). Depressed Synaptic Transmission and Reduced Vesicle Release Sites in Huntington's Disease Neuromuscular Junctions. *The Journal of Neuroscience: The Official Journal of the Society for Neuroscience*, *37*(34), 8077–8091. https://doi.org/10.1523/JNEUROSCI.0313-17.2017

Kirby, B. S., Carlson, R. E., Markwald, R. R., Voyles, W. F., & Dinenno, F. A. (2007). Mechanical influences on skeletal muscle vascular tone in humans: insight into contraction-induced rapid vasodilatation. *The Journal of Physiology*, *583*(Pt 3), 861. https://doi.org/10.1113/JPHYSIOL.2007.131250

Kokmen, E., Ozekmekçi, F. S., Beard, C. M., O'Brien, P. C., & Kurland, L. T. (1994). Incidence and prevalence of Huntington's disease in Olmsted County, Minnesota (1950 through 1989). *Archives of Neurology*, *51*(7), 696–698. https://doi.org/10.1001/archneur.1994.00540190076018

Koller, W. C., & Trimble, J. (1985). The gait abnormality of Huntington's disease. *Neurology*, *35*(10), 1450–1454. https://doi.org/10.1212/wnl.35.10.1450

Labbadia, J., & Morimoto, R. I. (2013). Huntington's disease: Underlying molecular mechanisms and emerging concepts. In *Trends in Biochemical Sciences* (Vol. 38, Issue 8). https://doi.org/10.1016/j.tibs.2013.05.003

LF, F., DM, H., & TJ, B. (2007). Effects of assuming constant optical scattering on measurements of muscle oxygenation by near-infrared spectroscopy during exercise. *Journal of Applied Physiology (Bethesda, Md. : 1985)*, *102*(1), 358–367. https://doi.org/10.1152/JAPPLPHYSIOL.00920.2005

Li, J., Dietsche, G., Iftime, D., Skipetrov, S. E., Maret, G., Elbert, T., Rockstroh, B., & Gisler, T. (2005). Noninvasive detection of functional brain activity with near-infrared diffusing-wave spectroscopy. *Journal of Biomedical Optics*, *10*(4), 044002. https://doi.org/10.1117/1.2007987

Li, J., Qiu, L., Xu, L., Pedapati, E. v, Erickson, C. A., & Sunar, U. (2016). Characterization of autism spectrum disorder with spontaneous hemodynamic activity. *Biomedical Optics Express*, *7*(10), 3871–3881. https://doi.org/10.1364/BOE.7.003871

Li, Y., Jia, H., & Yu, D. (2018). Novel analysis of fNIRS acquired dynamic hemoglobin concentrations: application in young children with autism spectrum disorder. *Biomedical Optics Express*, *9*(8), 3694. https://doi.org/10.1364/boe.9.003694

Li, Y., & Yu, D. (2016). Weak network efficiency in young children with Autism Spectrum Disorder: Evidence from a functional near-infrared spectroscopy study. *Brain and Cognition*, *108*, 47–55. https://doi.org/10.1016/j.bandc.2016.07.006

Lord, C., Risi, S., Lambrecht, L., Cook, E. H., Leventhal, B. L., DiLavore, P. C., Pickles, A., & Rutter, M. (2000). The Autism Diagnostic Observation Schedule-Generic: A standard measure of social and communication deficits associated with the spectrum of autism. *Journal of Autism and Developmental Disorders*, *30*(3), 205–223. https://doi.org/10.1023/A:1005592401947

Meechan, D. W., Rutz, H. L. H., Fralish, M. S., Maynard, T. M., Rothblat, L. A., & LaMantia, A.-S. (2015). Cognitive Ability is Associated with Altered Medial Frontal Cortical Circuits in the LgDel Mouse Model of 22q11.2DS. *Cerebral Cortex (New York, NY)*, *25*(5), 1143–1151. https://doi.org/10.1093/cercor/bht308

Mesquita, R. C., Durduran, T., Yu, G., Buckley, E. M., Kim, M. N., Zhou, C., Choe, R., Sunar, U., & Yodh, A. G. (2011). Direct measurement of tissue blood flow and metabolism with diffuse optics. *Philosophical Transactions. Series A, Mathematical, Physical, and Engineering Sciences*, *369*(1955), 4390–4406. https://doi.org/10.1098/rsta.2011.0232

M, F., L, M., & V, Q. (2004). Principles, techniques, and limitations of near infrared spectroscopy. *Canadian Journal of Applied Physiology = Revue Canadienne de Physiologie Appliquee*, *29*(4), 463–487. https://doi.org/10.1139/H04-031

Miranda, D. R., Wong, M., Romer, S. H., McKee, C., Garza-Vasquez, G., Medina, A. C., Bahn, V., Steele, A. D., Talmadge, R. J., & Voss, A. A. (2017). Progressive Cl-channel defects reveal disrupted skeletal muscle maturation in R6/2 Huntington's mice. *The Journal of General Physiology*, *149*(1), 55–74. https://doi.org/10.1085/jgp.201611603

Morgan, J. T., Chana, G., Pardo, C. A., Achim, C., Semendeferi, K., Buckwalter, J., Courchesne, E., & Everall, I. P. (2010). Microglial activation and increased microglial density observed in the dorsolateral prefrontal cortex in autism. *Biological Psychiatry*, *68*(4), 368–376. https://doi.org/10.1016/j.biopsych.2010.05.024

Mueller, S. M., Gehrig, S. M., Petersen, J. A., Frese, S., Mihaylova, V., Ligon-Auer, M., Khmara, N., Nuoffer, J.-M., Schaller, A., Lundby, C., Toigo, M., & Jung, H. H. (2017). Effects of endurance training on skeletal muscle mitochondrial function in Huntington disease patients. *Orphanet Journal of Rare Diseases*, *12*. https://doi.org/10.1186/s13023-017-0740-z

Necochea, J., Prieto, J., Hoffman, Z., & DiMarzio, C. (2017). Laser speckle contrast imaging augmented with structured light. *Three-Dimensional and Multidimensional Microscopy: Image Acquisition and Processing XXIV*, *10070*, 100701F. https://doi.org/10.1117/12.2275272

O'Doherty, J., McNamara, P., Clancy, N. T., Enfield, J. G., & Leahy, M. J. (2009). Comparison of instruments for investigation of microcirculatory blood flow and red blood cell concentration. *Journal of Biomedical Optics*, *14*(3), 034025. https://doi.org/10.1117/1.3149863

Ohnishi, T., Matsuda, H., Hashimoto, T., Kunihiro, T., Nishikawa, M., Uema, T., & Sasaki, M. (2000). Abnormal regional cerebral blood flow in childhood autism. *Brain: A Journal of Neurology*, *123 ( Pt 9*, 1838–1844. https://doi.org/10.1093/brain/123.9.1838

OM, S., AR, H., KR, K., P, B., O, J., & L, H. (1984). Intramuscular fluid pressure during isometric contraction of human skeletal muscle. *Journal of Applied Physiology:*

*Respiratory, Environmental and Exercise Physiology*, *56*(2), 287–295. https://doi.org/10.1152/JAPPL.1984.56.2.287

Philip, R. C. M., Dauvermann, M. R., Whalley, H. C., Baynham, K., Lawrie, S. M., & Stanfield, A. C. (2012). A systematic review and meta-analysis of the fMRI investigation of autism spectrum disorders. *Neuroscience and Biobehavioral Reviews*, *36*(2), 901–942. https://doi.org/10.1016/j.neubiorev.2011.10.008

Pollonini, L. (2018). Optical Properties and Molar Hemoglobin Concentration of Skeletal Muscles Measured in Vivo with Wearable Near Infrared Spectroscopy. *IEEE Sensors Journal*, *18*(6), 2326–2334. https://doi.org/10.1109/JSEN.2018.2794969

Poon, C., Rinehart, B., Li, J., & Sunar, U. (2020). Cerebral blood flow-based resting state functional connectivity of the human brain using optical diffuse correlation spectroscopy. *Journal of Visualized Experiments*, *2020*(159), 1–7. https://doi.org/10.3791/60765

PS, C., HA, K., JJ, H., JB, B., & JL, J. (2006). Mechanical compression elicits vasodilatation in rat skeletal muscle feed arteries. *The Journal of Physiology*, *572*(Pt 2), 561–567. https://doi.org/10.1113/JPHYSIOL.2005.099507

P, T., MT, H., & W, D. (2003). Two-photon imaging to a depth of 1000 microm in living brains by use of a Ti:Al2O3 regenerative amplifier. *Optics Letters*, *28*(12), 1022. https://doi.org/10.1364/OL.28.001022

Quarrell, O. W., Tyler, A., Jones, M. P., Nordin, M., & Harper, P. S. (1988). Population studies of Huntington's disease in Wales. *Clinical Genetics*, *33*(3), 189–195. https://doi.org/10.1111/j.1399-0004.1988.tb03436.x

RA, D. B., M, F., A, N., G, C., A, M., & A, G. (1994). Noninvasive measurement of forearm blood flow and oxygen consumption by near-infrared spectroscopy. *Journal of Applied Physiology (Bethesda, Md. : 1985)*, *76*(3), 1388–1393. https://doi.org/10.1152/JAPPL.1994.76.3.1388

Rao, A. K., Gordon, A. M., & Marder, K. S. (2011). Coordination of fingertip forces during precision grip in premanifest Huntington's disease. *Movement Disorders*, *26*(5), 862–869. https://doi.org/10.1002/mds.23606

Reed, T. E., & Chandler, J. H. (1958). Huntington's chorea in Michigan. I. Demography and genetics. *American Journal of Human Genetics*, *10*(2), 201–225. http://www.ncbi.nlm.nih.gov/pubmed/13533397

Reilmann, R. (n.d.). *Pharmacological Treatment of Chorea in Huntington's Disease-Good Clinical Practice versus Evidence-based Guideline*. https://doi.org/10.1002/mds.25500

Reyes, A., Cruickshank, T., Ziman, M., & Nosaka, K. (2014). Pulmonary function in patients with Huntington's Disease. *BMC Pulmonary Medicine 2014 14:1*, *14*(1), 1–8. https://doi.org/10.1186/1471-2466-14-89

Reynell, C., & Harris, J. J. (2013). The BOLD signal and neurovascular coupling in autism. *Accident Analysis and Prevention*, *6*, 72–79. https://doi.org/10.1016/j.dcn.2013.07.003

Rinehart, B., Poon, C. S., & Sunar, U. (2021). Quantification of perfusion and metabolism in an autism mouse model assessed by diffuse correlation spectroscopy and near-infrared spectroscopy. *Journal of Biophotonics*, *14*(11), e202000454. https://doi.org/10.1002/JBIO.202000454

Sasaki, M., Nakagawa, E., Sugai, K., Shimizu, Y., Hattori, A., Nonoda, Y., & Sato, N. (2010). Brain perfusion SPECT and EEG findings in children with autism spectrum disorders and medically intractable epilepsy. *Brain & Development*, *32*(9), 776–782. https://doi.org/10.1016/j.braindev.2010.06.003

Savitzky, Abraham., & Golay, M. J. E. (2002). Smoothing and Differentiation of Data by Simplified Least Squares Procedures. *Analytical Chemistry*, *36*(8), 1627–1639. https://doi.org/10.1021/AC60214A047

Schafer, R. W. (2011). What is a savitzky-golay filter? *IEEE Signal Processing Magazine*, *28*(4), 111–117. https://doi.org/10.1109/MSP.2011.941097

Shokeir, M. H. K. (1975). Investigation on Huntington's disease in the Canadian Prairies. *Clinical Genetics*, *7*(4), 349–353. https://doi.org/10.1111/j.1399-0004.1975.tb00341.x

Simonoff, E., Pickles, A., Charman, T., Chandler, S., Loucas, T., & Baird, G. (2008). Psychiatric disorders in children with autism spectrum disorders: Prevalence, comorbidity, and associated factors in a population-derived sample. *Journal of the American Academy of Child and Adolescent Psychiatry*, *47*(8), 921–929. https://doi.org/10.1097/CHI.0b013e318179964f

Simpson, S. A., & Johnston, A. W. (1989). The prevalence and patterns of care of Huntington's chorea in Grampian. *The British Journal of Psychiatry: The Journal of Mental Science*, *155*, 799–804. https://doi.org/10.1192/bjp.155.6.799

Stephenson, D. T., O'Neill, S. M., Narayan, S., Tiwari, A., Arnold, E., Samaroo, H. D., Du, F., Ring, R. H., Campbell, B., Pletcher, M., Vaidya, V. A., & Morton, D. (2011). Histopathologic characterization of the BTBR mouse model of autistic-like behavior reveals selective changes in neurodevelopmental proteins and adult hippocampal neurogenesis. *Molecular Autism*, *2*(1), 7. https://doi.org/10.1186/2040-2392-2-7

S, W., M, C., DT, D., JS, W., & EO, R. (1988). Characterization of the near infrared absorption spectra of cytochrome aa3 and haemoglobin for the non-invasive monitoring of cerebral oxygenation. *Biochimica et Biophysica Acta*, *933*(1), 184–192. https://doi.org/10.1016/0005-2728(88)90069-2

Thaut, M. H., Miltner, R., Lange, H. W., Hurt, C. P., & Hoemberg, V. (1999). Velocity modulation and rhythmic synchronization of gait in Huntington’s disease. *Movement Disorders: Official Journal of the Movement Disorder Society*, *14*(5), 808–819. https://doi.org/10.1002/1531-8257(199909)14:5<808::aid-mds1014>3.0.co;2-j

Theoharides, T. C., Tsilioni, I., Patel, A. B., & Doyle, R. (2016). Atopic diseases and inflammation of the brain in the pathogenesis of autism spectrum disorders. In *Translational Psychiatry* (Vol. 6, Issue 6, p. e844). Nature Publishing Group. https://doi.org/10.1038/tp.2016.77

van der Burg, J. M. M., Björkqvist, M., & Brundin, P. (2009). Beyond the brain: widespread pathology in Huntington’s disease. *The Lancet. Neurology*, *8*(8), 765–774. https://doi.org/10.1016/S1474-4422(09)70178-4

Vargas, D. L., Nascimbene, C., Krishnan, C., Zimmerman, A. W., & Pardo, C. A. (2005). Neuroglial activation and neuroinflammation in the brain of patients with autism. *Annals of Neurology*, *57*(1), 67–81. https://doi.org/10.1002/ana.20315

Wahlsten, D., Metten, P., & Crabbe, J. C. (2003). Survey of 21 inbred mouse strains in two laboratories reveals that BTBR T/+ tf/tf has severely reduced hippocampal commissure and absent corpus callosum. *Brain Research*, *971*(1), 47–54. https://doi.org/10.1016/s0006-8993(03)02354-0

Waters, C. W., Varuzhanyan, G., Talmadge, R. J., & Voss, A. A. (2013). Huntington disease skeletal muscle is hyperexcitable owing to chloride and potassium channel dysfunction. *Proceedings of the National Academy of Sciences of the United States of America*, *110*(22). https://doi.org/10.1073/pnas.1220068110

Wheelock, V. L., Tempkin, T., Marder, K., Nance, M., Myers, R. H., Zhao, H., Kayson, E., Orme, C., Shoulson, I., & Group, H. S. (2003). Predictors of nursing home placement in Huntington disease. *Neurology*, *60*(6), 998–1001. https://doi.org/10.1212/01.wnl.0000052992.58107.67

Wyant, K. J., Ridder, A. J., & Dayalu, P. (2017). Huntington's Disease—Update on Treatments. In *Current Neurology and Neuroscience Reports* (Vol. 17, Issue 4). Current Medicine Group LLC 1. https://doi.org/10.1007/s11910-017-0739-9

Yerys, B. E., Herrington, J. D., Bartley, G. K., Liu, H. S., Detre, J. A., & Schultz, R. T. (2018). Arterial spin labeling provides a reliable neurobiological marker of autism spectrum disorder. *Journal of Neurodevelopmental Disorders*, *10*(1). https://doi.org/10.1186/s11689-018-9250-0

Y, K., N, O., M, K., A, T., & K, H. (2015). Examination of tissue oxygen saturation (StO2) changes associated with vascular pedicle occlusion in a rat Island flap model using near-Infrared spectroscopy. *Microsurgery*, *35*(5), 393–398. https://doi.org/10.1002/MICR.22385

Zang, Y. F., Yong, H., Chao-Zhe, Z., Qing-Jiu, C., Man-Qiu, S., Meng, L., Li-Xia, T., Tian-Zi, J., & Yu-Feng, W. (2007). Altered baseline brain activity in children with ADHD revealed by resting-state functional MRI. *Brain and Development*, *29*(2), 83–91. https://doi.org/10.1016/j.braindev.2006.07.002

Zhu, H., Fan, Y., Guo, H., Huang, D., & He, S. (2014). Reduced interhemispheric functional connectivity of children with autism spectrum disorder: evidence from functional near infrared spectroscopy studies. *Biomedical Optics Express*, *5*(4), 1262–1274. https://doi.org/10.1364/BOE.5.001262

Zhu, J.-N., Sipione, S., Gray, M., Gomez-Pastor, R., Intihar, T. A., & Martinez, E. A. (2019). Mitochondrial Dysfunction in Huntington's Disease; Interplay Between HSF1, p53 and PGC-1 Transcription Factors. *HYPOTHESIS AND THEORY Published*. https://doi.org/10.3389/fncel.2019.00103

Zielonka, D., Piotrowska, I., Marcinkowski, J. T., & Mielcarek, M. (2014). Skeletal muscle pathology in Huntington's disease. *Frontiers in Physiology*, *5*. https://doi.org/10.3389/fphys.2014.00380

Zilbovicius, M., Boddaert, N., Belin, P., Poline, J. B., Remy, P., Mangin, J. F., Thivard, L., Barthélémy, C., & Samson, Y. (2000). Temporal lobe dysfunction in childhood autism: a PET study. Positron emission tomography. *The American Journal of Psychiatry*, *157*(12), 1988–1993. https://doi.org/10.1176/appi.ajp.157.12.1988

Zilbovicius, M., Garreau, B., Samson, Y., Remy, P., Barthélémy, C., Syrota, A., & Lelord, G. (1995). Delayed maturation of the frontal cortex in childhood autism. *The American Journal of Psychiatry*, *152*(2), 248–252. https://doi.org/10.1176/ajp.152.2.248

Zürcher, N. R., Bhanot, A., McDougle, C. J., & Hooker, J. M. (2015). A systematic review of molecular imaging (PET and SPECT) in autism spectrum disorder: Current state and future research opportunities. In *Neuroscience and Biobehavioral Reviews* (Vol. 52, pp. 56–73). Elsevier Ltd. https://doi.org/10.1016/j.neubiorev.2015.02.002